# OXYGEN ISOTOPE COMPOSITION AND TOURMALINE MINERAL CHEMISTRY OF THE COSO AND DARAJAT GEOTHERMAL SYSTEMS

by

Thomas Mitchell Etzel

A thesis submitted to the faculty of
The University of Utah
in partial fulfillment of the requirements for the degree of

Master of Science

in

Geology

Department of Geology and Geophysics

The University of Utah

December 2016

Copyright © Thomas Mitchell Etzel 2016

All Rights Reserved

**The University of Utah Graduate School**

# STATEMENT OF THESIS APPROVAL

The thesis of **Thomas Mitchell Etzel**

has been approved by the following supervisory committee members:

| | | |
|---|---|---|
| **John R. Bowman** | , Chair | **12/17/2015** Date Approved |
| **Joseph N. Moore** | , Member | **12/17/2015** Date Approved |
| **Erich U. Petersen** | , Member | **12/17/2015** Date Approved |

and by **John M. Bartley**, Chair/Dean of

the Department/College/School of **Geology and Geophysics**

and by David B. Kieda, Dean of The Graduate School.

ABSTRACT

At the Coso geothermal system, near China Lake, California, clay mineralogy and the extent of $^{18}O/^{16}O$ depletion in whole rock samples and mineral separates have been determined for a suite of samples from wells 33A-7, 68-6 and 73-19 along the high temperature Western Flank. In general clay mineralogy changes from smectite to interlayered illite-smectite (I/S) to illite with increasing depth. However, their distributions are not closely correlated with the distributions expected from the present-day temperature profile. More widespread $^{18}O/^{16}O$ depletion northward along the Western Flank generally correlates with greater clay mineral abundances, thinner smectite zone, and absence of mixed I/S, suggesting clay mineral distribution in the Coso field is a function of both the extent of fluid-rock interaction and temperature. The $\delta^{18}O$ measurements identify a limited number of localized intervals of extensive $^{18}O/^{16}O$ depletion that signify interaction and oxygen isotope exchange with significant quantities of geothermal fluid. These local zones of maximum $^{18}O/^{16}O$ depletion in each well correspond closely with the depths of current production zone (restricted intervals of known high permeability). This association of discrete zones of high permeability with extensive but localized $^{18}O/^{16}O$ depletion indicates that the extent of $^{18}O/^{16}O$ depletion serves as a guide to the extent of fluid-rock interaction and permeability in the reservoir rock.

The chemical compositions of two separate tourmaline populations (Stage 1 and Stage 3) from well DRJ-S1 at Darajat, Indonesia, have been determined. These data, in combination with petrologic observations, are used to improve our understanding of the evolution of the Darajat vapor-dominated geothermal system. Stage 1 tourmalines (replacing feldspar) have distinctly higher Fe/(Fe + Mg) and Na/(Na + Ca) ratios than Stage 3 tourmalines (formed in anhydrite veins). Mineral paragenesis and the presence of Fe-rich tourmalines suggest that Stage 1 formed in a higher temperature, fluid-dominated environment following the emplacement of subvolcanic intrusives. Ca-abundant Stage 3 tourmalines formed after descending steam condensates causing advanced argillic alteration approached a neutral pH. Furthermore, continued anhydrite and calcite deposition (due to the heating of descending steam condensates) at shallow levels reduced porosity and permeability, impeding reservoir recharge, resulting in the current vapor-dominated system.

TABLE OF CONTENTS

ABSTRACT……...iii

LIST OF TABLES.……..……..vii

LIST OF FIGURES……ix

ACKNOWLEDGEMENTS……...xii

Chapters

1 MINERALOGICAL AND OXYGEN ISOTOPIC EVIDENCE OF WATER-ROCK INTERACTIONS IN THE COSO GEOTHERMAL SYSTEM……1

1.1 Introduction……1
1.2 Methods……..3
1.3 Results……5
1.4 Discussion……15
1.5 Conclusions……..28
1.6 References……31

2 TOURMALINE IN GEOTHERMAL SYSTEMS: AN EXAMPLE FROM DARAJAT, INDONESIA ……64

2.1 Introduction……..64
2.2 Analytical Methods……..66
2.3 Results……..66
2.4 Discussion……74
2.5 Conclusions……..78
2.6 References……80

Appendices

A. X-RAY DIFFRACTION METHODOLOGY AND MINERAL ABUNDANCES..……101

B. PREEXISTING WHOLE-ROCK OXYGEN ISOTOPE DATA……110

C. CALCULATION OF D18O VALUES OF RESERVOIR FLUIDS……...121

D. TOURMALINE MINERAL CHEMISTRY DATA…...…….124

LIST OF TABLES

Table Page

1.1 Measured $\delta^{18}O$ values for whole-rock and feldspar minerals samples from well 68-6……49

1.2 Measured $\delta^{18}O$ values for whole-rock and feldspar mineral samples from well 33A-7…….51

1.3 Measured $\delta^{18}O$ values for whole-rock and feldspar mineral samples from well 73-19……..53

1.4 Calculated equilibrium $\Delta_{r\text{-}w}$ and $\Delta_{fsp\text{-}w}$, measured $\Delta_{r\text{-}w}$ and $\Delta_{fsp\text{-}w}$, and W/R ratios for well 68-6……...58

1.5 Calculated equilibrium $\Delta_{r\text{-}w}$ and $\Delta_{fsp\text{-}w}$, measured $\Delta_{r\text{-}w}$ and $\Delta_{fsp\text{-}w}$, and W/R ratios for well 33A-7……59

1.6 Calculated equilibrium $\Delta_{r\text{-}w}$ and $\Delta_{fsp\text{-}w}$, measured $\Delta_{r\text{-}w}$ and $\Delta_{fsp\text{-}w}$, and W/R ratios for well 73-19…….61

2.1 Summary of mineral assemblages in the Darajat system……...89

2.2 Representative electron microprobe analyses (wt %) of Darajat tourmalines…...92

A.1 Summary table of bulk and clay-sized fraction XRD results given by sample for well 68-6……..104

A.2 Summary table of bulk and clay-sized fraction XRD results given by sample for well 33A-7……...105

A.3 Summary table of bulk and clay-sized fraction XRD results given by sample for well 73-19……109

B.1 Preexisting whole-rock oxygen isotope analyses from the Coso system……110

B.2 Measured $\delta^{18}O$ values for whole-rock and mineral samples from wells 68-6....118

B.3 Measured $\delta^{18}O$ values for whole-rock and mineral samples from well 33A-7...119

B.4 Measured $\delta^{18}O$ values for whole-rock and mineral samples from well 73-19....120

C.1 Necessary Information calculation of unboiled reservoir fluid ($\delta^{18}O_w{}^f$) for wells 33A-7, 68-6 and 73-19.....123

D.1 Initial oxide percentage values for tourmalines found within the Darajat geothermal system…….....125

LIST OF FIGURES

Figure Page

1.1 A simplified geologic map of the Coso Geothermal system…….35

1.2 General north-south thermal structure of the West Flank...……...36

1.3 Lithologic abundances, clay content, abundance of veining and temperature information for well 68-6…….....37

1.4 Lithologic abundances, clay content, abundance of veining and temperature information for well 33A-7……38

1.5 Lithologic abundances, clay content, abundance of veining and temperature information for well 73-19…….....39

1.6 A representative photomicrograph of a hornblende rich diorite chip……....40

1.7 A representative photomicrograph of a hornblende-biotite-quartz diorite chip…41

1.8 A representative photomicrograph of a biotite-quartz diorite chip……....42

1.9 A representative photomicrograph of a pervasively altered diorite chip……...43

1.10 A representative photomicrograph of a granodiorite chip…….44

1.11 Typical granite chips……..45

1.12 A microgranite chip cut by a calcite vein…….....46

1.13 Plan maps of the whole-rock oxygen isotope data at a series of elevation intervals in the Coso system…...……..47

1.14 Vertical cross-section of the oxygen isotope data along the north-south transect A-A'……...48

1.15 Measured $\delta^{18}O$ values of whole-rock and feldspar samples as a function of well and elevation depth for well 68-6……..50

1.16 Measured $\delta^{18}O$ values of whole-rock and feldspar samples as a function of well depth and elevation for well 33A-7……...52

1.17 Measured $\delta^{18}O$ values of whole-rock and feldspar samples as a function of well depth and elevation for well 73-19……54

1.18 Expected clay mineralogy zoning with increasing depth as a function of temperature……55

1.19 Vertical cross-section of the distribution of clay minerals (clay zones) at Coso along the transect A-A' base on XRD……...56

1.20 Oxygen isotope ($\delta^{18}O$) contours superimposed onto the cross-section of clay window distribution along the traverse A-A'……57

1.21 Evaluating departures from isotope exchange equilibrium……...62

1.22 Measured $\delta^{18}O$ values of feldspar (from wells 68-6 and 33A-7) and whole rock (from well 73-19) plotted as a function of preproduction temperatures……....63

2.1 Simplified location map of Darajat ……...83

2.2 Location maps of wells from Darajat……84

2.3 Overview of lithology in well DRJ-S1 based on petrographic observations and whole-rock XRD……85

2.4 Overview of lithology in well DRJ-18ST1 based on petrographic observations and whole-rock XRD……86

2.5 Overview of lithology in well DRJ-21 based on petrographic observations and whole-rock XRD……87

2.6 Overview of lithology in well DRJ-29 based on petrographic observations and whole-rock XRD……88

2.7 Representative photomicrograph of Stage 1 tourmalines replacing plagioclase……..90

2.8 Representative photomicrograph of Stage 3 tourmalines……..91

2.9 General chemical composition diagram based on alkali content……...…96

2.10 Compositional diagrams constructed to further classify tourmalines into accepted categories and depict possible exchange vectors……...97

2.11 Distribution of tourmaline and advanced argillic alteration assemblages…….....99

2.12 Simplified conceptual model of the evolution of the Darajat geothermal system……..100

ACKNOWLEDGEMENTS

I want to thank John Bowman for introducing me to the fascinating fields of water-rock interaction and isotope geochemistry, sharing his extensive knowledge, providing guidance when needed, and for his patience. I want to thank Joseph Moore for introducing me to geothermal systems, helping me improve my petrography skills, sharing his extensive knowledge, providing guidance when needed, and especially for his generous financial support. Many thanks to Erich Petersen for introducing me to economic geology, his constructive input, and for assisting me during my time spent as an officer with the University's Society of Economic Geology student chapter. I would be hard pressed to find three better mentors. Thanks Clay Jones and Wil Mace for assisting with the various analytic methods. A special thanks to John Valley and Mike Spicuzza at the University of Wisconsin for generously allowing me to use their facilities to generate oxygen isotope data. I would next like to thank Quintin Sahratian, Louise Spann and Diego Fernandez for their help preparing samples. A special thanks to David Langton, who located all the samples packed away in storage. I am grateful for the financial assistance provided by the Department of Energy, the University of Utah and the SEGF Graduate Fellowship Program. Next I thank my family for their love and support and instilling within me a work ethic necessary to succeed. Finally, I thank my friends for reminding me that taking an occasional break is not only acceptable, but beneficial.

# CHAPTER 1

# MINERALOGICAL AND OXYGEN ISOTOPIC EVIDENCE OF WATER-ROCK INTERACTIONS IN THE COSO GEOTHERMAL SYSTEM

## 1.1 Introduction

### 1.1.1 Background

The Coso Hot Springs Geothermal Field is located in California 10 km east of the Sierra Nevada Mountains at the western boundary of the Basin and Range Province; the field has an installed capacity of 273 MWe. A number of studies of this system have been done in order to characterize the geology and to optimize geothermal production (Duffield et al., 1980; Lutz et al., 1999; Adams et al., 2000; Manley and Bacon, 2000; Kovac, 2005). The field developed in a series of regionally metamorphosed diorite, quartz monzonite and granite intrusions of Mesozoic age (Duffield et al., 1980) (Figure 1.1). Two episodes of Cenozoic volcanism produced basalt and rhyolite at 4.0-2.5 Ma and 1.1-0.044 Ma (Duffield et al., 1980; Kurliovitch et al., 2003;). Crustal thinning from Basin and Range extension has produced a silicic magma reservoir between 5-20 km depth (Duffield et al., 1980; Reasenberg et al., 1980; Manley and Bacon, 2000) that produces heat for the current geothermal activity (Duffield et al., 1980). Surface expressions of geothermal activity include opaline sinter ($SiO_2$) and travertine ($CaCO_3$) spring deposits. $^{14}C$ dating of pollen in hot spring deposits has yielded ages of 11,550 to

8550 years (Moore, unpublished data). The present-day geothermal fluids have low salinities (5,000-10,000 ppm TDS), are NaCl-dominated and have temperatures up to 350 $^{o}$C. Geochemical and hydrogen isotope data indicate that the system is predominately recharged by meteoric fluids (Moore et al., 1990; Adams et al., 2000; unpublished results, Terra-Gen). Northerly trending, Basin and Range faulting and local dextral strike-slip faulting associated with the younger Walker Lane/Eastern California Shear Zone guide fluid flow and influence current geothermal activity (Monastero et al., 2005; Kaven et al., 2012).

### 1.1.2 Thermal Structure

Extensive borehole measurements in the Coso field define a north-south trending zone of high temperature in the western part of the field called the West Flank (Figure 1.1). Field operators used pre-exploitation temperature data from multiple wells to develop projected thermal cross-sections A-A' and B-B' along the West Flank (Figure 1.2). Reservoir temperatures in the south are higher than in the north at equivalent elevations, and maximum measured temperatures in the field exceed 350 $^{o}$C. These cross-sections provide information on pre-exploitation temperature as a function of depth for the three wells analyzed in this study. The cross-section A-A' illustrates the presence of a thermal plume that ascends in the south and then extends laterally to the north. This thermal structure implies that hot fluids ascend in the south and then migrate laterally to the north along the West Flank through subhorizontal, higher permeability zones (possibly along a northerly-trending Basin and Range fault capped with a low permeability smectite clay zone).

### 1.1.3 Objectives of the Study

Producing geothermal systems are particularly good systems to study fluid-rock interaction because the physical chemistry of the reservoir fluids can be established and extensive drilling required for field development can provide extensive geologic, geochemical and geophysical data on the reservoir host rocks. Hydrothermal alteration mineralogy and oxygen isotope compositions of whole-rock samples and feldspar mineral separates have been determined on sample cuttings from three producing wells in the Coso geothermal field. These wells are located within a north-south trending zone of high temperature (the West Flank), and preliminary oxygen isotope data (unpublished data, Terra-Gen Operating Company) suggest that these wells intersect zones of significant fluid-rock interaction. The new isotope results identify discrete zones of significant $^{18}O/^{16}O$ depletion that indicate large amounts of localized fluid infiltration, water-rock interaction and isotopic exchange (high water to rock ratio and inferred high permeability). The oxygen isotope analyses, in conjunction with clay mineral alteration, are used to better understand water-rock interaction and hydrothermal alteration in the Coso geothermal system as a function of temperature and permeability, and to enhance understanding of fracture-controlled permeability within an active geothermal system.

## 1.2 Methods

### 1.2.1 Sample Collection

Rock cuttings from regular intervals (~30 - 80 m distance part) in wells 68-6, 33A-7 and 73-19 were collected for oxygen isotope analyses, X-Ray diffraction (XRD) measurements and petrographic observations. The cutting samples were well mixed; then

2 grams were split from each sample for XRD measurements and the construction of new petrographic thin sections; a 0.5 gram split of randomized cuttings was collected for whole-rock oxygen isotope analysis, and 1 gram of cuttings, intended for mineral separate oxygen isotope analyses, was also collected.

### 1.2.2 XRD Measurements

Bulk rock mineralogy, mineral abundances, clay mineralogy and clay abundances have been determined by petrography and XRD methods at the Energy & Geoscience Institute at the University of Utah. A Broker D8 Advance X-Ray diffractometer, emitting Cu-K$\alpha$ radiation at 40 kV and 40 mA, with a 0.02$^{o}$ 2$\theta$ step size was used. A standard preparation technique for sample powders prepared from 2 gram aliquots of rock cutting samples was used for the XRD analysis (Lutz and Moore, 1997; Kovac 2005). Mineral abundances were determined following the Reitveld method using TOPAS software developed by Bruker AXS; the detection limit for clay minerals is 0.3 wt. %. Appendix A provides a more detailed description of these methods. The clay fraction was separated from the bulk sample using Stokes' Law for particle sedimentation. After an air-dried scan was performed, the sample was allowed to interact with ethylene glycol vapors to induce swelling of susceptible clays. A second scan was run and the air-dried and glycolated patterns were compared to determine which, if any, expandable clays are present.

### 1.2.3 Oxygen Isotope Measurements

New oxygen isotopic measurements were conducted at the University of Wisconsin-Madison on 91 whole-rock samples and 27 feldspar separates from wells 68-6, 33A-7 and 73-19. Minerals were separated using a Frantz magnetic separator followed by hand-picking under a stereoscopic microscope. All new analyses were done by laser-aided fluorination using a lasing sample chamber outfitted with an airlock sample chamber to prevent prefluorination of reactive rock powders (Spicuzza et al., 1998). Oxygen isotope values were standardized using UWG-2 garnet standard (Valley et al., 1995) and are reported in the standard $\delta^{18}O$ notation, relative to VSMOW.

## 1.3 Results

### 1.3.1 Lithology of the West Flank

Petrographic studies and whole-rock x-ray diffraction (XRD) analyses of drill cuttings have revealed a complex lithology consisting of diorite, granodiorite, granite, rhyolite and a trace amphibolite component throughout Coso (Duffield et al., 1980; Bishop and Bird, 1987; Lutz and Moore, 1997; Kovac, 2005). Whole-rock XRD analyses have been performed on a suite of samples collected from wells 33A-7, 68-6 and 73-19 (well locations noted in Figure 1.1) in order to provide quantitative information regarding the bulk mineralogy along the western portion of the Coso system. These XRD analyses are compiled in Appendix A.

The lithologies of wells 68-6, 33A-7 and 73-19 (deduced from petrographic observations and XRD analyses) are presented in Figures 1.3-1.5. The most common rock type present in the Coso basement is diorite (Figure 1.6). Previous mineralogical

assessments (Lutz and Moore, 1997) on the various rock types have concluded that a typical diorite in the area is composed of quartz (12-14%), plagioclase (35-38%), potassium feldspar (3-8%), micas (15-30%), hornblende (0-8%), epidote and a varying amount of chlorite; common accessory minerals include titanite, magnetite, pyrite, chalcopyrite, apatite and zircons. These diorites may be further subdivided into either hornblende-biotite-quartz diorite (Figure 1.7) or biotite-quartz diorite (Figure 1.8). Without the aid of a petrographic microscope, it is nearly impossible to distinguish the dioritic populations from one another; in Figures 1.3-1.5, diorite has been subdivided into two categories: quartz-diorite (consisting of predominately quartz-rich diorite fragments with only a minor amount of biotite), and hornblende-biotite diorite (this includes both hornblende-biotite-quartz diorite and biotite-rich quartz diorite fragments). The diorite is pervasively altered (Figure 1.9). Commonly observed amongst the alteration mineralogy are chlorite, adularia, calcite, sericite, epidote and pyrite; vein minerals include quartz, calcite, chlorite, hematite and trace amounts of epidote, pyrite and sericite. Based upon the degree of alteration and veining relationships, it is believed that the dioritic component in the system is the oldest (Moore et al., 2004).

The second most abundant rock type in the Coso basement is granodiorite (Figure 1.10). Its typical primary mineralogy is quartz (27%), plagioclase (31%), potassium feldspar (31%) and biotite (0-8%); common accessory minerals include hematite, pyrite and zircon (Lutz and Moore, 1997). The granodiorite samples are characterized by less brecciation, veining and extent of hydrothermal alteration. The extent of alteration for this component is best described as low to moderate. Observed alteration minerals include sericite, chlorite and trace calcite; minerals present in veins are calcite, quartz,

chlorite, hematite, epidote and pyrite.

Pink- to light-colored granites (Figure 1.11) present in the Coso system contain quartz (36%), plagioclase (22%), potassium feldspar (33%), micas (0-7%), calcite (3%) and chlorite (0-2%). Primary muscovite and granophyric textures present in the granite are the distinguishing features between it and granodiorite. Two distinct granite populations have been noted based upon grain-size: 1) a coarse-grained variety and 2) a fine-grained variety, best described as microgranite (Figure 1.12) or alaskite (Kovak, 2005). These granites experience very little alteration; when rare alteration in the granites is observed, secondary minerals include trace amounts of clay and calcite.

Rhyolite dikes encountered in a number of wells are believed to be associated with rhyolite domes present on the surface throughout Coso (Sugarloaf Mountain, for instance). The rhyolite is characterized by spherulitic devitrification textures and intergrowths of potassium feldspar and quartz. Occasionally silicified rhyolite fragments are observed.

Based on mineralogical and textural observations made throughout the system, it has been suggested that the oldest intrusions (primarily the dioritic phase) have been regionally metamorphosed under greenschist facies conditions in an event unrelated to geothermal activity (Duffield et al., 1980; Lutz et al., 1996; Kovac, 2005; Bartley et al., 2007). Mineralogical indicators of such an event observed in cuttings from wells related to this study include wide-spread presence of euhedral epidote and chlorite and the presence of minor actinolite in equivalent igneous rocks outside the Coso geothermal system. Textural indicators include kinked feldspar grains resulting from deformation, and locally faint foliation.

### 1.3.2 Clay Mineralogy

Clay mineral abundances were determined in samples of cuttings from wells 33A-7, 68-6 and 73-19 in the West Flank. Clay type abundances for each sample are presented in Appendix A and as a function of depth in each well in Figures 1.3-1.5.

The clay sized minerals (<5 micrometers) present along the West Flank of Coso include smectite, interlayered illite-smectite (I/S), illite, chlorite and a trace interlayered chlorite-smectite component. Clay mineralogy and abundances vary laterally but in general clay mineralogy changes from smectite to interlayered illite-smectite to illite with increasing depth in these three wells. Smectite is confined to the uppermost portions of all three wells. In wells 68-6 and 33A-7, smectite is present from the top down to an elevation between 800 and 1000 meters; abundances are between trace levels (from 0.3 to 1%) and 8.1% for 33A-7, and between 2.8% and 8.3% for 68-6. The elevation of the deepest occurrence of smectite above trace levels is used to define the base of the smectite zone in wells 68-6 and 33A-7 (Figure 1.3 and 1.4). In well 73-19, only trace levels (0.3 to 1%) of smectite are present, and smectite occurs persistently only at elevations above 469 m (Figure 1.5). We define the base of the smectite zone at this elevation (469 m) in well 73-19. Interlayered illite-smectite is present intermittently through the entirety of 33A-7, but is most prevalent immediately below the smectite zone in 33A-7, between the elevations of 640 meters and -41 meters. Small but detectable amounts of interlayered illite-smectite are present below the smectite zone in well 73-19, between 0 and -143 m elevation, and interlayered illite-smectite is completely absent in well 68-6. Illite is present at all depths in 68-6 and 33A-7, but is most abundant below -41 meters in 33A-7 and below 700 meters in 68-6. Illite abundance is between 1.0% and

15.8% in 68-6 and between trace levels (0.3%) and 14.3% in 33A-7. Illite is present throughout the entire length of well 73-19, but is most prominent below -143 meters, with abundances between 1.1% and 11.0%. Hence, the illite zone occurs in the deepest parts of all three wells, beneath the smectite or interlayered illite-smectite zones. Clay sized chlorite is abundant at all elevations throughout the entire West Flank.

### 1.3.3 Whole Rock Oxygen Isotope Characteristics of the Coso Geothermal System

The operating company for Coso, Terra-Gen, has made available 513 whole-rock $\delta^{18}O$ analyses of well-cuttings from the Coso geothermal field. These analyses (Appendix B), plus 91 additional whole-rock $\delta^{18}O$ values measured in this study (Tables 1.1-1.3), define general patterns of $\delta^{18}O$ variation in the Coso geothermal field. These results have been used to construct plan maps of $\delta^{18}O$ variations for a series of depth intervals (480 m) within the Coso field (Figure 1.13). These plan maps were constructed by averaging the isotopic values within the 480 m intervals in each well; sufficient analyses were not available deeper than 1125 m below sea-level to construct a useful plan map. Near surface $\delta^{18}O$ values (surface to 800 m elevation) are consistent with, or slightly lower than, measured $\delta^{18}O$ values for primary igneous rock in the Central Sierra Nevada Batholith (+7.5 ‰ to +8.0 ‰) except for depletion to $\delta^{18}O$ values between +5 ‰ and +6 ‰ in the northwest quadrant of the system. With increasing depth, significant and widespread decreases in $\delta^{18}O$ occur only in the northwest quadrant, where $\delta^{18}O$ values can decrease down to values between 0 and +1 ‰ (-645 to -1125 m depth interval).

Regardless of depth, the diorite host rock in most of the southern half of the reservoir does not experience significant $^{18}O/^{16}O$ depletion below +6 ‰.

Variations in whole-rock $\delta^{18}O$ values along the vertical section A-A' along the north-south trending thermal high in the West Flank of the Coso field (Figure 1.1) are illustrated in Figure 1.14. This cross-section was constructed using whole-rock data from nine wells along or close to this A-A' traverse (see Figure 1.1). Depletions in $^{18}O/^{16}O$ are more extensive and extend to significantly greater depth in the northern portion of the cross-section. Maximum depletions to $\delta^{18}O$ values below 0 ‰ occur in the northern wells 68-6 and 33A-7 in the elevation interval of -1000 to -1800 m. In contrast, host rocks in the southern part of the traverse are not significantly depleted except for two or three discrete intervals in wells 73-19 and 58A-18.

To facilitate comparison of temperature and $\delta^{18}O$, the isotherms from the thermal cross-section along A-A' (Figure 1.2) are superimposed on this $\delta^{18}O$ cross-section. It is apparent that preproduction temperatures and whole-rock $\delta^{18}O$ are not in general well correlated. With the few localized exceptions noted above, host rock is not depleted in $^{18}O/^{16}O$ to any significant extent in the southern part of the traverse, even within the deeper, higher T levels. In the northern part of the section, hotter host rocks below -1400 m are less depleted in $^{18}O/^{16}O$ than cooler rocks immediately above (between -1000 and -1400 m). The absence of close and consistent correlation between T and whole-rock $\delta^{18}O$ value suggests that additional factors such as permeability play a role in controlling the extent of fluid-rock interaction—and hence extent of $^{18}O/^{16}O$ depletion—in the Coso geothermal system.

### 1.3.4 Oxygen Isotope Characteristics of Reservoir Host Rock and Mineral Separates in the West Flank

Based upon the previous whole-rock oxygen isotope analyses (Appendix B) and measured temperature (preproduction) distribution in the system (unpublished data, Terra Gen Company), three wells (33A-7, 68-6 and 73-19) were selected for detailed oxygen isotope analyses of whole-rock and mineral separates (Tables 1.1-1.3). These wells are located in the West Flank of the Coso field within the north-south trending zone of high temperature within the field (Figure 1.1), and help define traverse A-A'. Previous oxygen isotope data (unpublished data, Terra-Gen Operating Company) document significant $^{18}O/^{16}O$ depletions in the northwest quadrant of the field, and particularly in well 68-6, suggesting that this well intersects zones of significant fluid-rock interaction. The new results from wells 68-6, 33A-7 and 73-19 (Tables 1.1-1.3) identify specific zones of significant $^{18}O/^{16}O$ depletion that indicate increased fluid infiltration, fluid-rock interaction and isotopic exchange (zones of inferred high permeability). Oxygen isotope analyses were also made of feldspar mineral separates; these and the whole-rock analyses are used to evaluate water-rock interaction as a function of temperature and permeability in the Coso geothermal system.

#### 1.3.4.1 Whole Rock $\delta^{18}O$ Analyses

The dioritic to granodioritic rocks from the region that are equivalent to the reservoir host rocks in the Coso system have primary whole-rock $\delta^{18}O$ values (relative to VSMOW) of +7.5 to 8.0 ‰ (Masi et al., 1981; Lackey et al., 2008). In well 68-6 (Figure 1.15), whole-rock $\delta^{18}O$ values are somewhat to moderately depleted in $^{18}O/^{16}O$ relative to

primary igneous values, and fluctuate between 1.8 ‰ and +6.02 ‰ down to ~2000 meters depth, with a tendency to decrease with depth. Below 2000 meters, $^{18}O/^{16}O$ depletions are even greater, and the maximum $\delta^{18}O$ value is +3.0, with most $\delta^{18}O$ values below +1 ‰. Whole-rock $\delta^{18}O$ values reach a minimum of -4.60 ‰ at a depth of 2941 meters (Figure 1.15). In well 33A-7 $\delta^{18}O$, values generally decrease with depth from a maximum value of +7.62 ‰ at 33.5 meters depth to a minimum of -3.08 ‰ at 2529.8 meters, just above the production zone in the well (Figure 1.16). Immediately below, and to the bottom of the well, $\delta^{18}O$ values are significantly higher, ranging between +3 to +4.9 ‰, but are still significantly lower than primary igneous values. The igneous host rocks in well 73-19 are less depleted in $^{18}O/^{16}O$ compared to the rocks of the other two wells (Figure 1.17). The highest measured $\delta^{18}O$ values from whole-rock samples overlap primary igneous $\delta^{18}O$ values of +7.5 to 8.0 ‰ (Masi et al., 1981; Lackey et al., 2008). The only $\delta^{18}O$ values below +5 ‰ occur at depths of 1386.8 m and below. The minimum $\delta^{18}O$ value in well 73-19 is still positive, +2.38 ‰ (1411.2 meters depth, Fig. 8). In all three wells, samples with the lowest measured $\delta^{18}O$ values (or with $\square^{18}O_{wr} \leq 2.0$ ‰, well 33A-7) correspond with major intervals of lost circulation, the primary production intervals for each well (Figs. 1.15-1.17).

1.3.4.2 Feldspar Oxygen Isotope Characteristics

Measured $\delta^{18}O$ in bulk feldspar separates range from 6.76 ‰ to -3.88 ‰ in well 68-6 and from 7.50 ‰ to -2.37 ‰ in well 33A-7; feldspars from well 73-19 have higher $\delta^{18}O$ values ranging from 8.12 ‰ to 6.14 ‰. In all three wells, the $\delta^{18}O$ values of feldspar correlate positively with the whole-rock $\delta^{18}O$ values, and are systematically 1 to

3 ‰ higher than the whole rock values, even in the more $^{18}O/^{16}O$ -depleted samples (Figures 1.15-1.17) with one exception in 33A-7(2471.9 m). Feldspar should be enriched in $^{18}O/^{16}O$ relative to the whole-rock value in unaltered diorite. However, this is not typical for igneous rock experiencing at least the initial stages of interaction with $^{18}O/^{16}O$-depleted meteoric waters (Garlick and Epstein, 1967; Taylor and Forester, 1979; Criss and Taylor, 1983). The bulk feldspar separates are mixtures of primary igneous feldspar and feldspar that has experienced oxygen isotope exchange with geothermal fluid (hydrothermal feldspar). The hydrothermal feldspar should have considerably lower $\delta^{18}O$ value than primary feldspar, owing to the low $\delta^{18}O$ value of the geothermal fluid and intermediate T of exchange ($\leq$350$^{o}$C). Further, feldspar is normally more susceptible to oxygen isotope exchange compared to hornblende and less abundant quartz in the host diorite and quartz diorite (Taylor and Forester, 1979; Criss and Taylor, 1983; Cole et al., 1992). As a result, hydrothermal feldspar might be expected to have a $\delta^{18}O$ value less than that of the whole rock for rocks that are only moderately depleted in $^{18}O/^{16}O$. In thin section, primary igneous feldspar is clear and twinned; hydrothermal feldspar is cloudy and sometimes turbid from the presence of very small grains of clay minerals. The intergrown nature of primary and hydrothermal feldspar at the grain scale makes their effective separation by standard density means impractical. However, a concentrate of cloudy-looking feldspar was made by hand picking the bulk feldspar separate from sample 2941.3 (well 68-6). Analysis of this concentrate yielded a $\delta^{18}O$ value of -5.1 ‰, significantly lower than the $\delta^{18}O$ values of the bulk feldspar (-3.9 ‰) and whole rock (-4.6 ‰) from this sample (Table 1.1). In-situ (SIMS) analysis will be necessary to define clearly the $\delta^{18}O$ value of hydrothermal feldspar in the host rock. Regardless, this

systematic difference between measured $\delta^{18}O$ values of bulk feldspar and whole rock, despite significant differences in the extent of fluid-rock interaction, suggests that the $\delta^{18}O$ values of both feldspar and whole rock reflect the extent of interaction (and oxygen isotopic exchange) between host rock and geothermal fluid in the Coso system.

Another possibility for the systematic $^{18}O/^{16}O$ enrichment in bulk feldspar relative to whole rock is that the lower $\delta^{18}O$, hydrothermally altered feldspar was preferentially removed by crushing during preparation of the sample aliquots (>80 or >100 mesh size) from the whole rock used to make plagioclase separates. To test this possibility, additional analyses were made of feldspar separated out of the finer-grained (150 to 200 mesh) residual fraction of the whole-rock aliquots for two samples. The analyzed $\delta^{18}O$ values for these finer-grained feldspar separates are -4.12 ‰ (compared to -3.88) for sample 2941.3, well 68-6 and +0.63 ‰ (compared to -0.03) for sample 2529.8, well 33A-7 (Table 1.1,1.2). Feldspar separates from these finer-grained fractions are not significantly lower in $\delta^{18}O$ compared to feldspar separates from the coarser-grained fractions.

The systematically higher measured $\delta^{18}O$ values of feldspar relative to whole rock indicate from mass balance that there is at least one other major phase (likely chlorite and/or other clay mineral alteration products) in the rock that is significantly depleted in $^{18}O/^{16}O$ relative to the whole-rock value. Chlorite can replace hornblende but would be stable with biotite during the greenschist facies conditions of the earlier regional metamorphism; this generation of chlorite will not be related to geothermal activity. Replacement of biotite by chlorite would likely occur only at the subgreenschist facies conditions of the Coso geothermal environment. Hence, bulk separates of chlorite will

potentially contain two generations of chlorite of very different $\delta^{18}O$ value. Further, good separation of bulk samples of chlorite by magnetic and density methods proved impractical owing to the intergrowth of chlorite with biotite and hornblende at the grain size scale. Therefore, concentrates of chloritized biotite were hand picked from four samples. Their $\delta^{18}O$ values, compared to whole-rock values (in parentheses) are: 1) 0.16 ‰ (3.78), sample 1700.8, well 68-6; 2) -3.18 ‰ (0.75), sample 2709.7, well 68-6; 3) -3.83 ‰ (-3.08), sample 2529.8, well 33A-7; and 4) -0.45 ‰ (4.61), sample 1386.8, well 73-19. These chloritized biotites are from almost 1 to as much as 5 ‰ depleted in $^{18}O/^{16}O$ relative to the whole rock values, satisfying at least qualitatively this mass balance requirement. In-situ analyzes will be necessary to define the $\delta^{18}O$ values of the hydrothermal chlorite more precisely. See Appendix B for the complete dataset.

## 1.4 Discussion

### 1.4.1 Clay Mineralogy as a Function of Fluid-Rock Interaction

Previous studies of geothermal systems (Steiner, 1968; Henley and Ellis, 1983; Browne, 1984; Reyes, 1990) have concluded that clay mineralogy changes from smectite to illite with increasing temperature. Smectites associated with the shallow clay cap of a geothermal field remain stable to a maximum temperature of 180 $^{o}$C; when temperatures exceed 180 $^{o}$C, smectites begin converting to illite until temperature reaches ~225 $^{o}$C, where conversion to pure illite is complete. As a result, clay mineralogy often changes systematically in geothermal systems and defines smectite, interlayered illite-smectite and illite zones with increasing depth (Figure 1.18).

The actual distribution of clay minerals and preproduction temperatures with

depth along the cross-section A-A' at Coso is shown in Figure 1.19. Boundaries between clay zones are based upon the lowest elevation in each well where the clay mineral identifying each zone is still abundant or persistent, as seen in Figures 1.3-1.5. Clay mineralogy changes with increasing depth from smectite to interlayered illite-smectite to illite, or directly to illite (well 68-6) in these wells. This distribution with depth suggests that at least the smectite and interlayered illite-smectite zones are a function of increasing temperature and the result of geothermal activity. However, illite is present at all elevations in these three wells; its presence at shallow depths probably reflects an older regional metamorphic event occurring at greenschist facies conditions. The presence of chlorite and epidote with this illite at shallow depths in all three wells necessitates temperatures exceeding 250 $^{o}$C (Browne, 1978; Henley and Ellis, 1983; Reyes, 1990) from the surface downward, incompatible with present-day geothermal temperatures (Figure 1.2). Therefore, hydrothermal alteration associated with geothermal activity has likely superimposed smectite and interlayered I/S zones onto the host rock, but has not completely converted pre-existing illite within these zones.

Figure 1.19 shows that the observed clay mineral distributions along A-A' are not closely correlated with the temperature-dependent clay mineral distribution expected from preproduction temperature distribution. In well 68-6 smectite disappears near 180$^{o}$C (at an elevation of ~1000 meters), close to its maximum thermal stability. However, no transition zone of I/S is present, despite temperature not reaching 225$^{o}$C until -40 meters elevation. In 33A-7, smectite abundance noticeably diminishes at 1000 meters where the temperature is only 123$^{o}$C, and 180$^{o}$C is not encountered in well 33A-7 until 590 meters elevation, in the middle of the interlayered illite-smectite zone. At the lowest elevation

(-41 meters) where interlayered I/S is still abundant in 33A-7, temperature is 197 $^{o}$C, and 225 $^{o}$C is not encountered until an elevation of -683 meters. Trace smectite and interlayered I/S exist within the illite zone in 33A-7 (Figure 1.4). These clay minerals likely formed during an earlier, lower temperature geothermal event; either insufficient time has passed since current high temperature conditions were imposed to completely convert these clays to illite, or kinetic barriers prevented complete conversion. In well 73-19, smectite disappears below 460 meters, a point where temperature is not much above 180 $^{o}$C, but interlayered I/S is detected down to an elevation of ~ -140 meters where temperature approaches 300 $^{o}$C. These discrepancies indicate that temperature variations alone cannot explain the details of clay mineral distribution patterns in the reservoir rock along traverse A-A'. These discrepancies may indicate that the preproduction thermal regime was younger and different from that responsible for clay mineral zoning, and this zoning has not yet readjusted to new thermal conditions. However these discrepancies may also suggest that parameters in addition to temperature are controlling the stability and spatial distribution of clay minerals with depth along the vertical cross-section A-A' in the Coso system.

Additional physical-chemical processes associated with fluid-rock interaction, such as fluid chemistry (including pH), heating rate and the fluid/rock ratio (a function of permeability), may influence the smectite to illite transformation. Patrier et al. (1996) show that in the Chipilapa Geothermal system, both illite and smectite formed at similar temperatures and at temperatures exceeding that (225$^{o}$C) normally viewed as the upper limit for smectite stability. These authors attribute these occurrences to a broad-scale reduction in permeability over time; initially, both smectite and illite precipitated in

response to high permeability [high water (W)/rock (R) ratio] conditions, followed by a second generation of smectite (currently precipitating) in lower permeability "closed micro-systems."

Variations in reaction progress resulting from variations in permeability may be playing a role in clay mineralization in the Coso system. Clay mineral abundances, particularly of smectite, increase from south to north in the system. In well 73-19, smectite abundances only reach a maximum of 0.3 % whereas in wells 68-6 and 33A-7 to the north, smectite abundances exceed 8 %. Hence, reaction progress—and the extent of fluid-rock interaction—increases from south to north; this increase correlates with the progressively shallower depth at which smectite disappears and with the thinning and eventual disappearance of the I/S transition zone. Increased fluid-rock interaction—possibly reflecting an increase in permeability—would increase smectite reaction progress, resulting in higher smectite abundances and disappearance of interlayered illite-smectite to the north. In contrast, the lower extent of reaction progress recorded in well 73-19 likely leaves temperature as the primary influencing factor on clay mineralogy in this southern well.

Another monitor of the extent of fluid-rock interaction—and hence permeability—is the extent of $^{18}O/^{16}O$ depletion experienced by the host rock. A comparison between clay mineralogy and whole rock $\delta^{18}O$ values along the cross-section A-A' is shown in Figure 1.20. The host rocks are systematically more depleted in $^{18}O/^{16}O$ at depth at the north end compared to the south end of the traverse. In addition, significant $^{18}O/^{16}O$ depletions extend to markedly shallower depth at the north end of A-A', where the smectite zone is shallowest and no I/S transition zone is present. As a

consequence, whole-rock $\delta^{18}O$ values are usually lower in rocks with illite than in rocks with smectite or mixed I/S clays. For 33A-7, the average measured $\delta^{18}O$ whole-rock value within the smectite zone is 6.0 ‰, the interlayered illite-smectite zone has an average value of 3.5 ‰, and the average value within the illite zone is 2.2 ‰. In well 68-6, the smectite zone has an average value of 4.5 ‰ and the illite zone has an average $\delta^{18}O$ value of 1.3 ‰. Because the overall extent of $^{18}O/^{16}O$ depletion in the south third of the traverse is considerably less, variations of $\delta^{18}O$ with clay mineralogy within well 73-19 are less systematic; the smectite zone has an average value of 6.8 ‰ and the illite-smectite zone has an average $\delta^{18}O$ value of 5.1 ‰, but the illite zone has an average value of 5.4 ‰. Figure 1.20 shows that there is a general correlation between greater and more widespread $^{18}O/^{16}O$ depletion in the north end of A-A' with more abundant smectite, a thinner smectite zone and the lack of a mixed I/S transition zone. The greater $^{18}O/^{16}O$ depletion of the rocks in the north part of A-A' indicates that these rocks have experienced greater fluid-rock interaction, which would also drive the smectite to illite reaction further to completion, controlling at least in part the spatial distribution of clay minerals and zoning patterns in the traverse A-A'. The greater extent of fluid-rock interaction and clay mineral reaction progress suggests that reservoir rocks at the north end of A-A' are characterized by higher permeability.

### 1.4.2 Oxygen Isotope Exchange and Fluid-Rock Interaction in the Coso Reservoir

The $\delta^{18}O$ values of the whole-rock samples from the West Flank range widely from -4.60 ‰ to 7.62 ‰ (Tables 1.1-1.3). With the exception of well 73-19, reservoir

rock in wells 33A-7 and 68-6, except for the shallowest levels, has experienced at least modest $^{18}O/^{16}O$ depletions ($\delta^{18}O$ <5.0‰) from primary igneous $\delta^{18}O$ values (+7.5 to 8.0‰). Hence, most of the reservoir rock sampled in these two wells has experienced at least some interaction and oxygen isotope exchange with the geothermal reservoir fluid derived from low $\delta^{18}O$ local meteoric water. Further, a few discrete intervals in wells 33A-7 and 68-6 have experienced significantly greater $^{18}O/^{16}O$ depletion, and have negative whole-rock $\delta^{18}O$ values ranging as low as -4.60‰.. These discrete intervals have experienced much greater fluid-rock interaction and oxygen isotope exchange with significant amounts of the geothermal fluid.

The extent of $^{18}O/^{16}O$ depletion in any given rock will be a function of the amount of reservoir fluid with which the rock has interacted, temperature and the degree to which isotope exchange equilibrium is attained. Use of reactive transport models for oxygen isotopes (Baumgartner and Rumble, 1988; Bowman and Willett, 1991; Bowman et al., 1994; Cook et al., 1997; Baumgartner and Valley, 2001) has potential to constrain fluid fluxes, which are related functionally to porosity and permeability. However, application of such models in interpreting isotopic shifts requires knowledge of flow geometry and the position of the Coso geothermal reservoir along the principal flow paths of the entire Coso hydrothermal system, information that is not yet available. Absent such information, estimates of the minimum amounts of fluid involved in hydrothermal alteration can be made using conventional box models of mass balance to compute water (W) to rock (R) ratios (Taylor, 1971).

Calculations of box model W/R ratios involve several assumptions, and it is important to understand how these assumptions place limitations on their interpretation.

Both closed- and open-system box model endmembers (Taylor, 1971; Criss and Taylor, 1986) assume attainment of exchange equilibrium between rock and fluid. Incomplete exchange yields less $^{18}O/^{16}O$ depletion in a rock; this will result in lower calculated W/R ratios. Departures from equilibrium may be important in geothermal systems that form at temperatures less than 300 $^{o}C$, and particularly so in their shallow, lower temperature sections. A second limitation is that box model W/R calculations do not account for the isotopic modification that the fluid undergoes along segments of its flow paths leading to the local site of hydrothermal alteration and isotopic exchange (Baumgartner and Rumble, 1988; Bowman and Willett, 1991; Bowman et al., 1994). The impact from this prior exchange history of the fluid is that box model W/R ratios will underestimate actual W/R ratios. As a result, calculated box model W/R ratios should be regarded as minimum estimates of the amounts of fluid involved in hydrothermal alteration and isotopic exchange at specific sites within hydrothermal flow systems. However, as long as the infiltrating fluid is chemically (isotopically) reactive, and therefore capable of inducing $^{18}O/^{16}O$ depletions in the infiltrated rocks, then variations in the extent of $^{18}O/^{16}O$ depletion in rocks from local segments of a hydrothermal flow system will qualitatively reflect variations in fluid fluxes. Under these circumstances, differences in calculated W/R ratios would also be qualitative guides to the relative amounts of fluid involved in alteration and isotopic exchange—and hence to relative differences in permeability—at specific sites within hydrothermal systems.

Both closed and open system box models (Taylor, 1971; Criss and Taylor, 1986) have been used to calculate W/R (atomic oxygen) ratios. The $\delta^{18}O$ and $\delta D$ values for Coso reservoir fluids are determined using measured $\delta^{18}O$ and $\delta D$ values of both

separated vapor (steam) and liquid water (unpublished data, Terra-Gen Operating Company) and calculating a steam fraction (based on measured T and enthalpy data), following the heat and mass balance calculations described by Truesdell (1984). See Appendix C for calculations. The $\delta^{18}O$ value of local meteoric water with similar δD to the reservoir fluids is ~ -13‰ (unpublished data, Terra-Gen Operating Company). The results of both sets of W/R calculations are presented in Tables 1.4-1.6. The $\delta^{18}O$ measurements (and W/R ratio calculations) identify a limited number of localized intervals of much more extensive $^{18}O/^{16}O$ depletion within the reservoir host rocks that have interacted and exchanged isotopically with significantly larger quantities of geothermal fluid (higher calculated W/R ratios) at some point in time. Well 33A-7 has three such intervals of locally higher calculated W/R ratio at 2502.4 - 2529.8 meters [$(W/R)_c$ = 1.94]; at 871.7 meters [$(W/R)_c$ = 1.35]; and at 109.7 meters [$(W/R)_c$ = 0.71]. Well 68-6 has one interval at 2941.3 meters that is characterized by much higher W/R ratio [$(W/R)_c$ = 2.45] than elsewhere in the well. In general, calculated W/R ratios for well 73-19 are lower than for the other two wells. However, locally higher W/R ratios (closed system) are computed for depths of 1856.2 (0.57), 1834.9 (0.57), 1411.2 (0.70) and 546 (0.28) meters in well 73-19.

In wells 33A-7 and 68-6, depths of current reservoir fluid production (lost circulation and known, high permeability) correspond to one or more of these intervals of significant $^{18}O/^{16}O$ depletion—and high W/R ratio (Figures 1.6 and 1.7). These correspondences demonstrate for the first time, as far as the author is aware, that $^{18}O/^{16}O$ depletions reflect permeability in a developed geothermal system. The presence of the limited number of discrete intervals of significant $^{18}O/^{16}O$ depletion (and high calculated

W/R ratios) in the three wells reflect discrete zones of much higher permeability within large masses of much lower permeability (much less $^{18}O/^{16}O$ depleted) rock. This spatial pattern is consistent with fluid flow and resulting fluid-rock interaction focused along discrete zones, likely fractures, and therefore large-scale permeability within the Coso rock reservoir is likely fracture-controlled.

### 1.4.3 The Extent of Isotope Exchange Equilibrium Accompanying Fluid-Rock Interaction

Because preproduction temperatures are known and the $\delta^{18}O$ value of reservoir fluids can be determined at Coso, the extent of exchange equilibrium between the geothermal fluid and feldspar in the reservoir host rock achieved through fluid-rock interaction can be evaluated. This can be done by calculating the equilibrium fractionation between feldspar and fluid (equilibrium $\Delta_{fsp\text{-}w}$) and comparing these values to the measured difference in $\delta^{18}O$ between feldspar and fluid (measured $\Delta_{fsp\text{-}w}$) (Tables 1.4-1.6). If feldspar has incompletely exchanged oxygen isotopes with the low $\delta^{18}O$ geothermal fluid, measured $\Delta_{fsp\text{-}w}$ values will be greater than equilibrium $\Delta_{fsp\text{-}w}$ values. The greater this difference, the farther from exchange equilibrium the feldspar. The equilibrium fractionation factors are calculated at temperatures measured in the wells prior to production, using the experimental calibration for oxygen isotope fractionation between plagioclase and water from O'Neil and Taylor (1967) and a plagioclase composition of $An_{25}$ (average of measured feldspar compositions in Coso reservoir rocks).

Figure 1.21a depicts the measured $\delta^{18}O$ value of feldspar plotted against the

difference between measured $\Delta_{fsp\text{-}w}$ and equilibrium $\Delta_{fsp\text{-}w}$ values for the feldspar. This figure illustrates two key aspects of the data. First, the measured $\Delta_{fsp\text{-}w}$ values for most of the sampled intervals are larger than equilibrium $\Delta_{fsp\text{-}w}$ values at preproduction measured temperatures and plot to the right of the dashed line (where measured $\Delta_{fsp\text{-}w}$ = equilibrium $\Delta_{fsp\text{-}w}$) in Figure 1.21a. This difference indicates that feldspars from most of the sampled intervals in these three wells have not completely exchanged with the geothermal fluid. Two groups of samples with measured $\Delta_{fsp\text{-}w}$ values less than equilibrium $\Delta_{fsp\text{-}w}$ are exceptions. The three feldspar samples with $\delta^{18}O$ values >7.0‰ come from the shallowest, lowest temperature intervals of wells 33A-7 and 73-19 and have experienced little or no $^{18}O/^{16}O$ depletion relative to their primary igneous $\delta^{18}O$ values. These feldspars have not experienced any significant interaction with geothermal fluid, and therefore are far from exchange equilibrium with the geothermal fluid (large measured $\Delta_{fsp\text{-}w}$). However, given the low temperatures for these three samples, equilibrium $\Delta_{fsp\text{-}w}$ values are even larger. The second exception where measured $\Delta_{fsp\text{-}w}$ values are less than equilibrium $\Delta_{fsp\text{-}w}$ values are the two most $^{18}O/^{16}O$ depleted feldspars that are from wells 33A-7 and 68-6. These two samples are discussed in a later section.

Figure 1.21a also shows that in general, the lower the $\delta^{18}O$ value of the feldspar, the closer the feldspar approaches exchange equilibrium with the geothermal fluid (e.g., measured $\Delta_{fsp\text{-}w}$ approaches equilibrium $\Delta_{fsp\text{-}w}$). This positive correlation indicates that the feldspar moves progressively toward oxygen isotope exchange equilibrium with the geothermal fluid as the extent of fluid-rock interaction increases (as indicated by progressively greater $^{18}O/^{16}O$ depletion in the feldspar and higher calculated W/R ratio). Experimental studies and theoretical considerations indicate that the rate of oxygen

isotope exchange accompanying the types of surface reactions responsible for producing hydrothermal alteration minerals at Coso increases with increasing surface area (Cole and Chakraborty, 2001). The positive correlation between progressive $^{18}O/^{16}O$ depletion in the feldspar and increasing approach to oxygen isotopic exchange equilibrium (measured $\Delta_{fsp\text{-}w}$ approaches equilibrium $\Delta_{fsp\text{-}w}$) observed for most of the feldspar samples suggests that increases in permeability of the reservoir host rock increase surface area of host rock exposed to geothermal fluid. This increase in surface area would likely play an important role in promoting fluid-rock interaction and isotopic exchange between geothermal fluid and reservoir host rock.

Rates of isotopic exchange accompanying hydrothermal alteration also increase dramatically with increase in temperature (Cole and Chakraborty, 2001). However, there is no systematic correlation of preproduction temperature with the extent of exchange equilibrium between feldspar and reservoir fluid (Figure 1.21b). In fact for most of the sample population, aside from the exceptions noted earlier, the extent of exchange equilibrium between feldspar and reservoir fluid generally decreases with increasing T. The excess of measured $\Delta_{fsp\text{-}w}$ compared to equilibrium $\Delta_{fsp\text{-}w}$ for feldspar samples from well 68-6 is clearly independent of temperature from 180 $^{o}$C to 265 $^{o}$C; for example, across the temperature range of 225-265 $^{o}$C, the difference between measured $\Delta_{fsp\text{-}w}$ and equilibrium $\Delta_{fsp\text{-}w}$ goes from 6.5 down to -1.78 and then back up to 4.1. A similar situation holds for samples from well 33A-7 over the T interval from 190 $^{o}$C to 250 $^{o}$C; the excess of measured $\Delta_{fsp\text{-}w}$ over equilibrium $\Delta_{fsp\text{-}w}$ ranges from 3.6 down to -1.7 and then abruptly back up to 5.

### 1.4.4 Thermal and Oxygen Isotope Evolution of Geothermal Fluids in the Coso System

The three lowest $\delta^{18}O$ feldspar samples are highly depleted in $^{18}O/^{16}O$, and therefore have experienced extensive fluid-rock interaction and oxygen isotope exchange. However, for the two feldspar samples with lowest $\delta^{18}O$, measured $\Delta_{fsp-w}$ values are less than equilibrium $\Delta_{fsp-w}$ values (Figure 1.21a). Measured $\Delta_{fsp-w}$ in well 33A-7 at 2471.9 m (depth of the most $^{18}O/^{16}O$ depleted feldspar sample) is 5.12 ‰, whereas equilibrium $\Delta_{fsp-w}$ for the current measured temperature (preproduction) of 246 $^{o}$C is 6.78 ‰. In well 68-6, the measured $\Delta_{fsp-w}$ at 2941.3 m (depth of the most $^{18}O/^{16}O$ depleted feldspar sample) is 4.79 ‰, whereas the equilibrium $\Delta_{fsp-w}$ for the preproduction temperature of 251 $^{o}$C is 6.57 ‰. Given the temperature conditions of the Coso system, incomplete isotopic exchange would produce measured $\Delta_{fsp-w}$ values greater than equilibrium $\Delta_{fsp-w}$ values. Therefore these discrepancies cannot result from incomplete oxygen isotope exchange between the current geothermal fluid and the reservoir rocks (because of either slow isotopic exchange kinetics or lack of physical contact between fluid and feldspar crystals – low permeability). For measured $\Delta_{fsp-w}$ to be less than equilibrium $\Delta_{fsp-w}$ for these two samples requires that the isotopic exchange took place either at higher temperature than current values and/or with a reservoir fluid of lower $\delta^{18}O$ value.

In Figure 1.22, measured $\delta^{18}O$ values of feldspar or whole rock (well 73-19) are plotted at preproduction temperatures for these samples. For comparison, curved lines define the calculated $\delta^{18}O$ values of feldspar (or whole rock) in equilibrium with a range of $\delta^{18}O$ values of geothermal fluid, including current values (solid line), as a function of temperature. Figure 1.22 illustrates the reservoir conditions necessary to obtain feldspar

(whole rock)-fluid equilibrium. Temperatures would need to increase by 48 $^{o}$C (to 299 $^{o}$C) and 42 $^{o}$C (to 288 $^{o}$C) in wells 68-6 and 33A-7, respectively, for the most $^{18}O/^{16}O$–depleted feldspars to be in exchange equilibrium with the current reservoir fluid from each well. Alternatively, the $\delta^{18}O$ values of geothermal fluids would need to decrease by 1.78 ‰ and 1.66 ‰ in 68-6 and 33A-7, respectively, to achieve equilibrium conditions with these feldspars at preproduction temperatures (Tables 1.4,1.5; Figure 1.22). Lower $\delta^{18}O$ value of the reservoir fluid in the past implies a decrease in the initial $\delta^{18}O$ value of the meteoric water source (owing to a cooler climate), an increase in the W/R ratio (and permeability) for these sections of the geothermal system, or some combination of these changes.

The situation for well 73-19 is opposite that in wells 33A-7 and 68-6 and may offer some insights into these possible changes. A $\delta^{18}O$ analysis for feldspar from the most $^{18}O/^{16}O$ depleted interval in well 73-19 is not available. However, the measured difference in $\delta^{18}O$ between the whole rock and reservoir fluid ($\Delta_{r-w}$) in well 73-19 at this depth (1411.2 m) is 7.94 ‰, <u>greater</u> than the equilibrium $\Delta_{r-w}$ value of 5.0 ‰ for the measured, preproduction temperature of 282 $^{o}$C at this depth (Table 1.6). This difference is opposite those for the most $^{18}O/^{16}O$ depleted intervals in wells 68-6 and 33A-7 and requires opposite changes in T and $\delta^{18}O$. The situation of measured $\Delta_{r-w}$ exceeding equilibrium $\Delta_{r-w}$ for well 73-19 requires that the temperature of exchange was 75 $^{o}$C <u>lower</u> than preproduction values, that the $\delta^{18}O$ value of the reservoir fluid was 3 ‰ <u>higher</u>, or that this discrepancy reflects incomplete isotopic exchange between rock and reservoir fluid, or some combination of these factors. Increase in the $\delta^{18}O$ value of the reservoir fluid would require either an increase in the $\delta^{18}O$ value of the meteoric water

source from climate changes or a decrease in W/R ratio (decrease in permeability). However, climate change seems to be a less plausible cause of the discrepancies between measured $\Delta_{r\text{-}w}$ and equilibrium $\Delta_{r\text{-}w}$ in these three wells, because the required change in the $\delta^{18}O$ value of the reservoir fluid in well 73-19 is in the opposite direction from that required to explain the discrepancies in wells 33A-7 and 68-6. Instead, these discrepancies suggest that portions of the West Flank of the Coso geothermal system (represented by wells 68-6 and 33A-7) were hotter and/or characterized by higher W/R ratio (higher permeability) during the fluid-rock exchange in the past. The opposite discrepancy recorded in well 73-19 suggests that fluid-rock interaction in this well was characterized by incomplete oxygen isotope exchange, either from kinetic barriers to isotopic exchange (from lower T in the past?) or limited physical contact between reservoir fluid and rock owing to lower permeability, or both. The extent of $^{18}O/^{16}O$ depletion measured in whole rock samples in well 73-19 is smaller in comparison to $^{18}O/^{16}O$ depletion in the other two wells (Table 1.3, Fig. 1.17), compatible with either of these factors.

## 1.5 Conclusions

Clay mineral alteration and $^{18}O/^{16}O$ depletion measured in whole-rock samples and feldspar separates along the West Flank of the Coso geothermal system record varying degrees of fluid-rock interaction in the reservoir host rocks, and provide insights into the role of fracture-controlled permeability in driving fluid-rock interaction in crystalline rocks. Observed clay mineral distribution along, and with depth, in the West Flank is not closely correlated with the distribution expected from measured,

preproduction temperature profiles. This discrepancy could indicate that clay mineral zoning has not had sufficient time to adjust to imposition of a new thermal regime in the West Flank. However, there is a general correlation toward the north along the West Flank of greater and more widespread $^{18}O/^{16}O$ depletion (indicating greater extent of fluid-rock interaction) with greater abundance of clay mineral alteration (higher reaction progress), a thinner smectite zone and ultimately the absence of a mixed I/S transition zone. These correlations suggest that clay mineral distribution in the Coso field is a function of both the extent of fluid-rock interaction and temperature.

Detailed oxygen isotope analyses of whole rock and feldspar samples from three wells along the West Flank show that the reservoir rocks have experienced a wide range of $^{18}O/^{16}O$ depletion, from negligible depletion below primary $\delta^{18}O$ values of +7.5 ‰ to $\delta^{18}O$ values as low as -6 ‰ for feldspar. This wide range indicates that the reservoir rocks have experienced significant variation in the extent of fluid-rock interaction. Minimum W/R ratios calculated from these depletions vary from negligible values to as high as 2.4 for the most $^{18}O/^{16}O$ depleted samples. The $\delta^{18}O$ measurements identify a limited number of localized intervals of extensive $^{18}O/^{16}O$ depletion within the reservoir host rocks; these intervals have interacted and exchanged isotopically with significant quantities of geothermal fluid (high calculated W/R ratios). These local zones of maximum $^{18}O/^{16}O$ depletion correspond closely with the depths of current production zones (intervals of known high permeability) in the wells. Rocks between these intervals have experienced exchange with much smaller quantities of water (much lower permeability). Therefore, the extent of $^{18}O/^{16}O$ depletion serves as a guide to the extent of fluid-rock interaction and permeability in the reservoir rock both currently and in the

past. This pattern of limited, discrete intervals of much greater $^{18}O/^{16}O$ depletion likely reflects that permeability in the rock reservoir is fracture-controlled.

Comparison of the measured $\delta^{18}O$ values of feldspars and reservoir fluid indicate that at preproduction temperatures, feldspars from most of the sampled intervals have $\delta^{18}O$ values too high to be in oxygen isotope exchange equilibrium with the current reservoir fluid; they are incompletely exchanged. The analyses also show that in general, the lower the $\delta^{18}O$ value of the feldspar (the greater the extent of fluid-rock interaction experienced), the closer the feldspar approaches exchange equilibrium with the geothermal fluid (e.g., measured $\Delta_{fsp\text{-}w}$ approaches equilibrium $\Delta_{fsp\text{-}w}$). This positive correlation suggests that increases in permeability of the reservoir host rock increase surface area of host rock exposed to geothermal fluid, thereby increasing the extent of fluid-rock interaction and accompanying oxygen isotopic exchange.

The three feldspar samples with the lowest $\delta^{18}O$ values are all from current production zones in the reservoir. These feldspars are highly depleted in $^{18}O/^{16}O$ and therefore have experienced extensive fluid-rock interaction and isotopic exchange. However, two of these feldspar separates have measured $\Delta_{fsp\text{-}w}$ < equilibrium $\Delta_{fsp\text{-}w}$ which requires that they have equilibrated either at higher temperature with the current reservoir fluid, or with a lower $\delta^{18}O$ reservoir fluid. These discrepancies suggest that the West Flank of the Coso geothermal system was hotter and/or characterized by higher permeability (higher W/R ratio) during fluid-rock exchange in the past.

## 1.6 References

Adams, M.C., Moore, J.N., Bjornstad, S., and Norman, D.I., (2000) Geologic History of the Coso Geothermal System: Transactions, Geothermal Resources Council, v. 24, p. 205-209

Bartley, J.M., Glaner, A.F., Coleman, D.S., Kylander-Clark, A., Mapes, R., and Friedrich, A.M. (2007) Large Laramide dextral offset across Owens Valley, California, and its possible relation to tectonic unroofing of the southern Sierra Nevada: The Geological Society of America Special Paper, v. 434, p. 129-148

Baumgartner, L.P., and Rumble, D., III, (1988) Transport of stable isotopes-I. development of continuum theory for stable isotope transport: Contributions to Mineralogy and Petrology, v. 98, p. 417-430

Baumgartner, L.P., and Valley, J.W. (2001) Stable isotope transport and contact metamorphic fluid flow in Stable Isotope Geochemistry, J.W. Valley and D.R. Cole (eds): Reviews in Mineralogy and Geochemistry, v. 43, p. 41-461

Bowman, J.R., and Willett, S.D. (1991) Spatial patterns of oxygen isotope exchange during one-dimensional fluid infiltration: Geophysical Research Letters, v. 18, p. 971-974

Bowman, J.R., Willett S.D., and Cook, S.J. (1994) Oxygen isotopic transport and exchange during fluid flow: one-dimensional models and applications: American Journal of Science, v. 294, p. 1-55

Browne, P. (1978) Hydrothermal alteration in active geothermal fields: A geochemical review: Annual Reviews in Earth and Planetary Science, v. 6, p. 229-250

Browne, P. (1984), Lectures on geothermal geology and petrology: UNU Geothermal Training Programme, Iceland, Report 1984-2

Cole, D.R., Ohmoto, H., and Jacobs, G.K. (1992) Isotopic exchange in mineral-fluid systems: III. Rates and mechansims of oxygen isotope exchange in the system granite-$H_2O$ ± NaCl ± KCl at hydrothermal conditions: Geochimica et Cosmochimica Acta, v. 56, p. 445-466

Cole, D.R., and Chakraborty, S. (2001) Rates and mechanisms of isotopic exchange in Stable Isotope Geochemistry, J.W. Valley and D.R. Cole (eds): Reviews in Mineralogy and Geochemistry, v. 43, 83-223

Criss, R.E., and Taylor, H.P. Jr. (1983) An $^{18}O/^{16}O$ and D/H study of Tertiary hydrothermal system in the southern half of the Idaho batholith: GSA Bulletin, v. 94, p. 640-663

Criss, R.E., and Taylor, H.P. Jr. (1986) Meteoric-hydrothermal systems" in Stable Isotopes in High Temperature Geological Processes, J.W. Valley, H.P. Taylor, Jr. and J.R. O'Neil (eds): Reviews in Mineralogy v. 16, p. 373-422

Duffield, W.A., Bacon, C.R., and Dalrymple, G.B. (1980) Late Cenozoic volcanism, geochronology, and structure of the Coso Range, Inyo County, California: Journal of Geophysical Research, v. 85, p. 2381-2404

Garlick, G.D., and Epstein, S. (1967) Oxygen isotope ratios in coexisting minerals of regionally metamorphosed rocks: Geochimica et Cosmochimica Acta, v. 31, p. 181-214

Henley, R.W., and Ellis, A.J. (1983) Geothermal systems ancient and modern: a geochemical review: Earth Science Reviews, v. 19, p. 1-50

Hulen, J.B., 1978, Geology and alteration of the Coso Geothermal Area, Inyo County, California: University of Utah Research Institute Report DOE/ID/28392-4, p. 1-28

Kaven, J.O., Hickman, S.H., and Davatzes, N.C. (2012) Using micro-seismicity and seismic velocities to map subsurface geologic and hydrologic structure within the Coso geothermal field, California: Proceedings, 37th Workshop on Geothermal Reservoir Engineering

Kovac, K.M., Moore, J.N., and Lutz, S.J. (2005) Geologic framework of the East Flank, Coso Geothermal Field: implications for EGS development: Proceedings, 30th Workshop on Geothermal Reservoir Engineering

Kurliovitch, L., Norman, D., Heizler, M., Moore, J., and McCulloch, J. (2003) $^{40}Ar/^{39}Ar$ thermal history of the Coso Geothermal Field: Proceedings, 28th Workshop on Geothermal Reservoir Engineering, Stanford, CA, p. 110-116

Lackey, J.S., Valley, J.W., Chen, J.H., and Stockli, D.F. (2008) Dynamic magma systems, crustal recycling, and alteration in the central Sierra Nevada Batholith: the oxygen isotope record: Journal of Petrology, v. 49, p. 1397-1426

Lutz, S.J., and Moore, J.N. (1997). Petrographic and X-ray diffraction study of 130 cuttings samples from six wells in the Coso geothermal area, California, unpublished CalEnergy Corporation Report

Lutz, S.J., Moore J.N., Adams, M.C., and Norman, D.I. (1999) Tracing fluid sources in the Coso Geothermal System using fluid-inclusion gas chemistry: Proceedings, 24th Workshop on Geothermal Reservoir Engineering

Manley, C.R., and Bacon, C.R. (2000) Rhyolite thermobarometry and the shallowing of the magma reservoir, Coso Volcanic Field, California: Journal of Petrology v. 41, p. 149-174

Masi, U., O'Neil, J.R., and Kistler, R.W. (1981) Stable isotope systematics in Mesozoic granites of central and northern California and southwestern Oregon: Contributions to Mineralogy and Petrology, v. 76, p. 116-126

Monastero, F.C., Katzenstien, A.M., Miller, J.S., Unruh, J.R., Adams, M.C., and Richards-Dinger, K. (2005) The Coso geothermal field: a nascent metamorphic core complex: Geologic Society of America Bulletin v. 117, p. 1534-1553

Moore, J.N., Adams, M.C., Bishop-Gollan, B., Copp, J.F., and Hirtz, P. (1990) Geochemical structure of the Coso geothermal system, California: American Association of Petroleum Geologists Guidebook, Coso Field Trip, AAPG EMD #1, Moore J.L. and Erskine, M., eds., p.25-39

O'Neil, J.R., and Taylor, H.P. Jr. (1967) The oxygen isotope and cation exchange chemistry of feldspars: The American Mineralogist, v. 52**,** p. 1414-1437

Patrier, P., Papapanagiotou, P., Beaufort, D., Traineau, H., Bril, H., and Rojas, J., (1996). Role of permeability versus temperature in the distribution of the fine (<0.2 μm) clay fraction in the Chipilapa geothermal system (El Salvador): Journal of Volcanology and Geothermal Research, v. 72, p. 101–120

Reasenberg, P., Ellsworth, W., and Walter, A. (1980) Teleseismic evidence for a low-velocity body under the Coso Geothermal Field: Journal of Geophysical Research, v. 85, p. 2471-2483

Reyes, A. G. (1990) Petrology of Philippines geothermal systems and the application of alteration mineralogy to their assessment: Journal of Volcanology and Geothermal Resources, v. 43, p. 279-309

Spicuzza, M.J., Valley, J.W., and McConnell, V.S. (1998) Oxygen isotope analysis of whole rock via laser fluorination: an air-lock approach: GSA Abstracts with Programs

Steiner, A. (1986) Clay minerals in hydrothermally altered rocks in Wairakei, New Zealand. Clays: Clay Mineralogy, v. 16, p. 193-213

Taylor, H.P., Jr. (1971) Oxygen isotope evidence for large-scale interaction between meteoric ground waters and Tertiary granodiorite intrusion, western Cascade Range, Oregon: Journal of Geophysical Research, v. 76, p. 7855-7874

Taylor, H. P., Jr., and Forester, R.W. (1979) An oxygen and hydrogen isotope study of the Skaergaard intrusion and its country rocks: a description of a 55-M.Y. old fossil hydrothermal system: Journal of Petrology, v. 20, p. 355-419

Truesdell, A.H. (1984) Stable isotopes in hydrothermal systems in Fluid-mineral Equilibria in Hydrothermal Systems, J.M Robertson (ed): Reviews in Economic Geology, v. 1, p. 129-141

Valley, J. W., Kitchen, N., Kohn, M. J., Niendorf, C. R., and Spicuzza, M. J. (1995) UWG-2, A garnet standard for oxygen isotope ratio-Strategies for high precision and accuracy with laser heating: Geochimica et Cosmochimica Acta, v. 59, p. 5223-5231

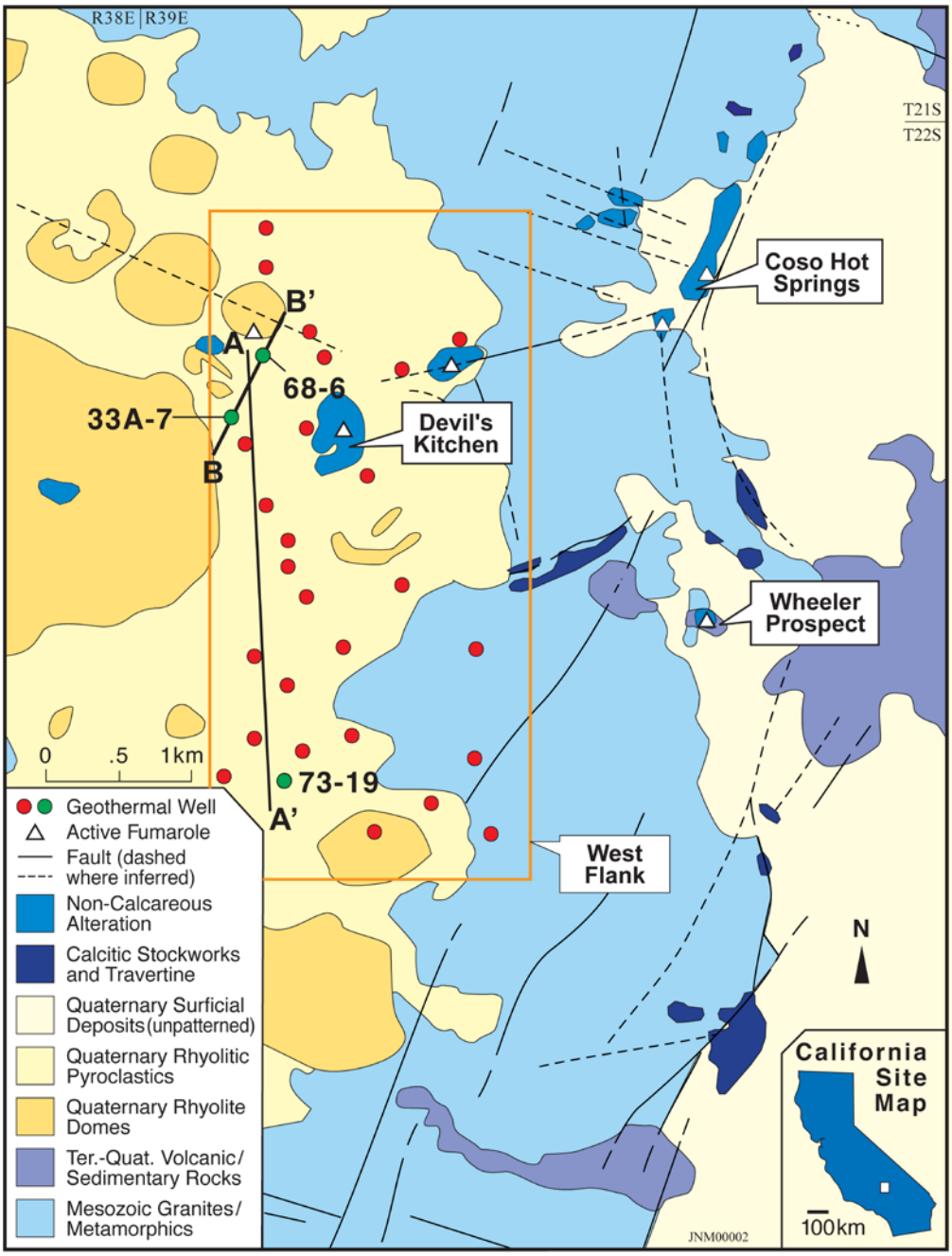


Figure 1.1 A simplified geologic map of the Coso Geothermal system (modified from Hulen, 1978) located on the Naval Air Weapons Station, China Lake, California. The Western Flank of the system is defined by a north-south trending thermal high (Terra-Gen, unpublished data); it is the focus of this study. Well locations in the West Flank are marked by red and green circles; the green circles indicate wells examined in detail for this study while the red circles indicate wells from previous studies. Line A-A' is the transect for a number of cross-sections used in this study. Line B-B' is a transect drawn to show the thermal profile between wells 68-6 and 33A-7.

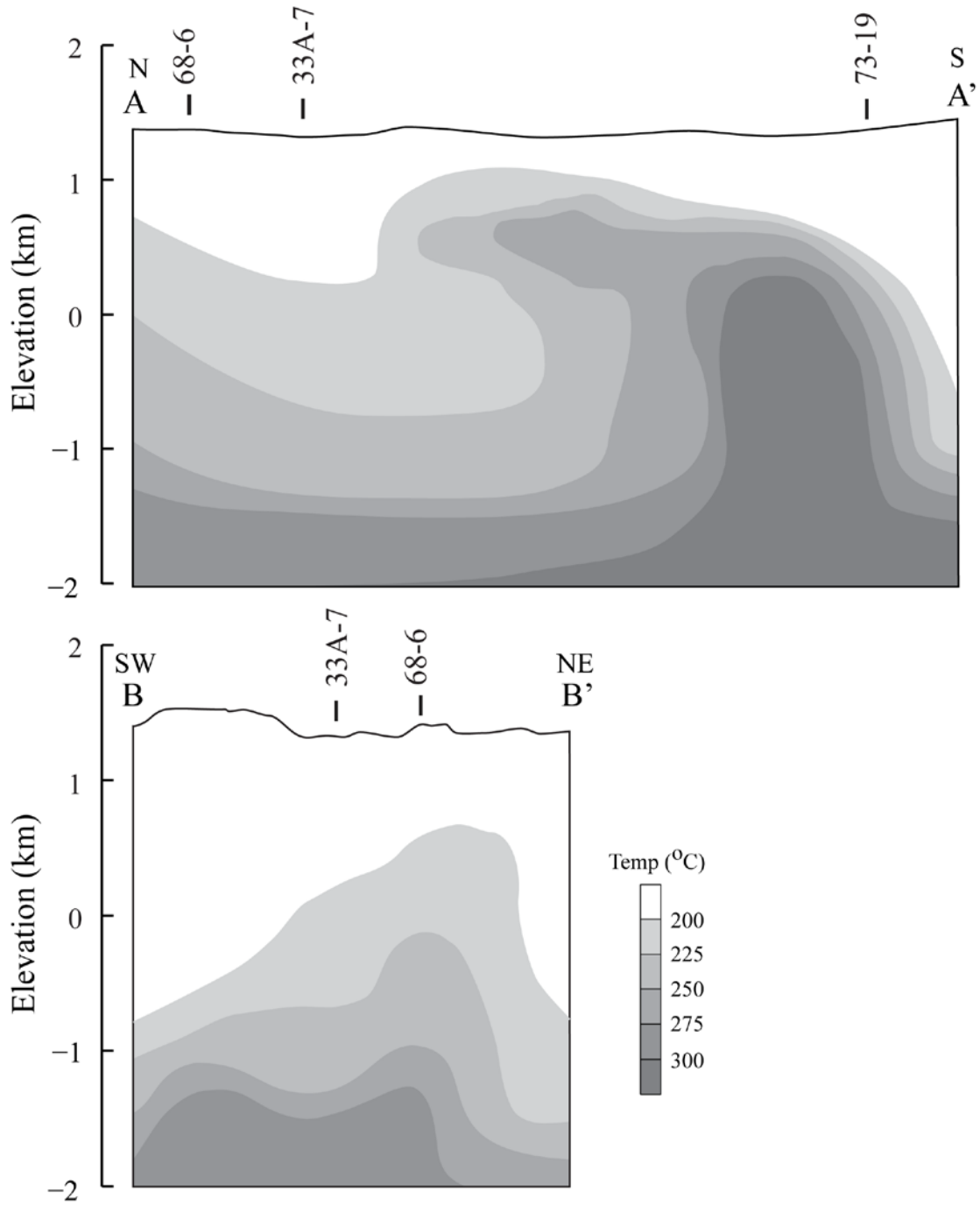


Figure 1.2: General north-south thermal structure of the West Flank along the transects A-A' and B-B'. Temperature values come from down-hole measurements made prior to production.

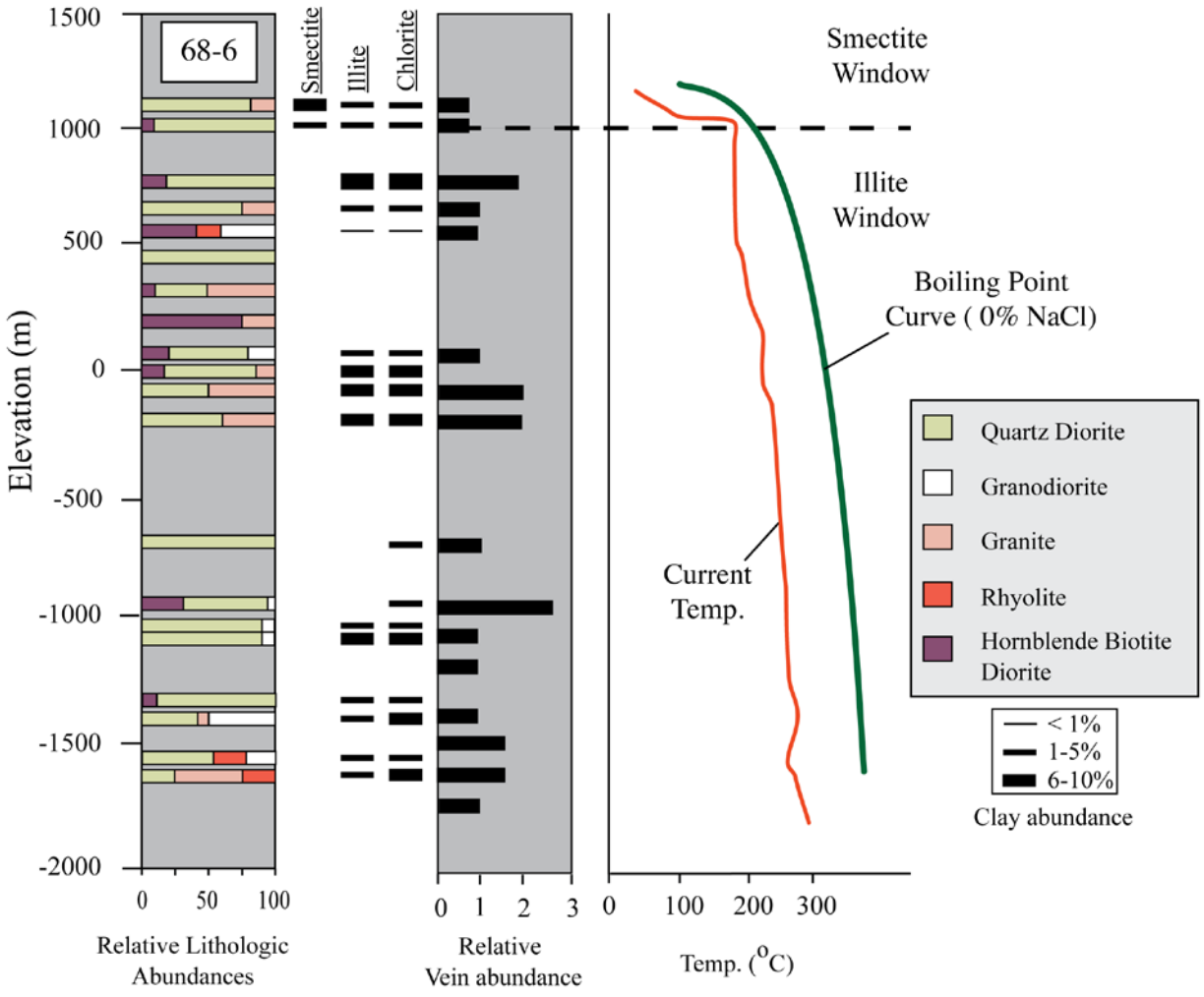


Figure 1.3: Lithologic abundances, clay content, abundance of veining and temperature information for well 68-6. Veining scale is trace (1), minor (2), abundant (3). Smectite and illite windows defined by observed occurrences.

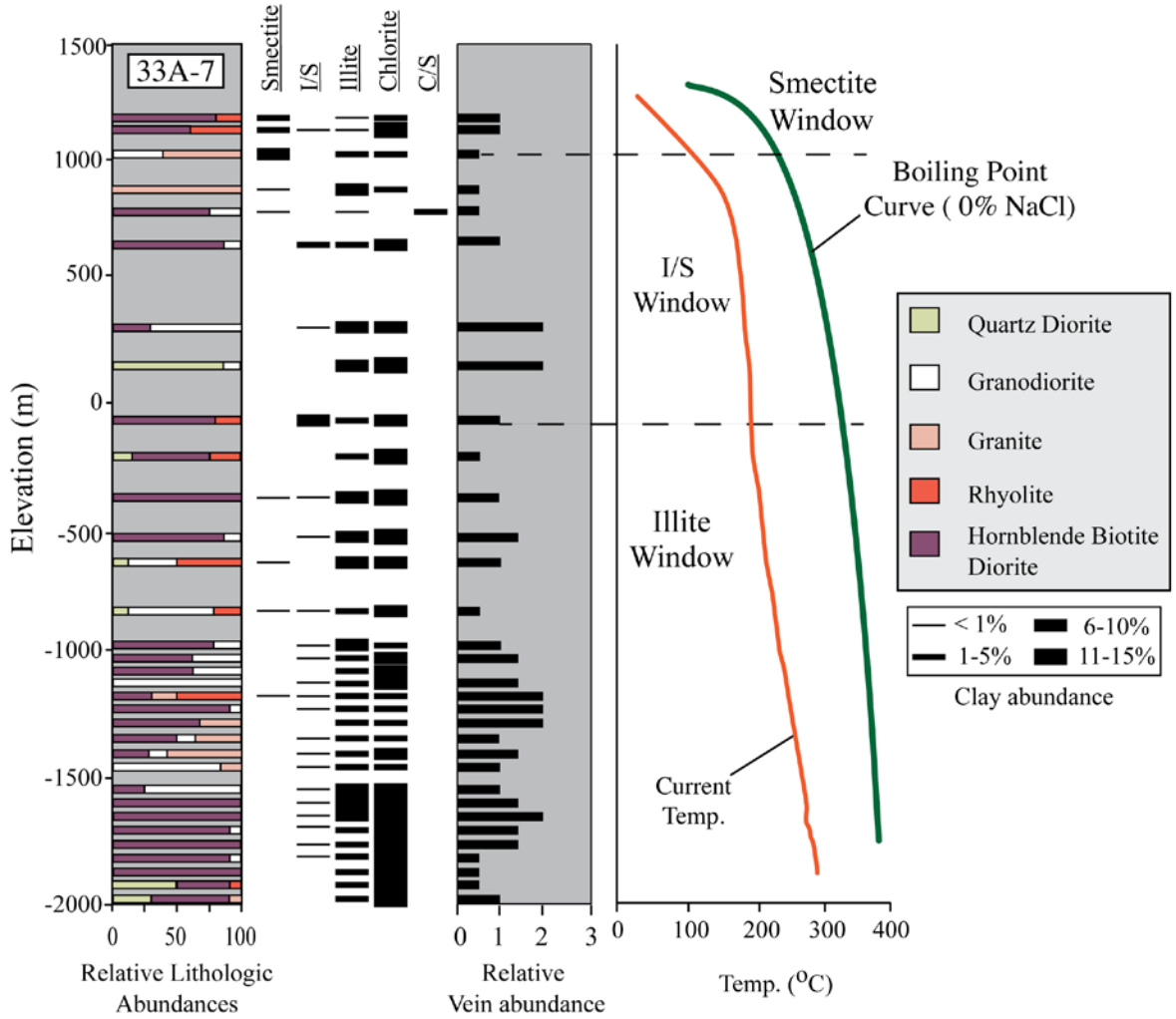


Figure 1.4: Lithologic abundances, clay content, abundance of veining and temperature information for well 33A-7. Veining scale is trace (1), minor (2), abundant (3). Smectite and illite windows defined by observed occurrences.

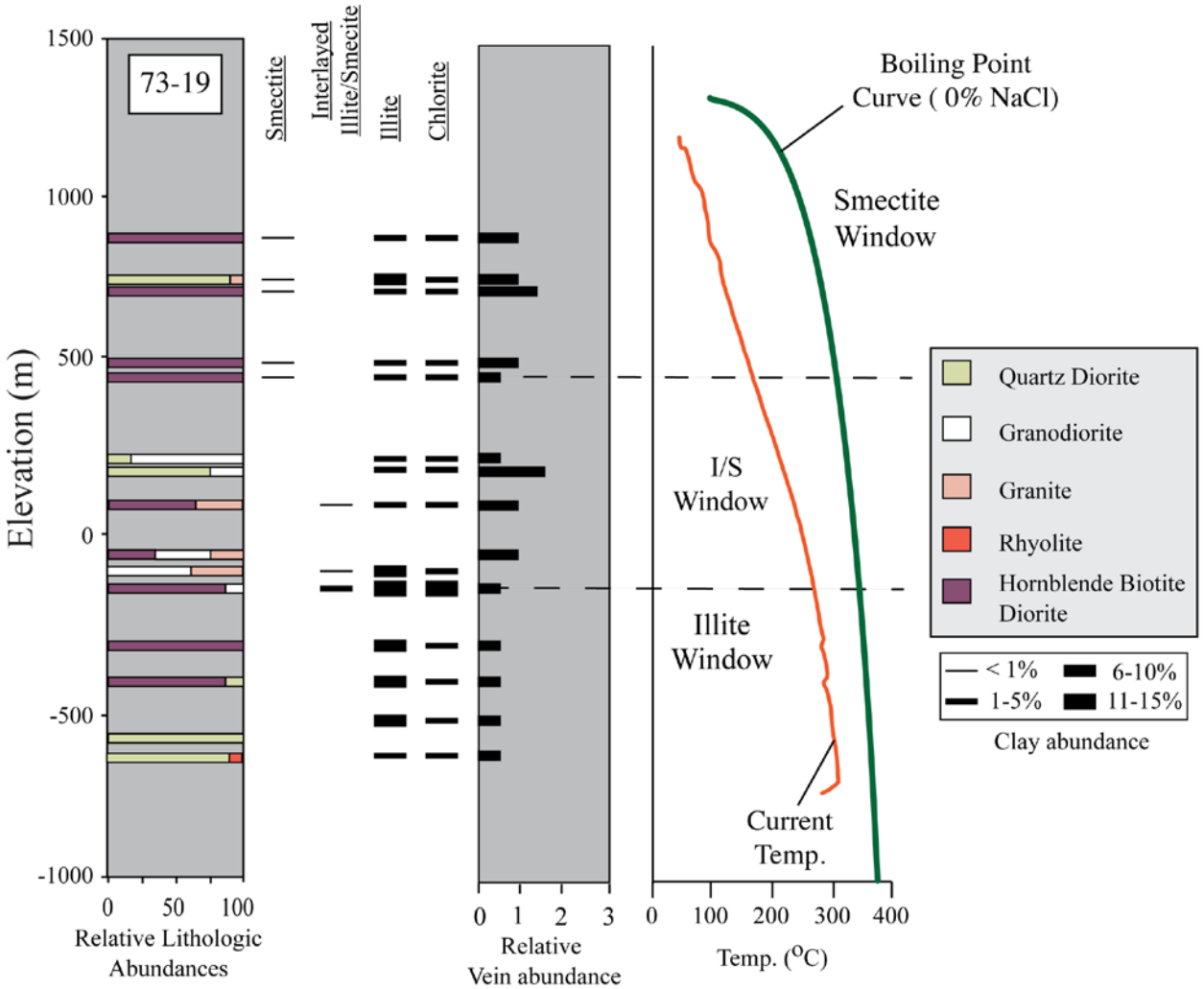


Figure 1.5: Lithologic abundances, clay content, abundance of veining and temperature information for well 73-19. Veining scale is trace (1), minor (2), abundant (3). Smectite and illite windows defined by observed occurrences.

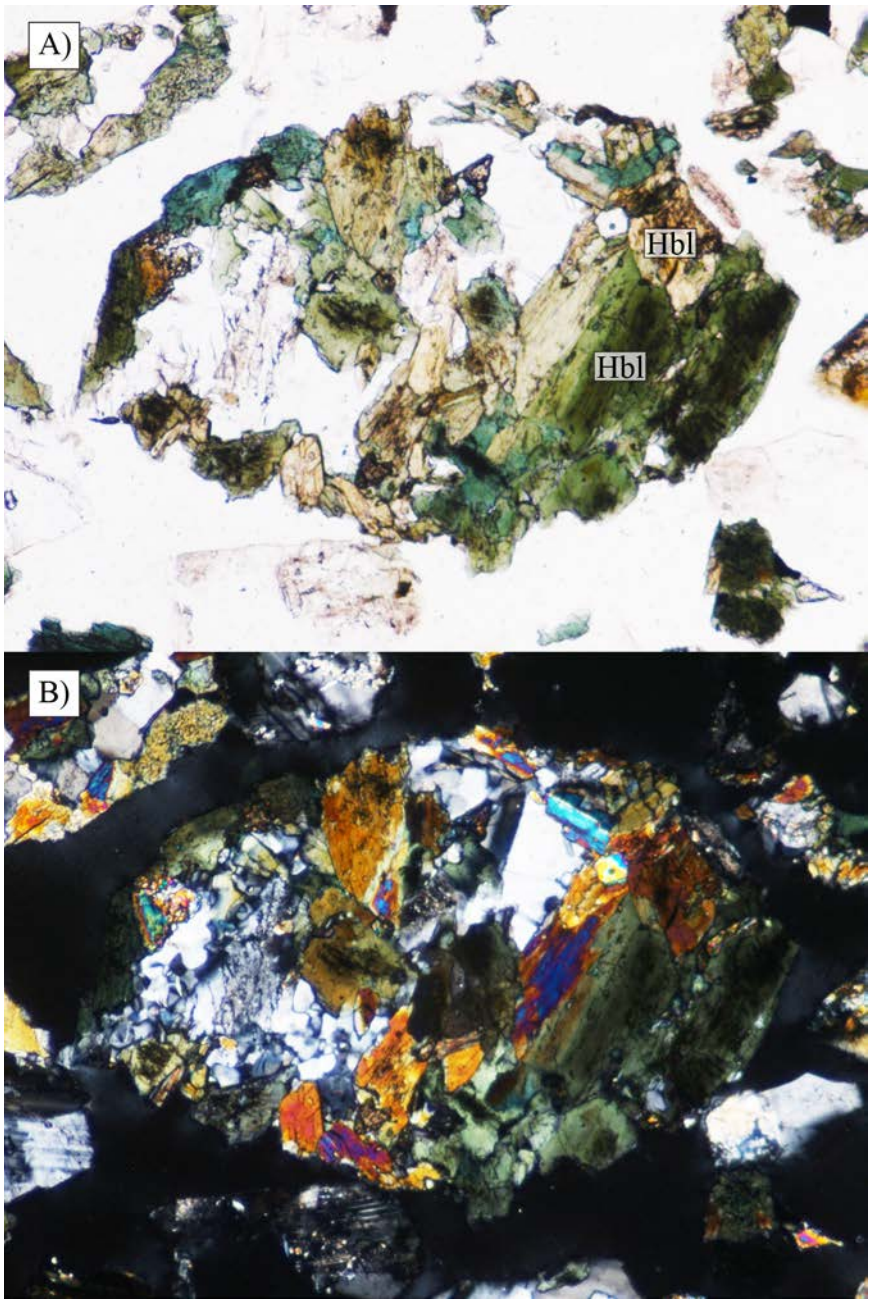


Figure 1.6: A representative photomicrograph of a hornblende rich diorite chip. This sample is from well 33A-7, interval 3112 m. A) taken under plane polarized light. Hornblende (Hbl) is green to light brown. B) taken under crossed polarized light. Field of view is 3.1 mm across.

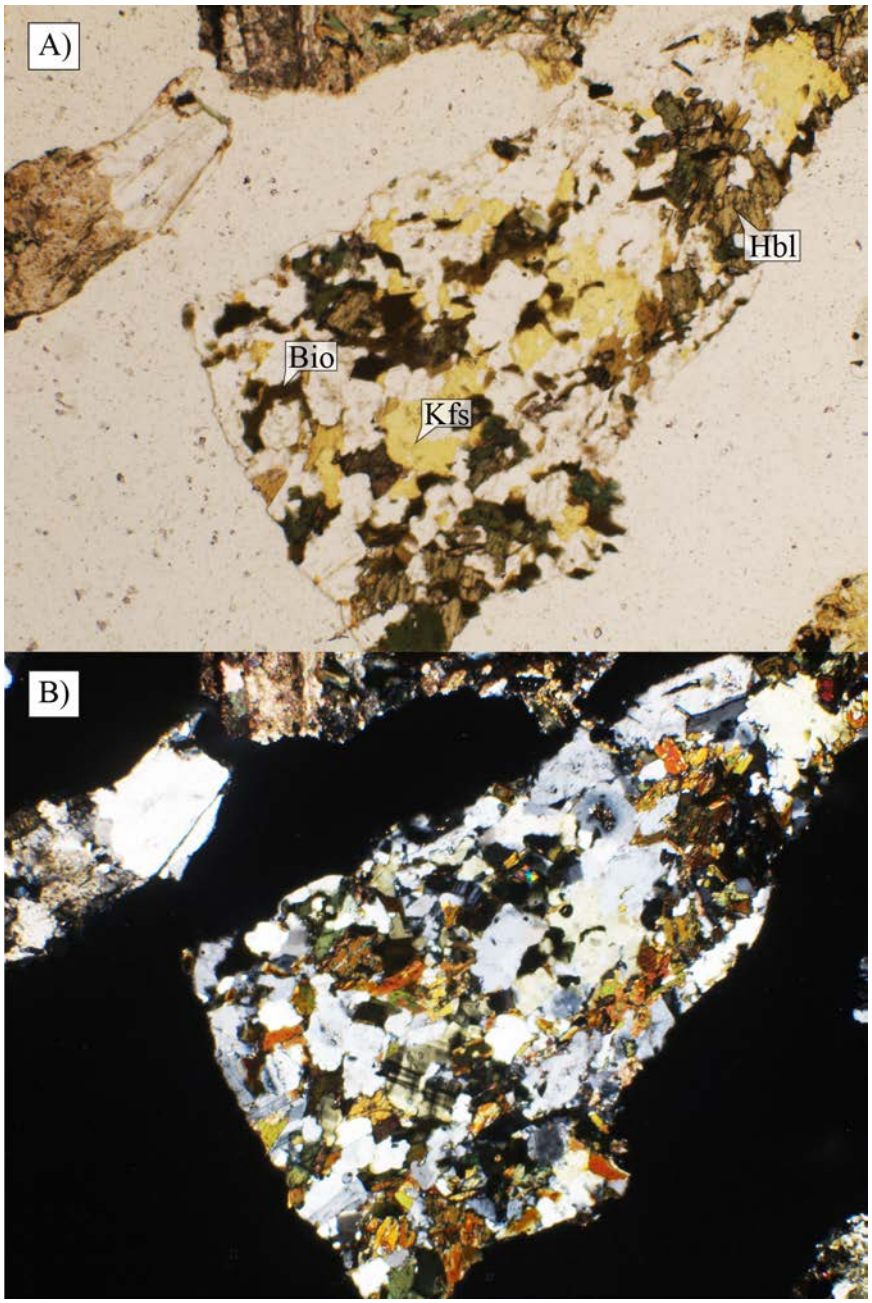


Figure 1.7: A representative photomicrograph of a hornblende-biotite-quartz diorite chip from well 33A-7, interval 2136.6 m. A) taken under plane polarized light. Biotite (Bio) is dark brown and hornblende (Hbl) is dark green to tan with distinct 60-120$^{o}$ cleavage. Potassium feldspar (Kfs) is stained yellow for easier identification. B) taken under crossed polarized light. The field of view is 3.1 mm.

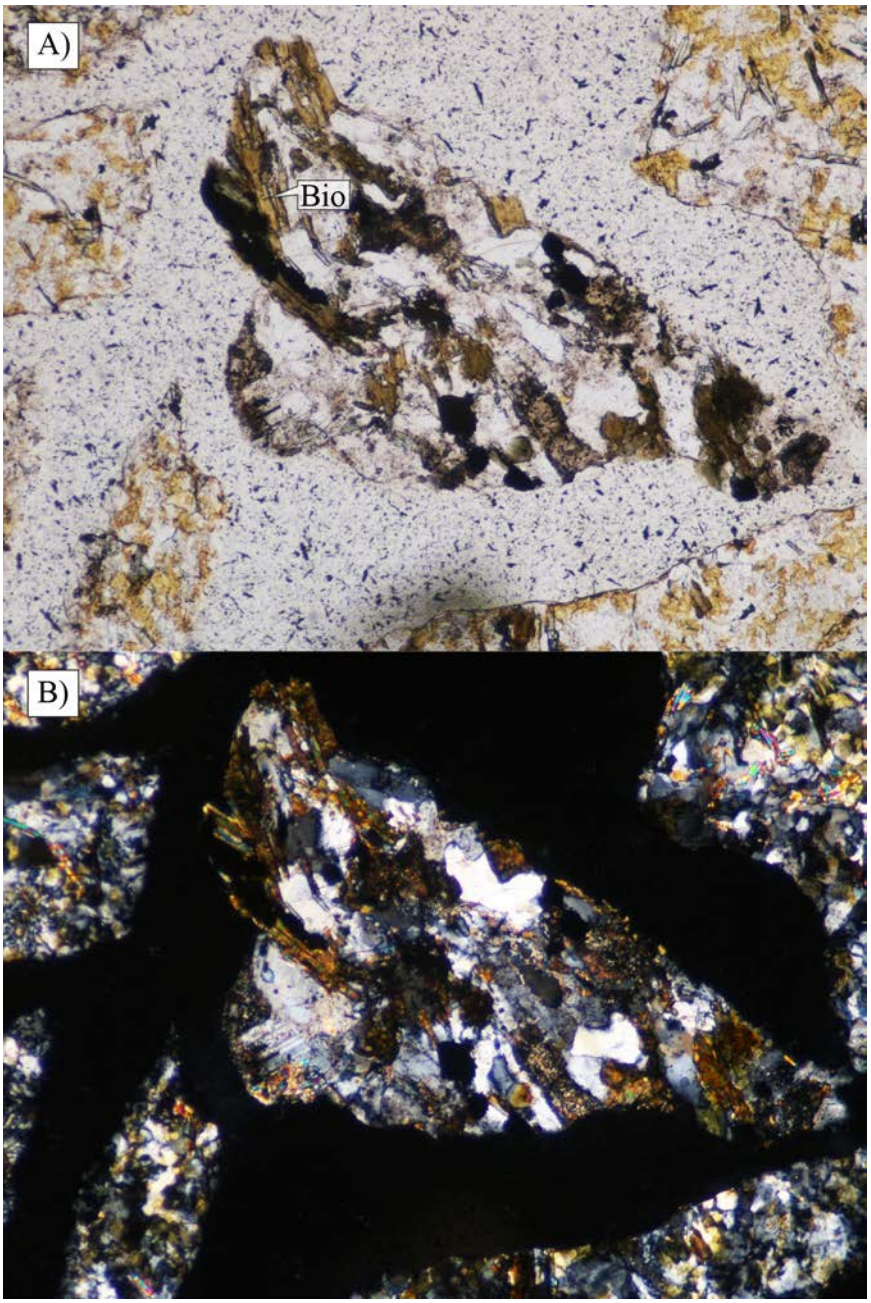


Figure 1.8: A representative photomicrograph of a biotite-quartz diorite chip from well 73-19 interval 1316.7 m. A) taken under plane polarized light. Biotite (Bio) is dark brown; B) taken under crossed polarized light. The field of view is 2.2 mm.

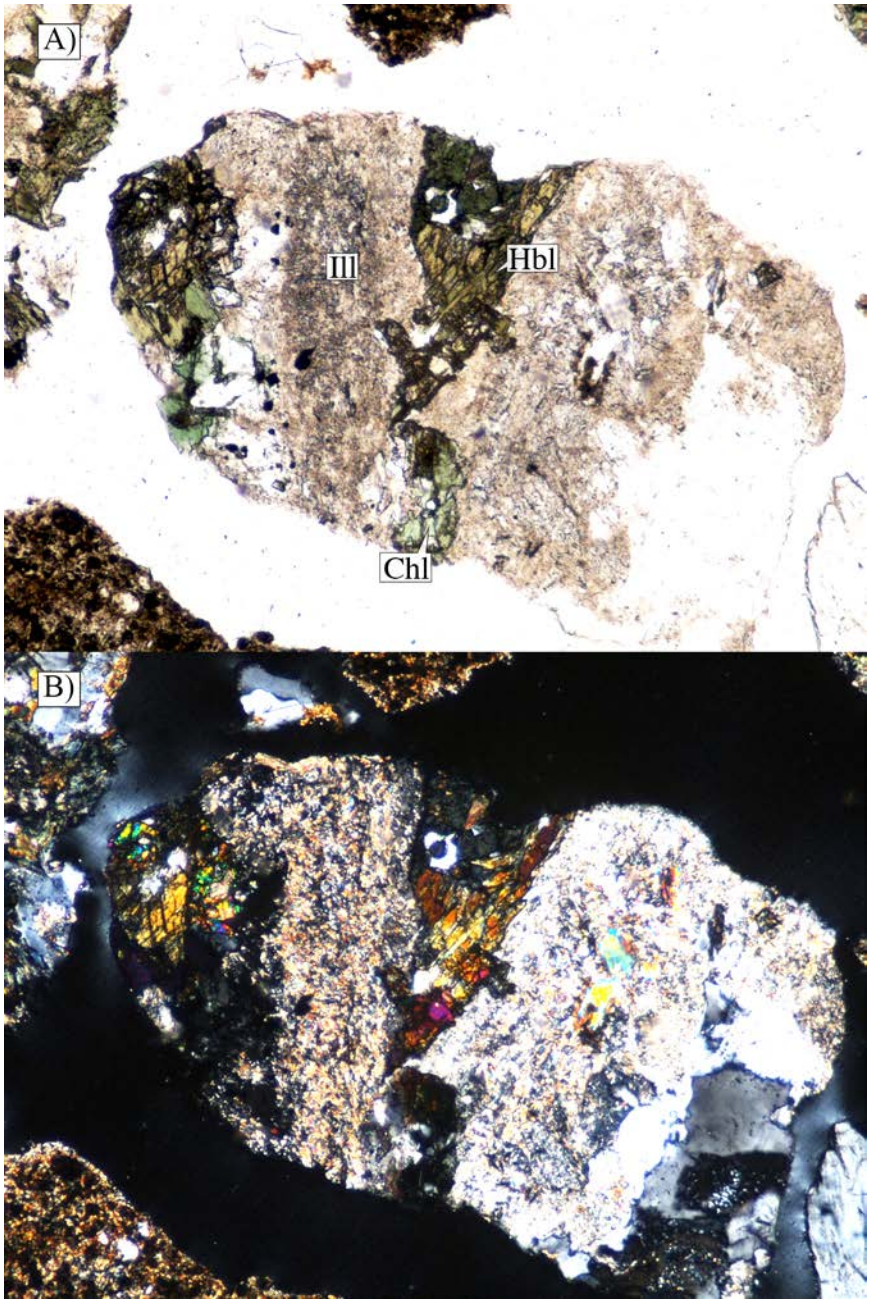


Figure 1.9: A representative photomicrograph of a pervasively altered diorite chip. This sample is from well 33A-7, interval 1569.7 m. A) taken under plane polarized light. Hornblende (Hbl) has partially to completely altered to chlorite (Chl). Feldspars have almost entirely altered to illite (Ill). B) taken under crossed polarized light. Field of view is 3.1 mm across.

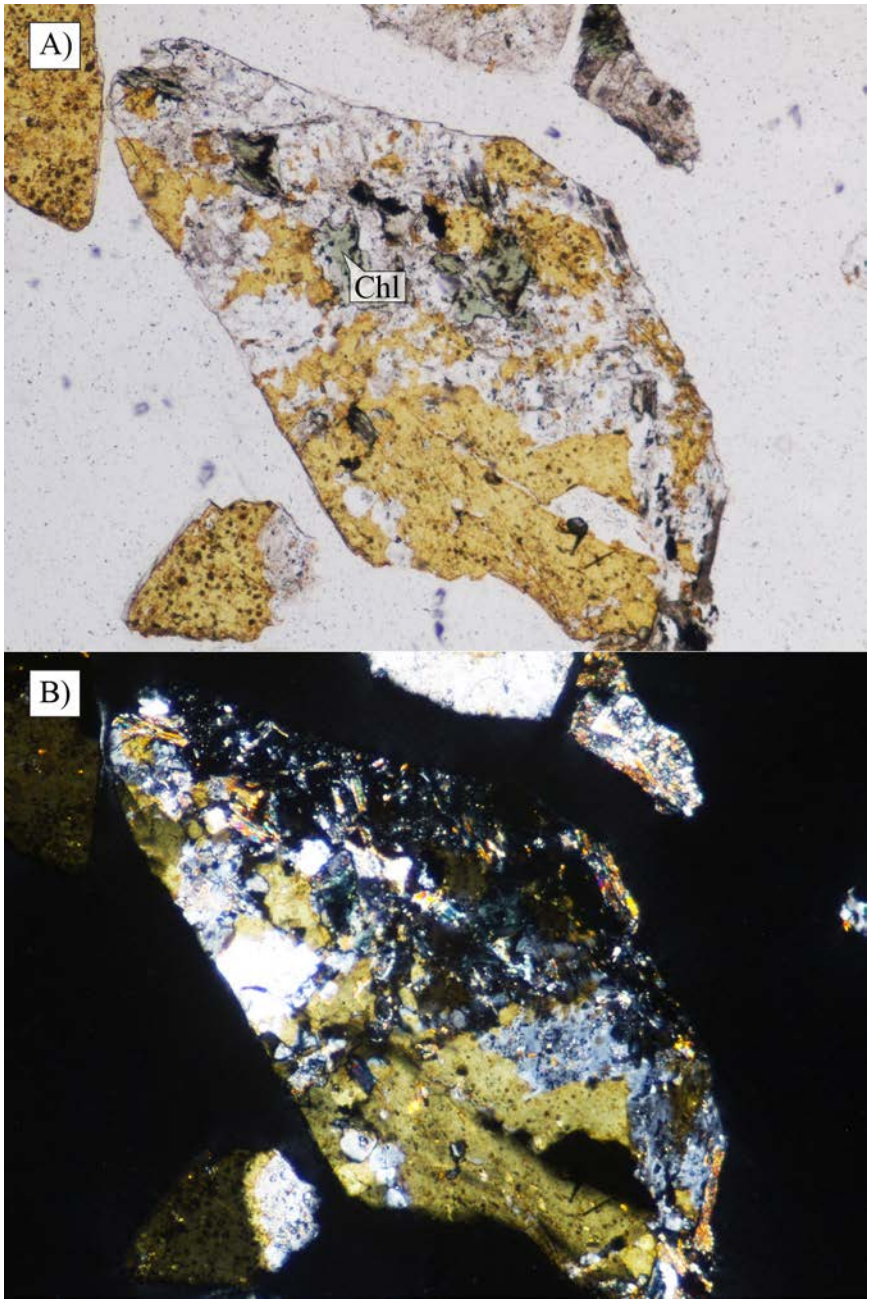


Figure 1.10: A representative photomicrograph of a granodiorite chip. This sample is from well 33A-7, interval 1877.6 m. A) taken under plane polarized light. Potassium feldspar is stained yellow. Ferromagnesian minerals are replaced by chlorite (Chl). B) taken under crossed polarized light. Field of view is 2.2 mm across.

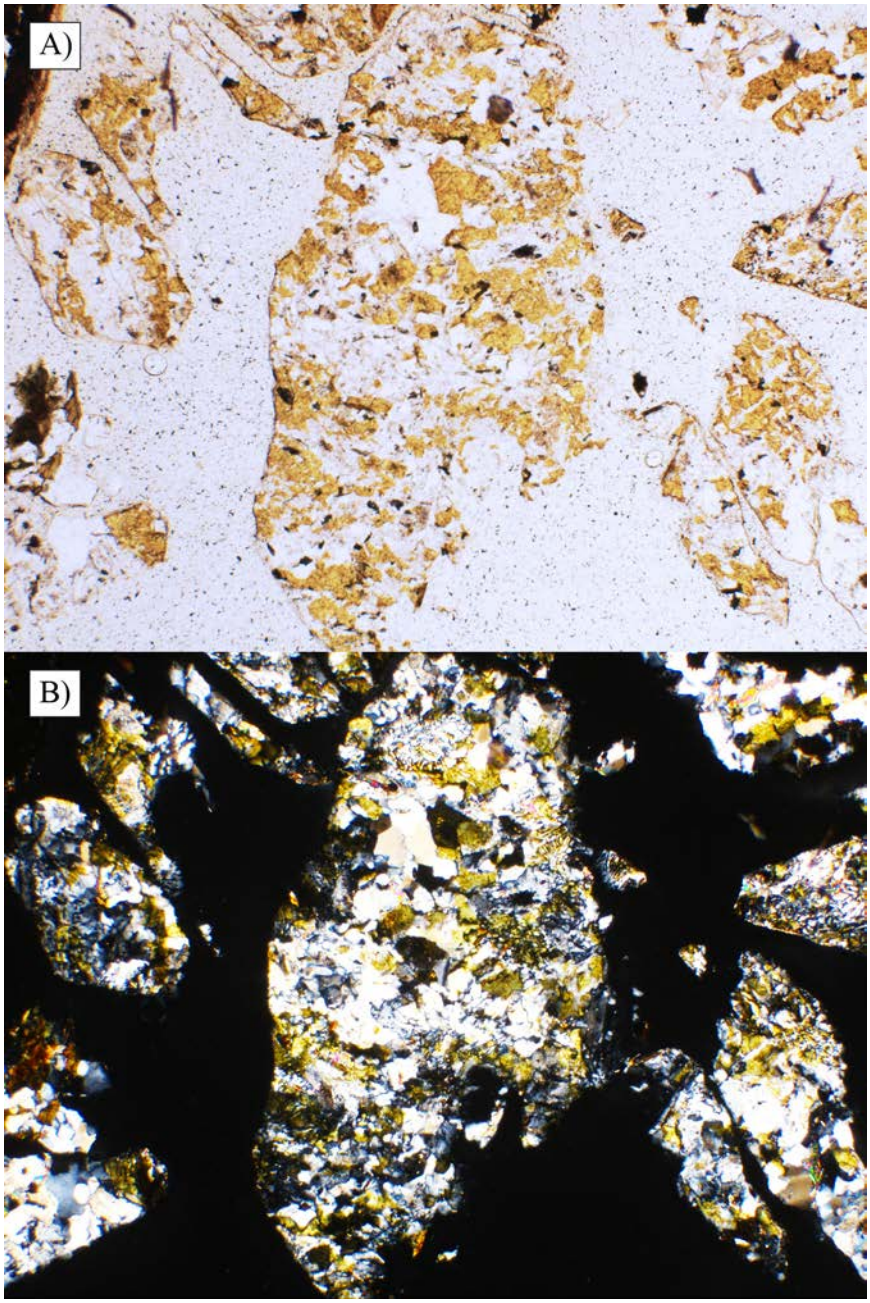


Figure 1.11: Typical granite chips (from well 73-19, interval 1060.7 m) with abundant potassium feldspar (stained yellow). A) plane polarized light; B) crossed polarized light. The field of view is 2.2 mm.

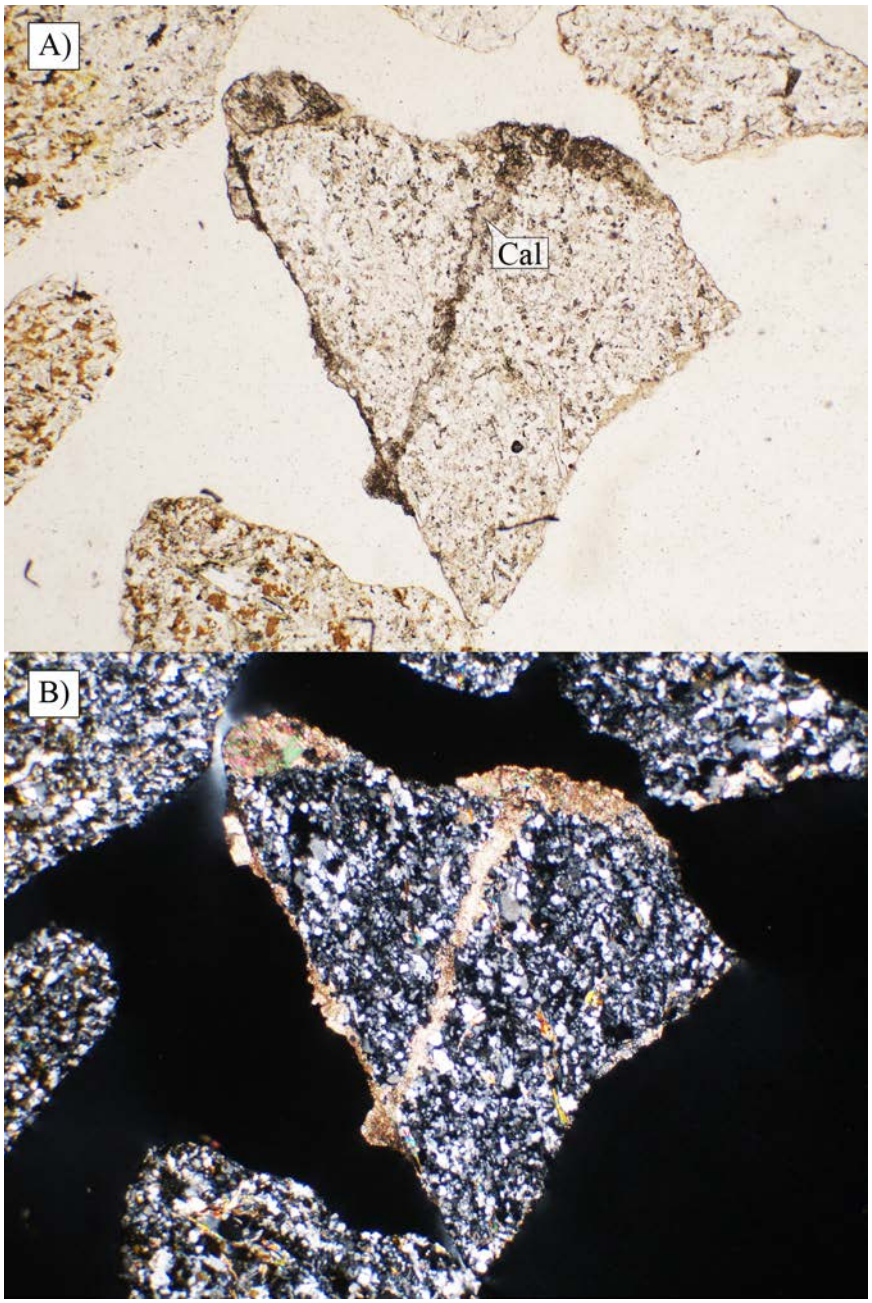


Figure 1.12: A microgranite chip cut by a calcite vein (Cal) found in well 73-19. A) taken under plane polarized light; B) taken under crossed polarized light. The field of view is 3.1 mm.

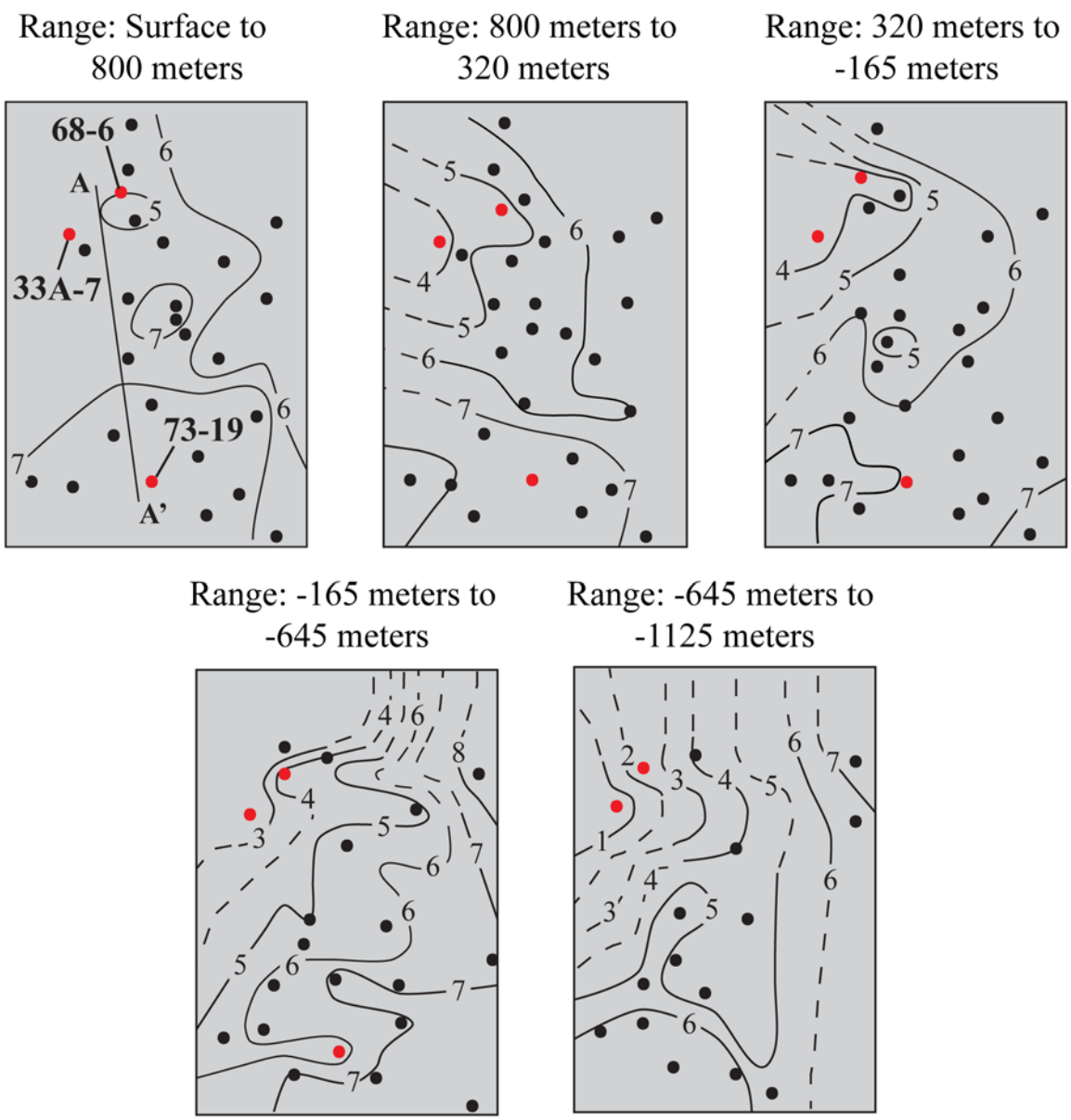


Figure 1.13: Plan maps of the whole-rock oxygen isotope data at a series of elevation intervals in the Coso system. The contour values (in ‰) represent averages of the data over 480 m intervals throughout the field. All elevations are relative to sea level. The red and black dots are well locations; dashed lines are used where contouring has been inferred. The location of transect A-A' in the West Flank is shown in the upper left panel.

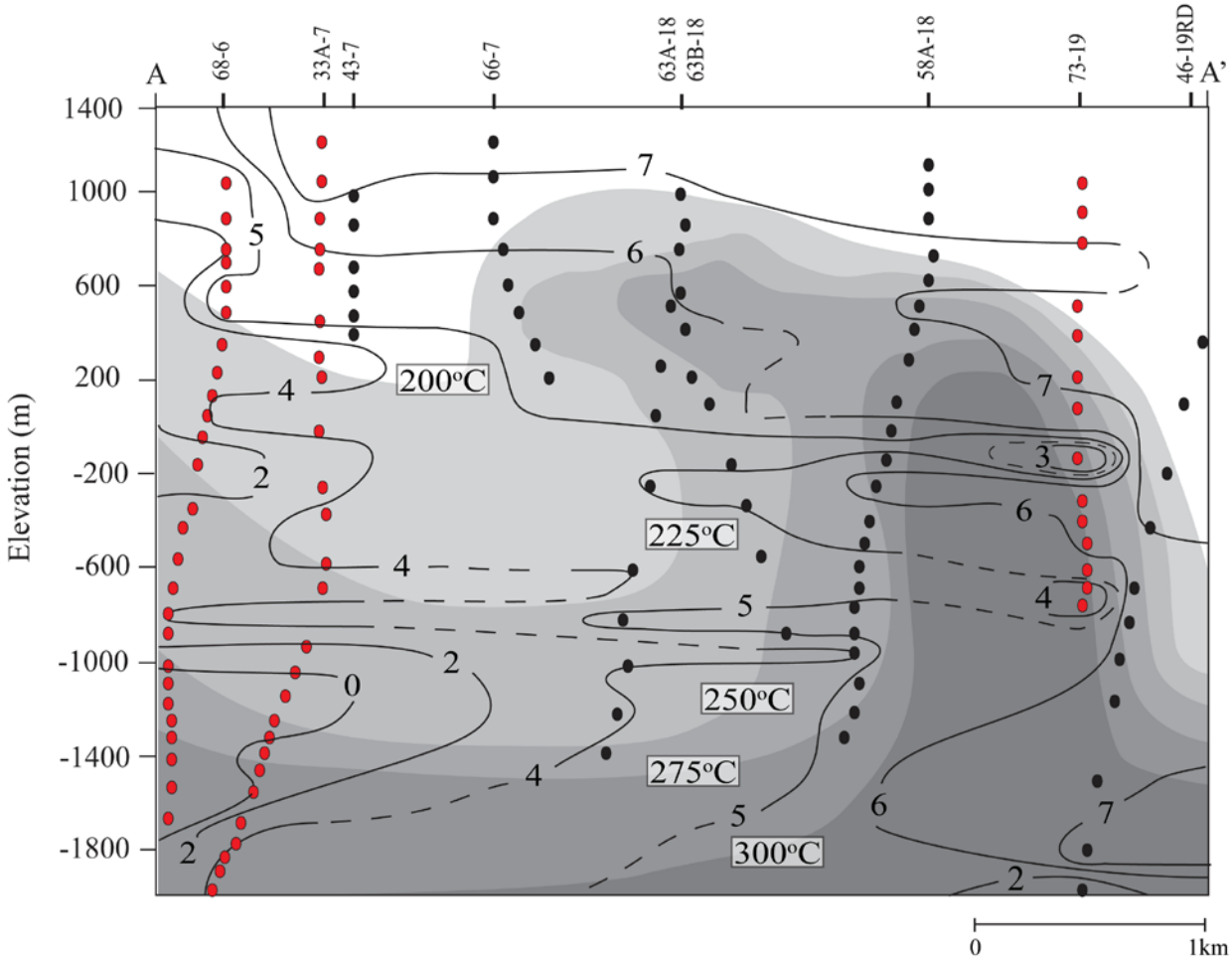


Figure 1.14: Vertical cross-section of the oxygen isotope data along the north-south transect, A-A'. The locations of all wells and data points used are shown; contours of the oxygen isotope data are in ‰. Red circles indicate the locations of samples analyzed in this study. 200, 225, 250, 275 and 300 °C isotherms from Figure 1.2 are included; see text for discussion.

Table 1.1: Measured $\delta^{18}O$ values for whole-rock and feldspar mineral samples from well 68-6, Coso geothermal system, California. Values are reported in per mil (‰) notation, relative to VSMOW.

| | **Well: 68-6** | |
|---|---|---|
| Depth (m) | Whole-Rock (‰) | Feldspar (‰) |
| 271.3 | 3.88 | |
| 335.3 | 4.47 | 6.04 |
| 423.7 | 2.55 | |
| 487.7 | 3.49 | 6.59 |
| 563.9 | 5.08 | |
| 685.8 | 5.78 | |
| 722.4 | 6.02 | 6.29 |
| 883.9 | 3.57 | |
| 984.5 | 4.07 | |
| 1069.8 | 4.30 | |
| 1271.0 | 4.43 | |
| 1371.6 | 2.44 | 5.24 |
| 1432.6 | 2.87 | |
| 1484.4 | 1.50 | 4.96 |
| 1554.5 | 2.60 | |
| 1700.8 | 3.78 | 5.64 |
| 1798.3 | 4.67 | 6.76 |
| 1935.5 | 4.46 | |
| 2066.5 | 2.94 | |
| 2270.8 | 2.70 | |
| 2392.7 | 0.75 | |
| 2465.8 | 0.75 | 3.09 |
| 2566.4 | 0.61 | |
| 2709.7 | 0.75 | 3.08 |
| 2792.0 | 2.83 | 3.59 |
| 2849.9 | 0.54 | |
| 2895.6 | 0.26 | |
| 2941.3 | -4.60 | -3.88 |
| | | -5.06[#] |
| | | -4.12[*] |
| 2984.0 | -1.05 | 1.76 |
| 3173.0 | 0.64 | |

[#]Hand picked cloudy (more altered) feldspar

[*]Feldspar separated from finer-grained (150-200 mesh) whole rock aliquot

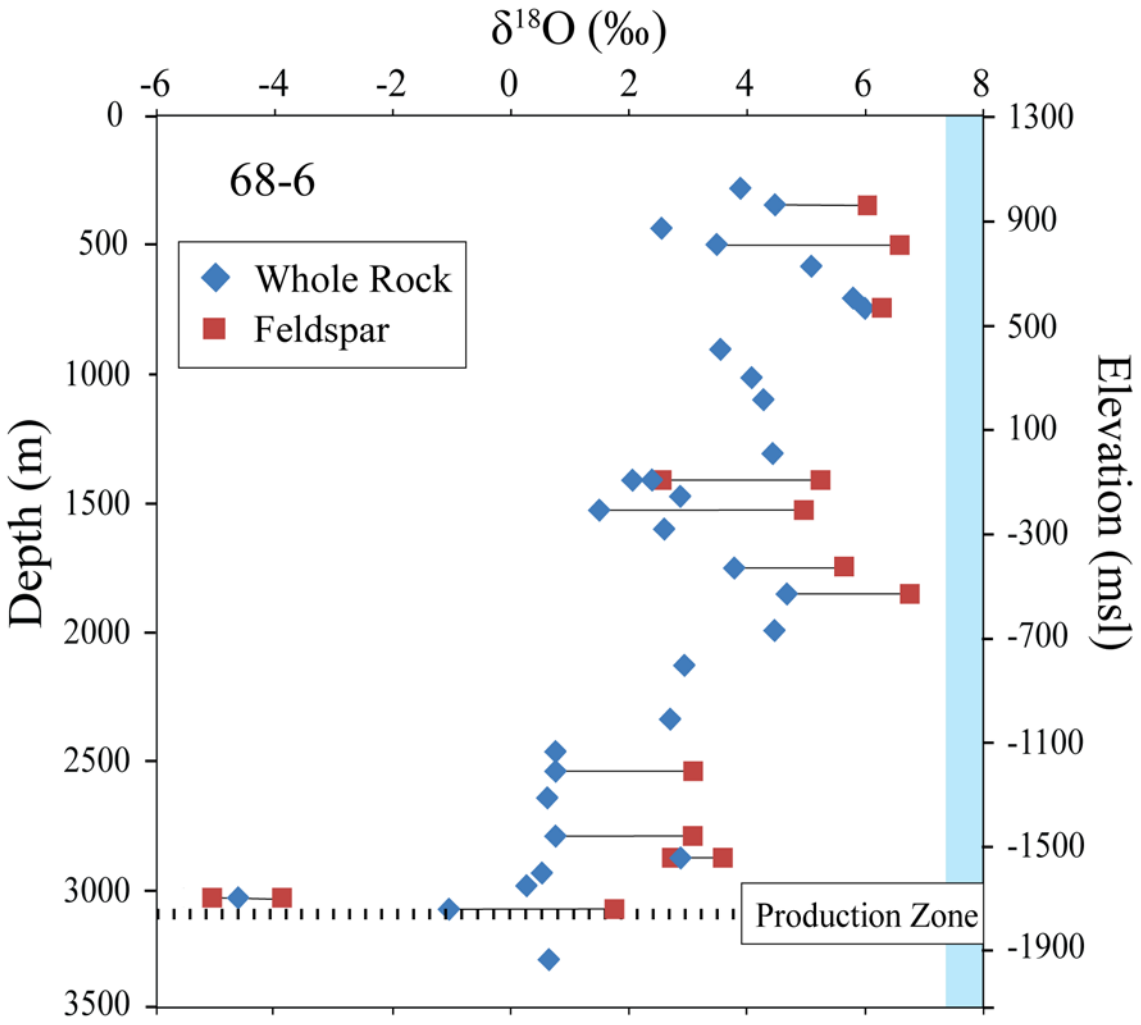


Figure 1.15: Measured $\delta^{18}O$ values of whole-rock and feldspar samples as a function of depth for well 68-6. All values are reported in per mil (relative to VSMOW), and plotted at both well depth and elevation (meters above sea level). The shaded light blue region here and in Figures 1.16 and 1.17 represents the range of primary $\delta^{18}O$ values of diorite to granodiorite rocks from the region that are equivalent to the reservoir host rocks in the Coso system (Masi et al., 1981; Lackey et al., 2008). The dotted line marks the current production zone (interval of lost circulation) in 68-6.

Table 1.2: Measured $\delta^{18}O$ values for whole-rock and feldspar mineral samples from well 33A-7, Coso geothermal system, California. Values are reported in per mil (‰) notation, relative to VSMOW.

| **Well: 33A-7** | | |
|---|---|---|
| Depth (m) | Whole-Rock (‰) | Feldspar (‰) |
| 33.5 | 7.62 | 7.50 |
| 109.7 | 3.7 | |
| 262.1 | 5.39 | |
| 414.5 | 7.45 | |
| 566.9 | 4.84 | |
| 646.2 | 5.34 | |
| 871.7 | 0.2 | |
| 1024.1 | 3.59 | |
| 1100.3 | 3.00 | 5.49 |
| 1325.9 | 4.18 | |
| 1569.7 | 3.89 | |
| 1649.0 | 2.71 | |
| 1877.6 | 1.03 | |
| 1984.2 | 3.93 | |
| 2136.6 | 1.60 | |
| 2212.8 | -0.44 | |
| 2322.6 | -0.02 | |
| 2322.6 | -1.02 | |
| 2350.0 | -0.98 | |
| 2380.5 | 0.14 | |
| 2471.9 | 0.51 | -2.37 |
| 2502.4 | -2.35 | |
| 2529.8 | -3.08 | -0.03 |
| | | +0.63* |
| 2566.4 | 0.94 | 4.16 |
| 2593.8 | 2.15 | 4.20 |
| 2624.3 | 1.55 | |
| 2654.8 | 2.92 | |
| 2685.3 | 2.10 | 4.60 |
| 2746.2 | 3.91 | |
| 2837.7 | 4.48 | 5.49 |
| 2959.6 | 4.60 | |
| 2990.1 | 4.25 | |
| 3020.6 | 4.05 | |
| 3051.0 | 1.78 | |
| 3081.5 | 4.21 | |
| 3112.0 | 4.03 | |
| 3142.5 | 4.61 | |
| 3173.0 | 4.10 | |
| 3233.9 | 4.49 | |
| 3294.9 | 3.88 | 5.90 |

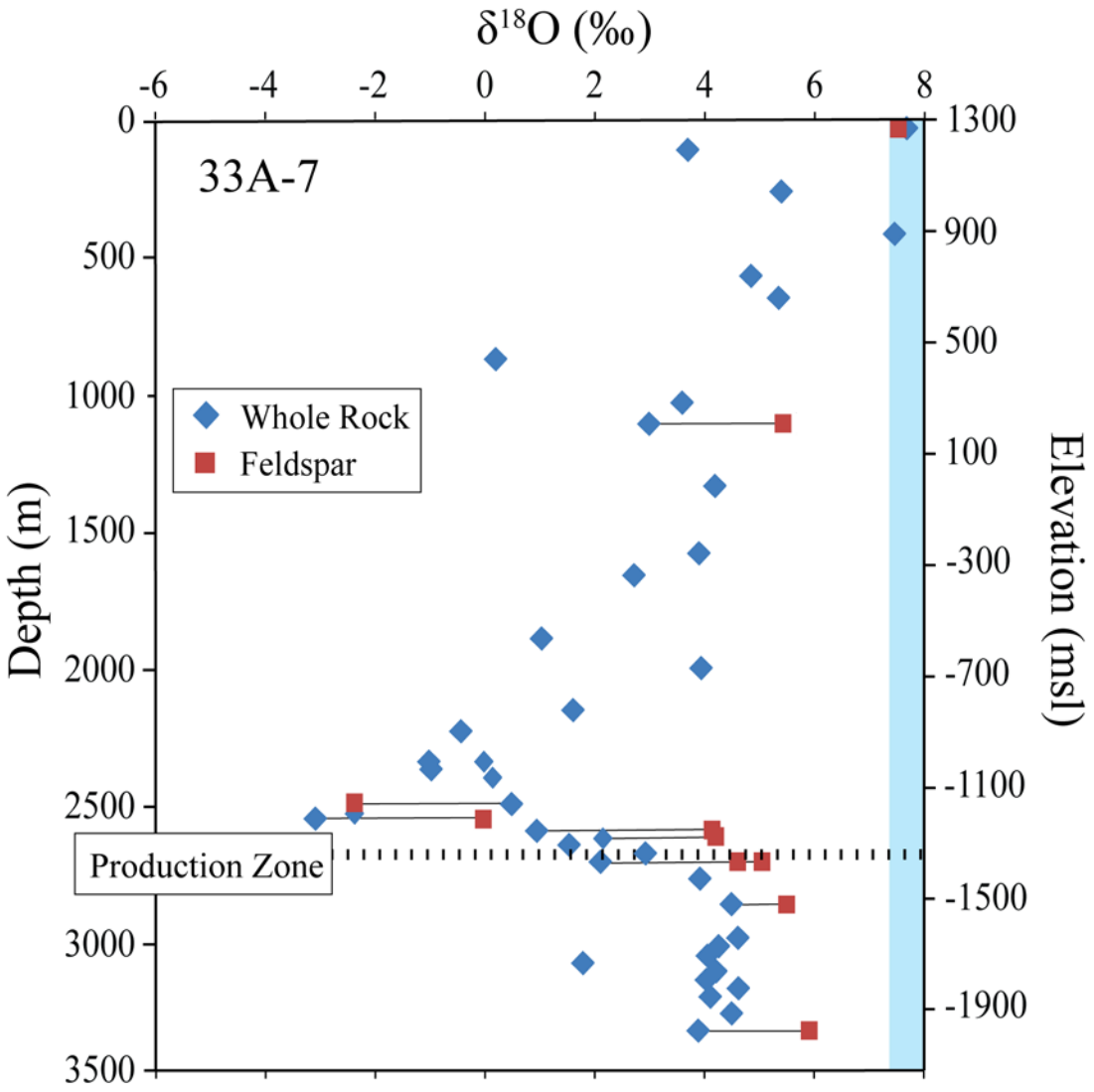


Figure 1.16: Measured $\delta^{18}O$ values (in per mil, relative to VSMOW) of whole-rock and feldspar samples as a function of well depth and elevation for well 33A-7. The dotted line marks the current production zone (interval of lost circulation) in 33A-7.

Table 1.3: Measured $\delta^{18}O$ values for whole-rock and feldspar mineral samples from well 73-19, Coso geothermal system, California. Values are reported in per mil (‰) notation, relative to VSMOW.

| | **Well: 73-19** | |
|---|---|---|
| Depth (m) | Whole-Rock (‰) | Feldspar (‰) |
| 271.3 | 6.98 | 7.79 |
| 381.0 | 6.61 | |
| 390.1 | 6.37 | |
| 445.0 | 7.48 | 8.12 |
| 545.6 | 5.52 | |
| 777.2 | 7.57 | |
| 798.6 | 6.36 | |
| 1060.7 | 7.16 | |
| 1072.9 | 7.41 | |
| 1225.3 | 6.07 | |
| 1316.7 | 6.63 | |
| 1347.2 | 5.91 | |
| 1386.8 | 4.61 | 6.14 |
| 1411.2 | 2.38 | |
| 1481.3 | 6.30 | 7.26 |
| 1581.9 | 5.94 | |
| 1664.2 | 6.85 | |
| 1709.9 | 5.13 | |
| 1813.6 | 5.14 | 6.20 |
| 1834.9 | 3.30 | 6.34 |
| 1856.2 | 3.30 | |

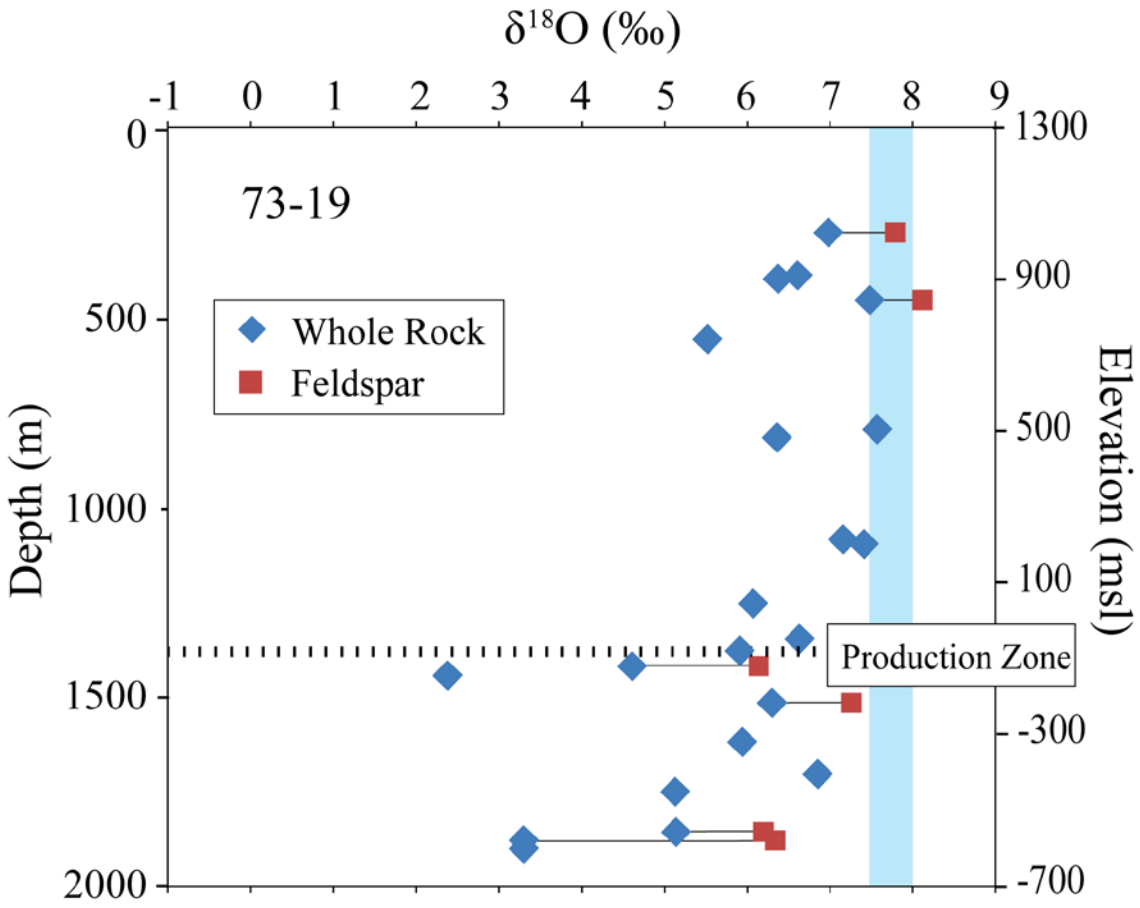


Figure 1.17: Measured $\delta^{18}O$ values (in per mil, relative to VSMOW) of whole-rock and feldspar samples as a function of well depth and elevation for well 73-19. The dotted line marks the current production zone (interval of lost circulation) in 73-19.

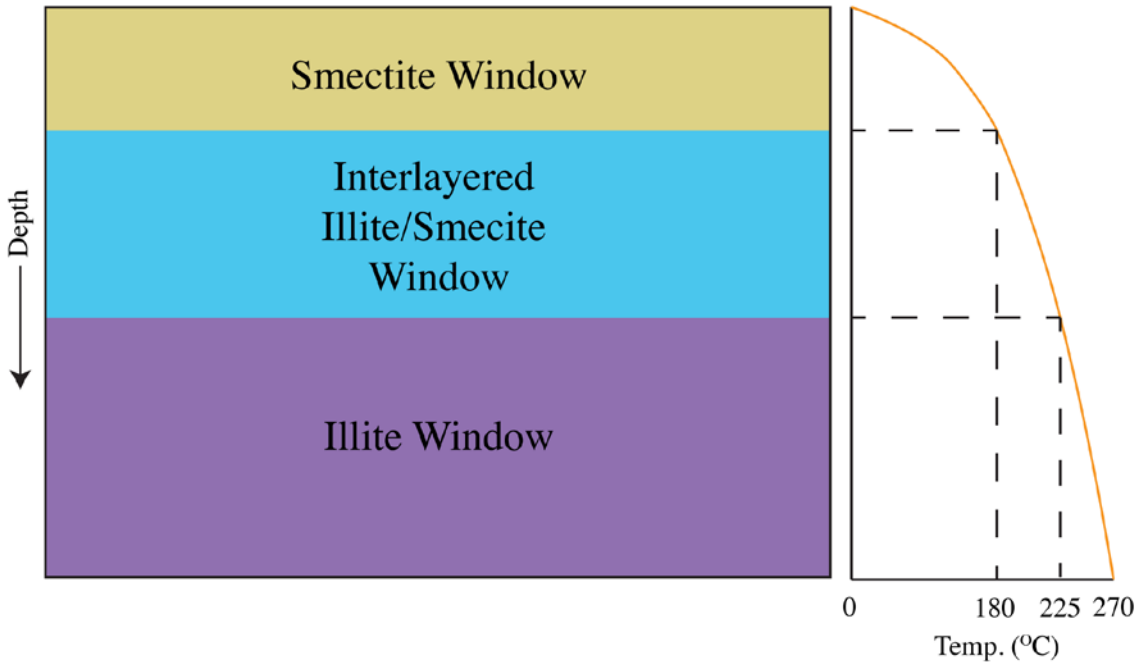


Figure 1.18: Expected clay mineralogy zoning with increasing depth as a function of temperature.

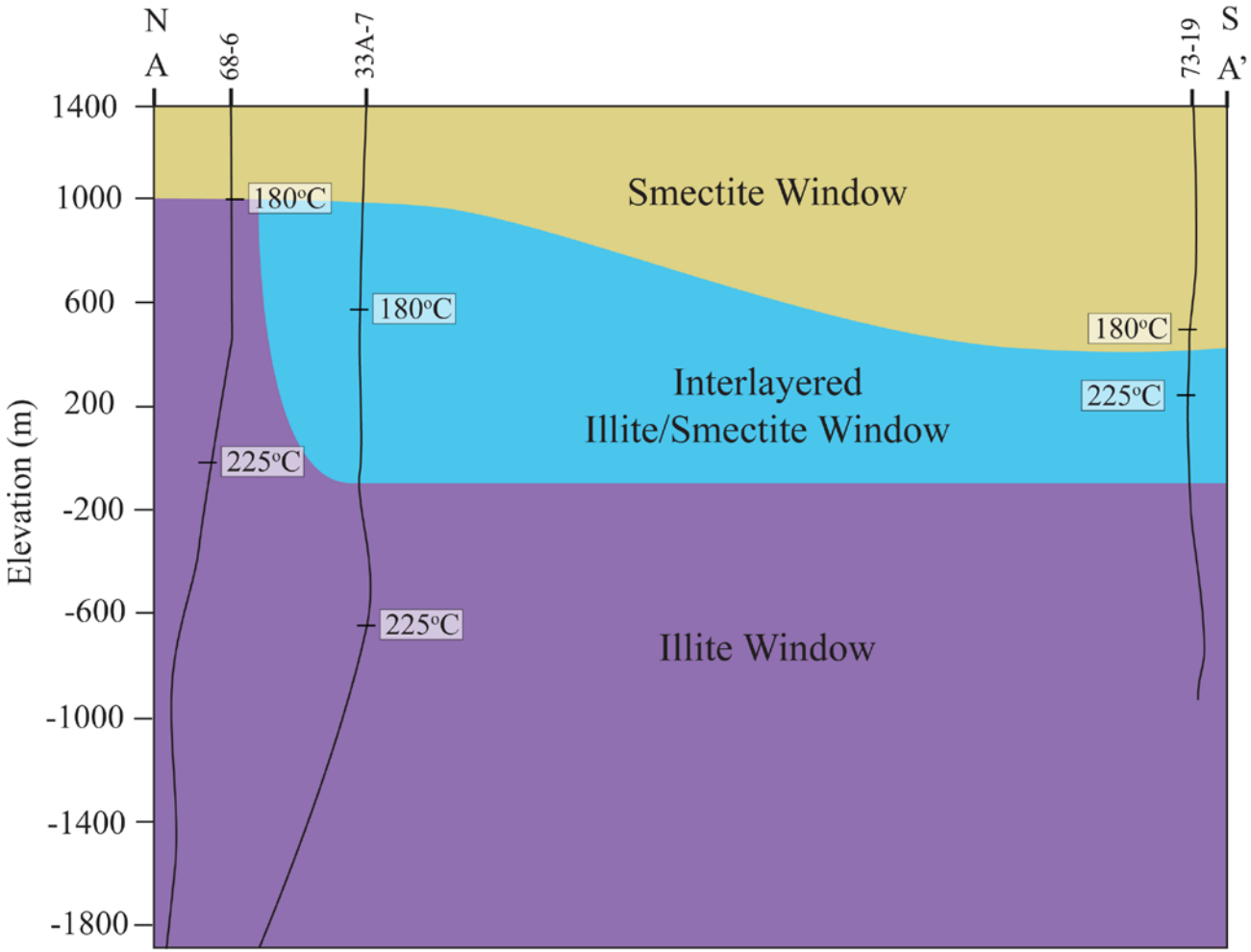


Figure 1.19**:** Vertical cross-section of the distribution of clay minerals (clay zones) at Coso along the transect A-A', based on XRD data. Thermal profile based on preproduction temperatures from wells 68-6, 33A-7 and 73-19. Preproduction temperatures of 180 and 225 ºC in each well are shown.

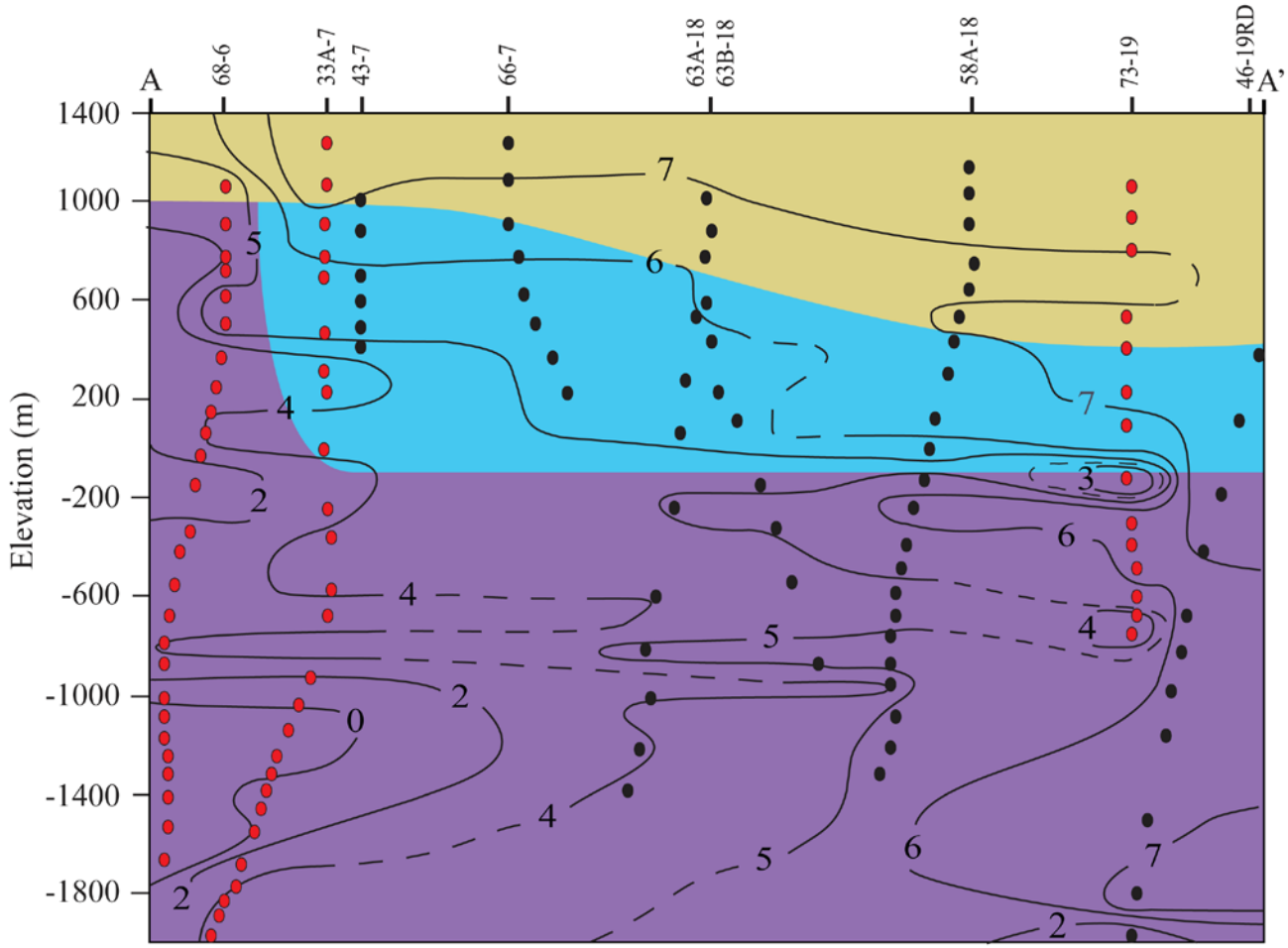


Figure 1.20: Oxygen isotope ($\delta^{18}O$) contours superimposed onto the cross-section of clay window distribution along the traverse A-A' in the West Flank. Black circles represent intervals with preexisting $\delta^{18}O$ values, red circles represent intervals where $\delta^{18}O$ values were determined for this study. Increasing extent of $^{18}O/^{16}O$ depletion northward correlates with changes in clay window zoning with depth, suggesting a correlation between clay mineralogy and permeability (see text for discussion).

Table 1.4: Calculated equilibrium $\Delta_{r\text{-}w}$ and $\Delta_{fsp\text{-}w}$, measured $\Delta_{r\text{-}w}$ and $\Delta_{fsp\text{-}w}$, and W/R ratios for well 68-6. WR = whole-rock; Eq = equilibrium; FSP = feldspar.

| *68-6* ID | W.R. $\delta^{18}O$ | *Eq* $\Delta_{r\text{-}w}$[1] | Measured $\Delta_{r\text{-}w}$[2] | *FSP* $\delta^{18}O$ | *Eq* $\Delta_{fsp\text{-}w}$[1] | Measured $\Delta_{fsp\text{-}w}$[2] | W/R closed | W/R Open |
|---|---|---|---|---|---|---|---|---|
| 271.3 | 3.88 | 9.33 | 12.55 | | | | 0.49 | 0.40 |
| 335.3 | 4.47 | 9.33 | 13.14 | 6.04 | 10.17 | 14.71 | 0.36 | 0.31 |
| 423.7 | 2.55 | 9.33 | 11.22 | | | | 0.80 | 0.59 |
| 487.7 | 3.49 | 9.27 | 12.16 | 6.59 | 10.10 | 15.26 | 0.58 | 0.46 |
| 563.9 | 5.08 | 9.27 | 13.75 | | | | 0.22 | 0.20 |
| 685.8 | 5.78 | 9.03 | 14.45 | | | | 0.06 | 0.05 |
| 722.4 | 6.02 | 8.79 | 14.69 | 6.29 | 9.59 | 14.96 | 0.00 | 0.00 |
| 883.9 | 3.57 | 8.04 | 12.24 | | | | 0.57 | 0.45 |
| 984.5 | 4.07 | 7.68 | 12.74 | | | | 0.45 | 0.37 |
| 1069.8 | 4.30 | 7.36 | 12.97 | | | | 0.40 | 0.33 |
| 1271 | 4.43 | 7.36 | 13.10 | | | | 0.37 | 0.31 |
| 1371.6 | 2.44 | 6.81 | 11.11 | 5.24 | 7.46 | 13.91 | 0.83 | 0.60 |
| 1432.6 | 2.87 | 6.81 | 11.54 | | | | 0.73 | 0.55 |
| 1484.4 | 1.50 | 6.81 | 10.17 | 4.96 | 7.46 | 13.63 | 1.04 | 0.71 |
| 1554.5 | 2.60 | 6.81 | 11.27 | | | | 0.79 | 0.58 |
| 1700.8 | 3.78 | 6.72 | 12.45 | 5.64 | 7.37 | 14.31 | 0.52 | 0.42 |
| 1798.3 | 4.67 | 6.51 | 13.34 | 6.76 | 7.13 | 15.43 | 0.31 | 0.27 |
| 1935.5 | 4.46 | 6.38 | 13.13 | | | | 0.36 | 0.31 |
| 2066.5 | 2.94 | 6.30 | 11.61 | | | | 0.71 | 0.54 |
| 2270.8 | 2.70 | 6.06 | 11.37 | | | | 0.77 | 0.57 |
| 2392.7 | 0.75 | 5.94 | 9.42 | | | | 1.22 | 0.80 |
| 2465.8 | 0.75 | 5.88 | 9.42 | 3.09 | 6.46 | 11.76 | 1.22 | 0.80 |
| 2566.4 | 0.61 | 5.79 | 9.28 | | | | 1.25 | 0.81 |
| 2709.7 | 0.75 | 5.50 | 9.42 | 3.08 | 6.05 | 11.75 | 1.22 | 0.80 |
| 2792 | 2.83 | 5.60 | 11.50 | 3.59 | 6.16 | 12.26 | 0.74 | 0.55 |
| 2849.9 | 0.54 | 5.77 | 9.21 | | | | 1.27 | 0.82 |
| 2895.6 | 0.26 | 5.98 | 8.93 | | | | 1.33 | 0.85 |
| 2941.3 | -4.60 | 5.98 | 4.07 | -3.88 | 6.57 | 4.79 | 2.45 | 1.24 |
| 2984 | -1.05 | 5.73 | 7.62 | 1.76 | 6.30 | 10.43 | 1.63 | 0.97 |
| 3173 | 0.64 | 5.00 | 9.31 | | | | 1.24 | 0.81 |

[1]Equilibrium $\Delta_{r\text{-}w}$ and $\Delta_{fsp\text{-}w}$ fractionation values calculated at preproduction reservoir temperatures using the experimental fractionation factor for $An_{50}$-water and $An_{25}$-water (O'Neil and Taylor, 1967), respectively.

[2] Measured $\Delta_{wr\text{-}w}$ and $\Delta_{fsp\text{-}w}$ are the differences between the measured $\delta^{18}O$ values of whole-rock or feldspar, and the measured $\delta^{18}O$ value of the current geothermal fluid (-8.67 ‰ ).

Table 1.5: Calculated equilibrium $\Delta_{r\text{-}w}$ and $\Delta_{fsp\text{-}w}$, measured $\Delta_{r\text{-}w}$ and $\Delta_{fsp\text{-}w}$, and W/R ratios for well 33A-7. WR = whole-rock; Eq = equilibrium; FSP = feldspar.

| 33A-7 ID | W.R. $\delta^{18}O$ | *Eq* $\Delta_{r\text{-}w}$[1] | Measured $\Delta_{r\text{-}w}$[2] | *FSP* $\delta^{18}O$ | *Eq* $\Delta_{fsp\text{-}w}$[1] | Measured $\Delta_{fsp\text{-}w}$[2] | W/R closed | W/R Open |
|---|---|---|---|---|---|---|---|---|
| 33.5 | 7.62 | 23.44 | 15.11 | 7.50 | 25.34 | 14.99 | 0.00 | 0.00 |
| 109.7 | 3.7 | 19.54 | 11.19 | | | | 0.71 | 0.54 |
| 262.1 | 5.39 | 14.03 | 12.88 | | | | 0.40 | 0.34 |
| 414.5 | 7.45 | 11.00 | 14.94 | | | | 0.03 | 0.03 |
| 566.9 | 4.84 | 11.00 | 12.33 | | | | 0.50 | 0.41 |
| 646.2 | 5.34 | 9.78 | 12.83 | | | | 0.41 | 0.35 |
| 871.7 | 0.2 | 9.30 | 7.69 | | | | 1.35 | 0.85 |
| 1024.1 | 3.59 | 8.70 | 11.08 | | | | 0.73 | 0.55 |
| 1100.3 | 3 | 8.56 | 10.49 | 5.49 | 9.34 | 12.98 | 0.84 | 0.61 |
| 1325.9 | 4.18 | 8.20 | 11.67 | | | | 0.62 | 0.49 |
| 1569.7 | 3.89 | 7.94 | 11.38 | | | | 0.68 | 0.52 |
| 1649 | 2.71 | 7.76 | 10.20 | | | | 0.89 | 0.64 |
| 1877.6 | 1.03 | 7.39 | 8.52 | | | | 1.20 | 0.79 |
| 1984.2 | 3.93 | 7.20 | 11.42 | | | | 0.67 | 0.51 |
| 2136.6 | 1.6 | 6.81 | 9.09 | | | | 1.09 | 0.74 |
| 2212.8 | -0.44 | 6.70 | 7.05 | | | | 1.46 | 0.90 |
| 2322.6 | -0.02 | 6.49 | 7.47 | | | | 1.39 | 0.87 |
| 2322.6 | -1.02 | 6.49 | 6.47 | | | | 1.57 | 0.94 |
| 2350 | -0.98 | 6.44 | 6.51 | | | | 1.56 | 0.94 |
| 2380.5 | 0.14 | 6.38 | 7.63 | | | | 1.36 | 0.86 |
| 2471.9 | 0.51 | 6.18 | 8.00 | -2.37 | 6.78 | 5.12 | 1.29 | 0.83 |
| 2502.4 | -2.35 | 6.06 | 5.14 | | | | 1.81 | 1.03 |
| 2529.8 | -3.08 | 6.02 | 4.41 | -0.03 | 6.61 | 7.46 | 1.94 | 1.08 |
| 2566.4 | 0.94 | 6.02 | 8.43 | 4.16 | 6.61 | 11.65 | 1.21 | 0.79 |
| 2593.8 | 2.15 | 5.96 | 9.64 | 4.20 | 6.55 | 11.69 | 0.99 | 0.69 |
| 2624.3 | 1.55 | 5.85 | 9.04 | | | | 1.10 | 0.74 |
| 2654.8 | 2.92 | 5.79 | 10.41 | | | | 0.85 | 0.62 |
| 2685.3 | 2.1 | 5.73 | 9.59 | 4.60 | 6.30 | 12.09 | 1.00 | 0.69 |
| 2746.2 | 3.91 | 5.60 | 11.40 | | | | 0.67 | 0.51 |
| 2837.7 | 4.48 | 5.48 | 11.97 | 5.49 | 6.03 | 12.98 | 0.57 | 0.45 |
| 2959.6 | 4.6 | 5.25 | 12.09 | | | | 0.55 | 0.44 |

Table 1.5 (continued)

| 33A-7 ID | W.R. $\delta^{18}O$ | *Eq* $\Delta_{r-w}$[1] | Measured $\Delta_{r-w}$[2] | *FSP* $\delta^{18}O$ | *Eq* $\Delta_{fsp-w}$[1] | Measured $\Delta_{fsp-w}$[2] | W/R closed | W/R Open |
|---|---|---|---|---|---|---|---|---|
| 2990.1 | 4.25 | 5.20 | 11.74 | | | | 0.61 | 0.48 |
| 3020.6 | 4.05 | 5.16 | 11.54 | | | | 0.65 | 0.50 |
| 3051 | 1.78 | 5.13 | 9.27 | | | | 1.06 | 0.72 |
| 3081.5 | 4.21 | 5.13 | 11.70 | | | | 0.62 | 0.48 |
| 3112 | 4.03 | 5.00 | 11.52 | | | | 0.65 | 0.50 |
| 3142.5 | 4.61 | 4.95 | 12.10 | | | | 0.55 | 0.44 |
| 3173 | 4.1 | 4.84 | 11.59 | | | | 0.64 | 0.49 |
| 3233.9 | 4.49 | 4.76 | 11.98 | | | | 0.57 | 0.45 |
| 3294.9 | 3.88 | 4.68 | 11.37 | 5.90 | 5.17 | 13.39 | 0.68 | 0.52 |

[1]Equilibrium $\Delta_{r-w}$ and $\Delta_{fsp-w}$ fractionation values calculated at preproduction reservoir temperatures using the experimental fractionation factor for $An_{50}$-water and $An_{25}$-water (O'Neil and Taylor, 1967), respectively.

[2] Measured $\Delta_{wr-w}$ and $\Delta_{fsp-w}$ are the differences between the measured $\delta^{18}O$ values of whole-rock or feldspar, and the measured $\delta^{18}O$ value of the current geothermal fluid (-7.49 ‰).

Table 1.6: Calculated equilibrium $\Delta_{r\text{-}w}$ and $\Delta_{fsp\text{-}w}$, measured $\Delta_{r\text{-}w}$ and $\Delta_{fsp\text{-}w}$, and W/R ratios for well 73-19. WR = whole-rock; Eq = equilibrium; FSP = feldspar.

| *73-19* ID | W.R. $\delta^{18}O$ | *Eq* $\Delta_{r\text{-}w}$[1] | Measured $\Delta_{r\text{-}w}$[2] | *FSP* $\delta^{18}O$ | *Eq* $\Delta_{fsp\text{-}w}$[1] | Measured $\Delta_{fsp\text{-}w}$[2] | W/R closed | W/R Open |
|---|---|---|---|---|---|---|---|---|
| 271.3 | 6.98 | 16.10 | 12.54 | 7.79 | 17.43 | 13.35 | 0.08 | 0.08 |
| 381 | 6.61 | 14.08 | 12.17 | | | | 0.13 | 0.12 |
| 390.1 | 6.37 | 14.03 | 11.93 | | | | 0.16 | 0.15 |
| 445 | 7.48 | 13.35 | 13.04 | 8.12 | 14.47 | 13.68 | 0.01 | 0.01 |
| 545.6 | 5.52 | 11.78 | 11.08 | | | | 0.28 | 0.24 |
| 777.2 | 7.57 | 8.85 | 13.13 | | | | 0.00 | 0.00 |
| 798.6 | 6.36 | 8.62 | 11.92 | | | | 0.16 | 0.15 |
| 1060.7 | 7.16 | 6.37 | 12.72 | | | | 0.06 | 0.05 |
| 1072.9 | 7.41 | 6.25 | 12.97 | | | | 0.02 | 0.02 |
| 1225.3 | 6.07 | 5.47 | 11.63 | | | | 0.20 | 0.18 |
| 1316.7 | 6.63 | 5.12 | 12.19 | | | | 0.13 | 0.12 |
| 1347.2 | 5.91 | 5.12 | 11.47 | | | | 0.22 | 0.20 |
| 1386.8 | 4.61 | 4.92 | 10.17 | 6.14 | 5.42 | 11.70 | 0.40 | 0.33 |
| 1411.2 | 2.38 | 5.00 | 7.94 | | | | 0.70 | 0.53 |
| 1481.3 | 6.3 | 4.69 | 11.86 | 7.26 | 5.18 | 12.82 | 0.17 | 0.16 |
| 1581.9 | 5.94 | 4.55 | 11.50 | | | | 0.22 | 0.20 |
| 1664.2 | 6.85 | 4.39 | 12.41 | | | | 0.10 | 0.09 |
| 1709.9 | 5.13 | 4.26 | 10.69 | | | | 0.33 | 0.28 |
| 1813.6 | 5.14 | 4.63 | 10.70 | 6.20 | 4.69 | 11.76 | 0.33 | 0.28 |
| 1834.9 | 3.3 | 4.95 | 8.86 | 6.34 | 4.69 | 11.90 | 0.57 | 0.45 |
| 1856.2 | 3.3 | 4.86 | 8.86 | | | | 0.57 | 0.45 |

[1]Equilibrium $\Delta_{r\text{-}w}$ and $\Delta_{fsp\text{-}w}$ fractionation values calculated at pre-production reservoir temperatures using the experimental fractionation factor for $An_{50}$-water and $An_{25}$-water (O'Neil and Taylor, 1967), respectively.

[2] Measured $\Delta_{wr\text{-}w}$ and $\Delta_{fsp\text{-}w}$ are the differences between the measured $\delta^{18}O$ values of whole-rock or feldspar, and the measured $\delta^{18}O$ value of the current geothermal fluid (-5.56 ‰).

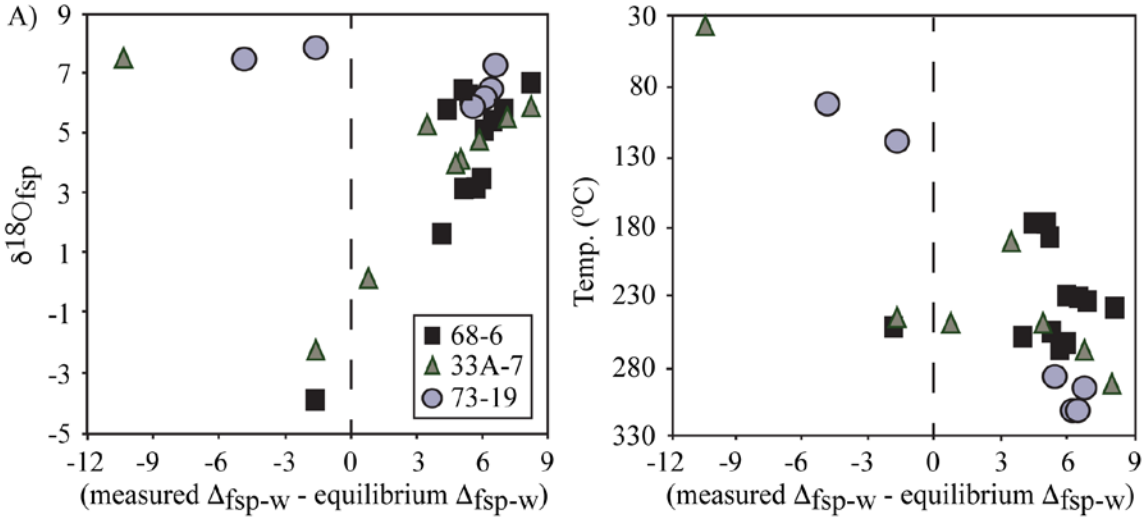


Figure 1.21: Evaluating departures from isotope exchange equilibrium. A) The difference between measured $\Delta_{fsp\text{-}w}$ and equilibrium $\Delta_{fsp\text{-}w}$ plotted against the measured $\delta^{18}O$ value of each feldspar separate. B) The difference between measured $\Delta_{fsp\text{-}w}$ and equilibrium $\Delta_{fsp\text{-}w}$ plotted against measured temperature (preproduction) for the feldspar sample. Equilibrium $\Delta_{fsp\text{-}w}$ is calculated at measured temperatures (preproduction). The dashed line in both plots represents equilibrium (that is, measured $\Delta_{fsp\text{-}w}$ = equilibrium $\Delta_{fsp\text{-}w}$) between analyzed feldspar and the current reservoir fluid. Samples plotting to right of the dashed line have a measured $\Delta_{fsp\text{-}w}$ > equilibrium $\Delta_{fsp\text{-}w}$; these feldspars have incompletely exchanged oxygen isotopes with the current reservoir fluid.

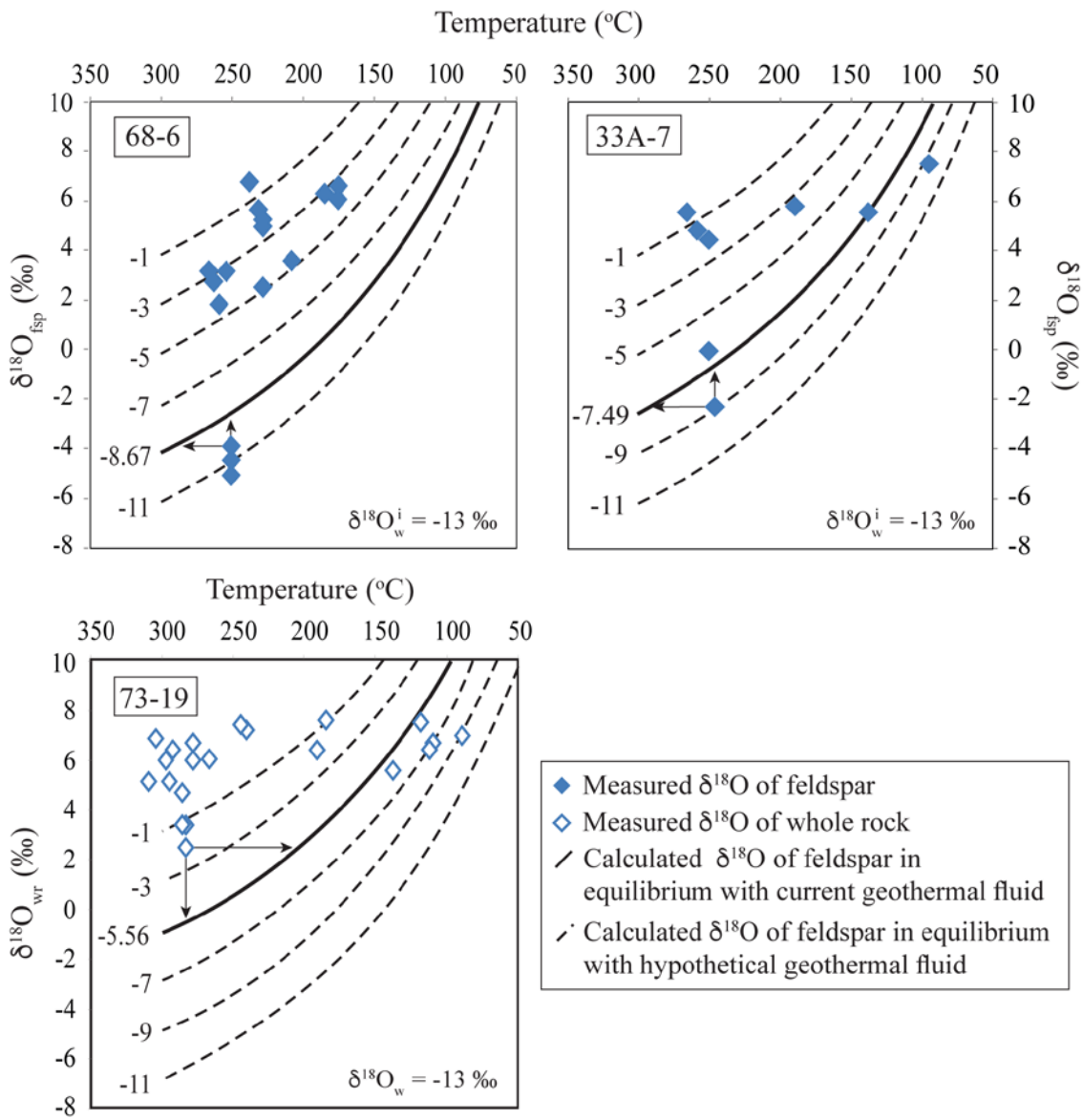


Figure 1.22: Measured $\delta^{18}O$ values of feldspar (from wells 68-6 and 33A-7) and whole-rock (from well 73-19) plotted as a function of preproduction temperatures. Curved lines define the calculated $\delta^{18}O$ values of feldspar or whole rock in equilibrium with a range of $\delta^{18}O$ values of geothermal fluid (values specified next to each curve), including current values (solid line), as a function of temperature. Arrows indicate changes in temperature or $\delta^{18}O$ of reservoir fluid needed for measured feldspar to achieve oxygen isotope exchange equilibrium with current geothermal fluids.

CHAPTER 2

# TOURMALINE IN GEOTHERMAL SYSTEMS: AN EXAMPLE FROM DARAJAT, INDONESIA

## 2.1 Introduction

Tourmaline is a common accessory mineral in a variety of geologic settings (Hawthorne and Henry, 1999; Henry and Dutrow, 2012). Based on specific compositions, this refractory mineral can provide detailed information about its crystallizing environment; for this reason, it is becoming increasingly common to analyze tourmalines for various geologic studies (Cavarretta and Puxeddu, 1990; Henry and Dutrow, 1996, 2012; Trumbull et al., 1999; Moore et al., 2004; Jiang et al., 2008; Collins, 2010; Pal et al., 2010; Dill et al., 2012; Gupta et al., 2014).

This supergroup borosilicate mineral is able to incorporate a range of major and trace elements into the cation and anion sites of the general formula $XY_3Z_6(T_6O_{18})(BO_3)_3V_3W$. Typical elements for each site include: X = Na, Ca, K, □; Y = Li, Mg, $Fe^{2+}$, $Mn^{2+}$, Al, $Ti^{4+}$; Z = Mg, Al, $Fe^{3+}$, $Cr^{3+}$, $V^{3+}$; T = Si, Al, B; B = B, V = OH, O; W = OH, O, Cl, F (Hawthorne and Henry, 1999; Henry et al., 2011). This spectrum of elements accessible for site substitution has led the IMA-CNMNC to officially recognize 17 ideal end-members (Henry et al., 2011).

The composition of tourmaline crystallizing in active geothermal systems can

reveal information about fluid flow and sources of the major ion constituents (i.e., whether elements such as B, F, Na, Ca, Mg, Mn, Ti are leached from the host rock during water-rock interactions, externally derived and transported by thermal fluids or a combination of the two). Therefore, their chemistry can provide details regarding the evolution of a geothermal system (Cavarretta and Puxeddu, 1990; Moore et al., 2004). Tourmalines have been identified in other geothermal systems, but very few occurrences in higher temperature vapor-dominated systems have been well characterized in mineral chemistry. This chapter describes the mineral paragenesis and composition of tourmaline from the vapor-dominated geothermal system at Darajat, Indonesia. These compositions are then compared to tourmalines from a variety of geothermal and magmatic systems to better understand water-rock interaction at Darajat. Finally, these observations are used to explain the evolution of this geothermal system.

### 2.1.1 The Darajat Geothermal System

Darajat is a volcanic hosted geothermal system located on the flanks of Gunung Papandayan and Gunung Guntur (two active volcanoes) in West Java, Indonesia (Figure 2.1). In general, the system is part of an older collapsed andesitic stratovolcano overlain by younger volcanic material; the lower section consists of lavas and instrusives that are tholeiitic to calc-alkaline in composition. These are overlain by a thick sequence of alternating pyroclastics and andesitic lavas. Magneto-telluric/time domain electro-magnetic (MT/TDEM) surveys and micro-earthquake (MEQ) array data have revealed a number of major faults (Rejeki et al., 2010).

Rejeki et al. (2010) defined the borders of the reservoir (Figure 2.2) by integrating

down-hole temperature profiles, electrical resistivity data, alteration mineralogy and MEQ data. A correlation between the conductive-convective heating boundary and an electric resistive transition from low to high has helped constrain the top of the reservoir at around 0 to 700 m above sea level (depending on location); confidently defining the bottom of the reservoir has been problematic, however, with estimates varying from between -1200 m and -2000 m (most accepted depths) to between -2200 m and -3500 m (Rejeki et al., 2010).

## 2.2 Analytical Methods

Thin sections of core samples from four depths, namely 670.6 m, 870.7 m, 821.4 m and 975.4 m, were analyzed. Detailed petrographic observations were made using a standard transmitted light microscope to identify primary lithologies and alteration mineralogy at each interval. Electron microprobe analyses of tourmaline were conducted at the University of Utah using a Cameca BX50 automated electron microprobe (EMP) with 4 wavelength dispersive spectrometers, an accelerating voltage of 15 kV, 20 nA sample current and a 1 micron beam diameter. Standards used were Albite (Na), Sanidine (Al, K), Diopside (Mg, Ca, Si), Rutile (Ti), Rhodonite (Mn), Hematite (Fe), Fluorite (F) and Tugtupite (Cl).

## 2.3 Results

### 2.3.1 Petrographic Observations

It is necessary to understand the lithology and alteration mineralogy at each interval in order to deduce meaningful physicochemical information that may influence

tourmaline compositions. Hence, a detailed petrographic study of core from well DRJ-S1 has been conducted to define the reservoir host-rock lithology and alteration mineralogy (Figure 2.3). Previous petrographic interpretations made by others (Moore, 2007; Moore and Jones, 2014) in wells DRJ-18ST1, DRJ-21 and DRJ-29 (Figures 2.4-2.6) have also been used for this study.

Two distinct lithologies are found in well DRJ-S1 (Figure 2.3). The first lithology encountered is alternating lahar/ash-flow tuffs. These alternating layers, found between 255 meters and 778 meters, are argillically altered. Lahars consist of both andesite lava clasts with fractured quartz, plagioclase and pyroxene crystals, and brecciated veins of cemented diorite fragments. Altered ash flow tuffs contain fragments of quartz and plagioclase phenocrysts in a fine-grained quartz and clay-rich matrix. Plagioclase phenocrysts have been altered to smectite, illite, calcite and quartz; pyroxenes replaced by smectite, pyrite and quartz are also observed. Typical secondary minerals include quartz, smectite, illite, interlayered illite-smectite, interlayered chlorite-smectite, pyrite, calcite, anhydrite, rutile, fluorite, titanite and tourmaline, all found as replacements and in vein assemblages.

Below 778 meters, in the present day steam reservoir, the dominant lithology is equigranular to porphyritic diorites (referred to as the Andesite Complex). This diorite primarily consists of plagioclase with a minor amount of clinopyroxene and quartz. Plagioclase phenocrysts display a varying extent of alteration to epidote, chlorite, calcite, illite and occasionally anhydrite, while clinopyroxene phenocrysts have altered to actinolite, chlorite and titanite. The majority of the diorite is propylitically altered with occasional intervals of biotite hornfels.

Intrusion of the diorite produced biotite hornfels from contact metamorphism. It consists of relatively fresh plagioclase, clinopyroxene typically altered to actinolite and biotite altered to chlorite.

Moore (unpublished, 2007) defined four stages of hydrothermal alteration in the Darajat system based on textural and vein relationships (Table 2.1). Each stage is associated with geothermal activity in the evolution of the geothermal system. Petrographic observations made for this study confirm the presence of these four distinct hydrothermal stages in well DRJ-S1. Each stage is defined by a distinct secondary mineralogy.

Stage 1 is argillic-phyllic alteration at shallow depths and propylitic alteration deeper in the reservoir. Petrographic evidence indicates that these stage 1 assemblages formed during the early stages of hydrothermal alteration (Table 2.1). Secondary minerals include smectite, interlayered illite-smectite and calcite in the shallow, argillic altered portion of the system, and epidote, chlorite, illite, tourmaline, actinolite, prehnite, pyrite, adularia and biotite in the deeper propylitically altered reservoir. It is important to consider the vertical distribution of smectite, interlayered illite-smectite and illite as their presence can be sensitive to temperature (Henley and Ellis, 1983; Reyes, 1990). Pure smectite occurs in the shallowest depths of well DRJ-S1; at ~ 400 m smectite has begun to convert to interlayered illite-smectite. Previous work has shown that the disappearance of interlayered clays and the presence of illite and chlorite mark the base of the argillic zone and the top of the phyllic zone in other portions of the Darajat system (Moore unpublished, 2007 and 2014).

Epidote associated with Stage 1 is first observed near the top of the diorite

intrusions and marks the upper boundary of the propylitic zone at a depth of 807.7 meters. It commonly occurs as a replacement mineral of plagioclase, but is also a constituent of many vein assemblages. Frequently epidote is encapsulated by prehnite. Moore (unpublished report, 2007) also recognized this paragenetic relationship in other regions of the Darajat reservoir and concluded that the formation of prehnite after epidote reflects waning temperatures based on calculated mineral stability relationships.

Tourmaline associated with Stage 1 (Figure 2.7) alteration assemblages occurs near the upper contact of the diorite intrusions and within the intrusive rocks. Similar early stage tourmalines identified at Larderello, Italy, and The Geysers, California, formed during the liquid-dominated stages of geothermal activity at distances up to 300 m from the intrusions (Cavarretta and Puxeddu, 1990; and Moore and Gunderson, 1995). A similar occurrence of tourmaline has also been observed at Karah-Telaga Bodas (Moore et al., 2004a).

Stage 2 is defined by the precipitation of quartz and chalcedony, a microcrystalline intergrowth between quartz and mogenite. The deposition of chalcedony is significant because quartz is the stable polymorph above 180 $^{o}$C (Fournier, 1985). Quartz and chalcedony cemented veins often encase fragments of wall rock, indicating brecciation. This, alongside banded chalcedony identified petrographically, indicates boiling. At Karaha – Telaga Bodas, similar banded chalcedony precipitated following a tectonic flank collapse resulting in catastrophic depressurization (Moore et al., 2008).

Stage 3 is characterized by advanced argillic alteration and anhydrite, calcite and tourmaline-filled veins at shallow depths. These veins also contain minor amounts of pyrite, chlorite and clays. Cross-cutting relationships indicate the precipitation of

anhydrite post dates Stage 1 alteration assemblages. Late stage wairakite deeper in the reservoir is also associated with Stage 3.

Stage 3 tourmaline is found along the margins of anhydrite veins (Figure 2.8). At shallow depths, it is found as aggregates of radiating needle-like crystals while slightly coarser grained aggregates are observed deeper in the well. Similar veins of anhydrite and tourmaline were observed at Karaha – Telaga Bodas. Using numerical simulations, Moore et al. (2004a) showed that this vein package was the product of descending acid lake waters reacting with the andesitic host rock.

Stage 4 is defined by continued sparse advanced argillic alteration and silicification of pyroclastics above the diorite intrusions. Widespread silicification of these rocks suggests cation leaching resulting from the interaction with acid sulfate condensates. Alunite, commonly associated with advanced argillic alteration, was not found in DRJ-S1; however, kaolinite, a mineral commonly associated with a low pH environment, was identified in these intervals.

### 2.3.2 Tourmaline Chemistry

Two tourmaline populations identified petrographically are each related to separate hydrothermal stages. Tourmalines associated with Stage 1 were analyzed from intervals 975.4 m and 807.7 m, while Stage 3 tourmalines were analyzed from intervals 821.4 m and 670.1 m. Chemical compositions and calculated mineral chemistry by spot are presented in Table 2.2 and illustrated in Figures 2.9 and 2.10. For comparison, compositions of tourmaline from Karaha-Telaga Bodas (Moore et al., 2004), The Geysers (Jones et al., in prep), Larderello (Cavarretta and Puxeddu, 1990) and two intrusive

systems (Jiang et al., 2008; Dill et al., 2012) are also shown (Figures 2.9 and 2.10). The tourmalines from Karaha and The Geysers occur in association with mineral assemblages characteristic of Stage 3 at Darajat, and the tourmalines from Larderello and the two intrusive systems occur in mineral associations characteristic of Stage 1 at Darajat. Structural formulae were calculated on the basis of the general formula $XY_3Z_6(T_6O_{18})(BO_3)_3V_3W$ by normalizing the sum of T+Y+Z to 15 (15 cations). Light elements (B, H, O) could not be analytically determined; boron was assumed to be stoichiometric (i.e., B = 3) following the justification provided by Henry and Dutrow (1996); oxygen and hydrogen were determined following the procedure originally described by Grice and Erict (1993). Li, assumed to be a negligible component in these tourmaline samples, has not been accounted for. All iron is assumed to be $Fe^{2+}$. Chemical variation is most noticeable in Al, Ca, Na, Mg and $Fe_{tot}$, while K, Ti, Mn, F and Cl concentrations are minimal and show little variation with depth or between stages. Compositionally, most tourmaline samples plot within the alkali group (Figure 2.9). Three analyses with no computed X-site vacancies plot within the calcic group on the right arm of the ternary diagram. These analyzed grains are quite small, so this high Ca concentration could, in part, be the result of additional mineral phases inadvertently contributing to those tourmaline analyses. However, some progressive calcic enrichment occurs in tourmalines in data from sample 821.4.

Tourmalines have been further subdivided into specific end-member categories following an accepted computational procedure (Henry et al., 2011) illustrated in Figure 2.10. Computed tourmaline compositions range from schorl-dravite (alkali abundant subcategories) to uvite-feruvite compositions (calcic abundant subcategories). Stage 1

tourmalines are intermediate schorl-dravite in composition. Tourmalines from interval 975.4 would be classified as schorl, save one Ca-rich analysis that is classified as uvite. Tourmalines from interval 807.7 are dravitic. Stage 3 tourmalines range from dravite to uvite; tourmalines from interval 670.1 are predominately dravitic, with a small number of calcic-rich specimens plotting in the uvite field, while tourmalines from interval 821.4 m range from intermediate dravite-uvite to dravite in composition.

Stage 1 tourmalines have distinctly higher and more variable Fe/(Mg + Fe) ratios than Stage 3 tourmalines, with interval 975.4 having the overall highest values (Figure 2.10a). This variation in Fe/(Mg + Fe) is best described by the $FeMg_{-1}$ exchange vector (Figure 2.10b). Henry and Dutrow (1996) pointed out that metagranitoid tourmalines are typically enriched in Fe. For example, main stage metagranitoid tourmalines in Hnilec granites (Jiang et al., 2008) have very Fe-rich compositions (Fig. 2.10a). Stage 1 tourmalines at Darajat formed during the early stages of hydrothermal alteration shortly after pluton emplacement, and are therefore related to metamorphism in the contact aureole. Tourmalines documented from similar occurrences at Karaha-Telaga Bodas, Indonesia (Moore et al., 2008), Larderello, Italy (Cavarretta and Puxeddu, 1990) and at the Geysers, California, have similar Fe/(Mg + Fe) ratios (Figure 2.10a), attesting to the metamorphic nature of Stage 1 tourmalines at Darajat.

With one exception, Stage 1 tourmalines have higher Na/(Na + Ca) ratios than Stage 3 tourmalines (Figure 2.10a), but Stage 3 tourmalines have more variable Na/(Na + Ca) ratios than Stage 1 tourmalines. Both groups of tourmaline exhibit significant variations in Na and Al contents (Figure 2.10c). However, Na is negatively correlated with Al in Stage 1 tourmalines, with two exceptions, and Na is positively correlated with

Al in Stage 3 tourmalines, primarily within the tourmalines from interval 670.1 m. The $NaAl(CaMg)_{-1}$ exchange vector can explain in general the positive correlation of Na and Al, and variable Na/(Ca + Na) (Na-Ca substitution) on the X-site in Stage 3 tourmalines (Figure 2.10c). However, because Na/(Ca + Na) ratios are relatively constant in Stage 1 tourmalines, the variations in Na content in Stage 1 tourmalines are more likely the result of the $NaMg(\square Al)_{-1}$ exchange vector (Figure 2.10c).

Natural and laboratory-generated data have revealed a correlation between increasing Na content of tourmaline and increasing temperature in a metamorphic environment (Henry and Dutrow, 1996; von Goerne et al., 2001). The Na-enriched Stage 1 tourmalines likely formed at higher reservoir temperatures than did Stage 3 tourmalines, although fluid inclusion data are needed for validation. However, reservoir rock chemistry will also have an important impact on tourmaline composition. Stage 1 tourmalines formed at the expense of magmatic minerals enriched in Na, while Stage 3 tourmalines formed in anhydrite veins sourcing cations from a Ca-enriched hydrothermal fluid.

Despite the occurrence of fluorite and zunyite in Stage 3, fluorine is a relatively insignificant component of tourmalines except for interval 670.1. Although Henry and Dutrow (2011) found that as X-site charge decreases F content also decreases, our limited data set fails to produce a similar observation. The significance of F- and B-bearing minerals, however, is that they suggest a magmatic contribution to hydrothermal fluids during the formation of Assemblage 3.

## 2.4 Discussion

### 2.4.1 Initial Hydrothermal Activity

Propylitic alteration is not observed above the diorite (Andesite Complex) in well DRJ-S1 (Figure 2.3). In other wells, however, the propylitic mineral assemblage extends to shallow depths (Figures 2.4). Epidote distribution shows no relationship to the modern geothermal system and is only observed in the diorites (Moore, 2007); at Karaha – Telaga Bodas, epidote is spatially associated with the underlying granodiorite intrusion and has been observed more than 300 m away from the intrusive contact (Moore et al., 2008). It is reasonable to infer then that the epidote surface should extend beyond the intrusive contact at Darajat. The abrupt disappearance of epidote above the intrusive contact (~810 m) in well DRJ-S1 suggests an erosional event that removed overlying propylitically altered strata prior to the deposition of the younger alternating tuff layers.

### 2.4.2 Compositional Evolution of Tourmaline-Forming Fluids/Environment

The tourmaline geochemical data are used to better understand early water-rock interactions occurring at Darajat during the liquid-dominated stage. Stage 1 tourmalines compositionally resemble tourmalines formed during the early stages of hydrothermal alteration at Larderello (Cavarretta and Puxeddu, 1990), the San Jorge porphyry Cu deposit (Dill et al., 2012) and at The Geysers (Jones et al., unpublished) (Figures 2.9 and 2.10). At Larderello, it was shown that tourmaline growth occurred in a high temperature, liquid-dominated environment. A similar interpretation was also made for early stage tourmalines at Karaha – Telaga Bodas (Moore et al., 2008). At Darajat Stage 1 would have formed in a similar environment with near-neutral pH NaCl waters (Ellis and

Mahon, 1977). Tourmaline formation is, however, pH sensitive and favors acidic to slightly acidic environments (Morgan and London, 1989); its presence plus the absence of alunite (associated with low pH) therefore suggests early fluids were mildly acidic.

Chemical variations between both populations of Stage 1 tourmalines (975.4 and 821.4) highlights the influence of wall-rock chemistry and temperature to secondary mineral chemistry. Tourmaline at interval 975.4 most closely resembles Na-rich metamorphic tourmalines precipitated in higher temperature conditions. Alteration of mafic minerals present in the contact aureole is responsible for high Fe content in this subgroup. Due to progressive water-rock interaction introducing more Fe ions into solution, Stage 1 tourmalines precipitated at 807.7 m are intermediate in composition between the metamorphic tourmalines present at interval 975.4 and Assemblage 3 tourmalines.

A significant feature of the mineral assemblages in the tourmaline-bearing Darajat wells is the presence of minerals characteristic of advanced argillic alteration (Figure 2.11). These minerals are diaspore, pyrophyllite, zunyite and kaolinite. Silification and intense cation leaching has also occurred. In places, alunite and fluorite are also present. Calcite and anhydrite are common. Pyrophyllite and diaspore are diagnostic of temperatures exceeding ~250 $^{o}$C and acidic conditions (pH <2-3). Stage 3 tourmaline and fluorite are temporally associated with Stage 3 advanced argillic alteration assemblages but persist to greater depths.

Stage 3 tourmalines exist as a fracture-filling phase alongside late-stage calcite and anhydrite overprinting earlier propylitic assemblages containing quartz, epidote and actinolite. Due to the retrograde solubility of both calcite and anhydrite, tourmaline-

bearing anhydrite veins were deposited by downward percolating acid-sulfate waters that developed as steam condensate drained downward. Water-rock interactions acted to neutralize the descending acid-condensates by introducing Ca ions, leached from the plagioclase abundant wall-rock, into solution. This resulted in generally higher Ca/(Ca+Na) ratios for Stage 3 tourmalines.

Moore et al. (2008) described similar relationships at Karaha-Teaga Bodas. They observed tourmaline in well T-2, the well drilled closest to the acid Telaga Bodas Lake. This lake is interpreted to overlie a magmatic vapor chimney; the lake's composition is strongly influenced by magmatic gases, particularly HCl and $SO_2$. Advanced argillic alteration occurred in the upper part of T-2 and, in addition to tourmaline, fluorite and native sulfur were locally present. These minerals were not found in other wells at Karaha-Telaga Bodas. Fluid inclusions trapped in anhydrite indicate that tourmaline deposition occurred at temperatures of about 235 $^{o}$C. Based on these relationships, it was concluded that the B and F were magmatic in origin.

The origin of B and F at Darajat is less certain, although the close association of tourmaline with disaspore, pyrophyllite and the F-bearing minerals zunyite and fluorite strongly suggests a magmatic origin. B isotope analyses on tourmaline could help confirm this interpretation.

### 2.4.3 Conceptual Evolution of Darajat

Darajat is currently a vapor-dominated system. Hydrothermal mineral assemblages identified in this work and previous work (Herdianita, 2001) suggest the system was once liquid dominated. Using paragenetic relationships, a conceptual model

for the evolution of this geothermal system has been conceptualized (Figure 2.12).

Stage 1 alteration minerals indicate an early liquid dominated system (Figure 2.12a). Shallow argillic-phyllic alteration and deep propylitic alteration indicate temperatures increased with depth. The presence of tourmaline near the top of the diorites suggests that 1) temperatures exceeded 300 $^{o}$C (Corbett and Leach, 1998) and 2) magmatic fluids introduced B into the system.

Widespread Stage 2 chalcedony deposition signifies a change in the physiochemical conditions of the reservoir. Chalcedony in geothermal systems indicates temperatures below 180 $^{o}$C (Fournier, 1985) and is therefore rarely observed in the propylitically altered, high temperature portions of a system. Fluid inclusion data from this generation of chalcedony are needed to constrain temperatures during this time. However, vapor-rich inclusions trapped in chalcedony observed by Moore (2007) suggests a rapid reduction in reservoir pressures, allowing fluids to flash, thus creating vapor to be trapped in inclusions as chalcedony deposited. Rapid depressurization resulting in the deposition of chalcedony also occurred in Karaha – Telaga Bodas; this was interpreted to result from a flank collapse event (Moore et al., 2008). It is possible this too occurred at Darajat (Figure 2.12b). Alternatively, movement along the Kendang fault could have led to rapid depressurization. Therefore, Stage 2 marks the transition from liquid-dominated to vapor-dominated.

During Stage 3 alteration, ascending magmatic volatiles condensed, forming acidic fluids that migrated laterally and downward through fractures and faults (Figure 2.12c). These migrating acidic fluids that were enriched in $H_2S$, $SO_4$ and $CO_2$ interacted with the wall-rock, resulting in advanced argillic alteration at shallow depths, similar to

how advanced argillic alteration occurred at the high-sulfidation epithermal Au-Ag-Cu Pascua deposit in Chile (Chouinard et al., 2005). This interaction gradually increased the pH. As these slightly acid-to-near neutral waters continued to descend, below the advanced argillic horizon, increasing temperatures resulted in calcite and anhydrite deposition. Physiochemical conditions were such that boric acid in solution also reacted with Ca ions and the surrounding wall-rock to crystallize Stage 3 tourmalines. The magmatic source that introduced relatively unaltered (therefore presumably younger) dacites observed in DRJ-41 and DRJ-43 (Figure 2.11) may have been the source of $SO_2$, $CO_2$, B and F. Alternatively, vapors already present in the reservoir could have been enriched in $SO_2$, $CO_2$, B and F. Continued fracture filling decreased the porosity and permeability, impeding reservoir recharge, therefore sustaining vapor dominated conditions that still persist.

## 2.5 Conclusions

Petrologic and geochemical observations offer new insights into water-rock interactions occurring at Darajat. The following conclusions can be made:

1) Two distinct tourmaline populations are present. Stage 1 tourmalines crystallized in a higher temperature environment following emplacement of the initial diorite intrusions; this population has higher Na/(Na + Ca) ratios and Fe abundances. Later, Stage 3 tourmalines formed on calcite and anhydrite vein margins as descending condensates interacted with the surrounding wall-rock. This population formed below the advanced argillic alteration horizon once the

descending fluids were sufficiently neutralized.

2) Based on tourmaline mineral chemistry, initial hydrothermal fluids were enriched in Na and magmatic B. Sporadic magmatic activity following a flank collapse introduced additional B and F into solution.

3) Hydrothermal mineral assemblages reflect a complex history of geothermal activity at Darajat. Deep propylitic alteration seen in the diorite samples occurred in an early liquid dominated system. Next, chalcedony deposited in response to boiling following catastrophic depressurization. Volatiles present in the reservoir condensed upon ascent and formed acid fluids responsible for advanced argillic alteration observed in the lahars and tuffs; as these fluids migrated downward and laterally, they were neutralized through water-rock interactions. Heating of these descending fluids resulted in the precipitation of calcite and anhydrite. This fracture-filling episode reduced porosity and permeability, prohibiting meteoric recharge, thus creating the current vapor-dominated geothermal system.

## 2.6 References

Bogie, I., and MacKenzie, K. M. (1998) The application of a volcanic facies model to an andesitic stratovolcano hosted geothermal system at Wayang Windu, Java, Indonesia: Proceedings 20th New Zealand Geothermal Workshop

Cavarretta, G., and Puxeddu, M. (1990) Schorl-dravite-ferridravite tourmalines deposited by hydrothermal magmatic fluids during early evolution of the Larderello geothermal field, Italy: Economic Geology, v. 85, p. 1236-1251

Chouinard A., Williams-Jones, A. E., Leonardson, R. W., Hodgson, C. J., Silva, P., Tellez, C., Vega, J., and Rojas F. (2005) Geology and genesis of the multistage high-sulfidation epithermal Pascua Au-Ag-Cu deposit, Chile and Argentina: Economic Geology, v. 100, p. 463-490

Collins A. C. (2010) Mineralogy and geochemistry of tourmaline in contrasting hydrothermal systems: Copiapo area, Northern Chile: MS thesis, The University of Arizona

Dill, H. G., Garrido, M. M., Melcher, F., Gomez, M. C., and Luna, L. I. (2012) Depth-related variation of tourmaline in the breccia pipe of the San Jorge porphyry copper deposit, Mendoza, Argentina: Ore Geology Reviews, v. 48, p. 271-277

Dutrow, B. L., and Henry, D. J. (2000) Complexly zoned fibrous tourmaline, Cruzeiro mine, Minas Gerais, Brazil: a record of evolving magmatic and hydrothermal fluids: The Canadian Mineralogist, v. 38, p. 131-143

Ellis, A. J., and Mahon, W. A. J. (1977) Chemistry and geothermal systems: Academic Press, p. 392

Fournier, R. O. (1985) The behavior of silica in hydrothermal solutions, in Geology and Geochemistry of Epithermal Systems, Berger, B. R., and Bethke, P. M. (eds): Reviews in Economic Geology, v. 2, p. 45-62

Grice J. D., and Ercit, T. S. (1993) Ordering of Fe and Mg in the tourmaline crystal structure: the correct formula: Neues Jahrbuch fuer Mineralogie Abhandlungen, v. 165, p. 245-266

Gupta, S., Jayananda, M., and Fareeduddin (2014) Tourmaline from the Archean G.R. Halli gold deposit, Chitradurga greenstone belt, Dharwar craton (India): implication for the gold metallogeny: Geoscience Frontiers, v. 5, p. 877-892

Hawthorne, F. C., and Henry, D. J. (1999) Classification of the minerals of the tourmaline group: European Journal of Mineralogy, v. 11, p. 201-215

Henry, D. J., and Dutrow, B. L. (1996) Metamorphic tourmaline and its petrologic applications, in Boron Mineralogy, Petrology and Geochemistry, E. S. Grew and L. M. Anovitz (eds): Reviews in Mineralogy, v. 33, 503-557

Henry, D. J., and Dutrow, B. L. (2011) The incorporation of fluorine in tourmaline: internal crystallographic controls or external environmental influences?, The Canadian Mineralogist, v. 49, p. 41-56

Henry, D. J., and Dutrow, B. L. (2012) Tourmaline at digenetic to low-grade metamorphic conditions: its petrologic applicability: Lithos, v. 154, p. 16-32

Henry, D. J., and Guidotti, C. V. (1985) Tourmaline as a petrogenetic indicator mineral: an example from the staurolite-grade meapelites of NW Maine: American Mineralogist, v. 70, p. 1-15

Henry, D. J., Novak, M. Hawthorne, F. C., Ertl, A. Dutrow, B. L., Uher, P., and Pezzotta, F. (2011) Nomenclature of the tourmaline-supergroup minerals: American Mineralogist, v. 96, p. 895-913

Herdianita, N. R., Browne, P. R. L., and Rodgers, K. A. (2001) Styles of hydrothermal alteration in the Darajat geothermal field, West Java, Indonesia: a progress report: Proceeding 23rd NZ Geothermal Workshop, p. 119-124

Jiang, S. Y., Radvanec, M., Nakamura, E., Palmer, M., Kobayashi, K., Zhao, H. X., and Zhao K. D. (2008) Chemical and boron isotopic variations of tourmaline in the Hnilec granite-related hydrothermal system, Slovakia: constraints on magmatic and metamorphic fluid evolution: Lithos, v. 106, p. 1-11

London, D., and Manning, D. (1995) Chemical variation and significance of tourmaline from Southwest England: Economic Geology, v. 90, p. 495-519

Moore, J. N., Allis, R. G., Nemcok, M., Powell, T. S., Bruton, C. J., Wannamaker, P. E., Raharjo, I. B., and Norman, D. I. (2008) The evolution of volcano-hosted geothermal systems based on deep wells from Karaha – Telaga Bodas, Indonesia: American Journal of Science, v. 308, p. 1-48

Moore, J. N., Bruton, C., and Powell, T. (2004a,) Wairakite: a potential indicator of fluid mixing: Geothermal Resources Council Transactions, v. 28, p. 495-498

Moore, J. N., Christenson, B. W., Allis, R. G., Browne, P. R. L., and Lutz, S. J., 2004b, The mineralogical consequences and behavior of descending acid-sulfate waters: an example from the Karaha – Telaga Bodas geothermal system, Indonesia: The Canadian Mineralogist, v. 42, p. 1483-1499

Moore, J. N., and Gunderson, R. P. (1995) Fluid inclusion and isotopic systematics of an evolving magmatic-hydrothermal system: Geochimica et Cosmochimica Acta, v. 59, p. 3887-3907

Morgan, G. B., and London, D. (1989) Experimental reactions of amphibolite with boron-bearing aqueous fluids at 200 MPa: implications for tourmaline stability and partial melting in mafic rocks: Contributions to Mineralogy and Petrology, v. 102, p. 281-297

Pal, D. C., Trumbull, R. B., and Wiedenbeck, M. (2010) Chemical and boron isotope compositions of tourmaline from the Jaduguda U (-Cu-Fe) deposit, Singhbhum shear zone, India: implications for the sources and evolution of mineralizing fluids: Chemical Geology, v. 277, p. 245-260

Rejeki, S., Rohrs, D., Nordquist, G., and Fitriyanto, A. (2010) Geologic conceptual model update of the Darajat geothermal field, Indonesia: Proceedings World Geothermal Congress, p. 1-6

Trumbull, R. B., and Chaussidon, M. (1999) Chemical and boron isotopic composition of magmatic and hydrothermal tourmalines from the Sinceni granite-pegmatite syste in Swaziland: Chemical Geology, v. 153, p. 125-137

van Hinsberg, V. J., Henry, D. J., and Marschall, H. R. (2011) Tourmaline: an ideal indicator of its host environment: The Canadian Mineralogist, v. 49, p. 1-16

von Goerne, G., Franz, G., and Heinrich, W. (2001) Synthesis of tourmaline solid solutions in the system $Na_2O$ – MgO - $Al_2O_3$ – $SiO_2$ – $B_2O_3$ – $H_2O$ – HCl and the distribution of Na between tourmaline and fluid at 300 to 700$^{o}$C and 200 MPa, Contributions to Mineralogy and Petrology, v. 141, p. 160-173

von Goerne, G., Franz, G., and van Hinsberg, V. J. (2011) Experimental determination of Na-Ca distrubtion between tourmaline and fluid in the system CaO-$Na_2O$-MgO-$Al_2O_3$-$SiO_2$-$B_2O_3$-$H_2O$: The Canadian Mineralogist, v. 49, p. 137-152

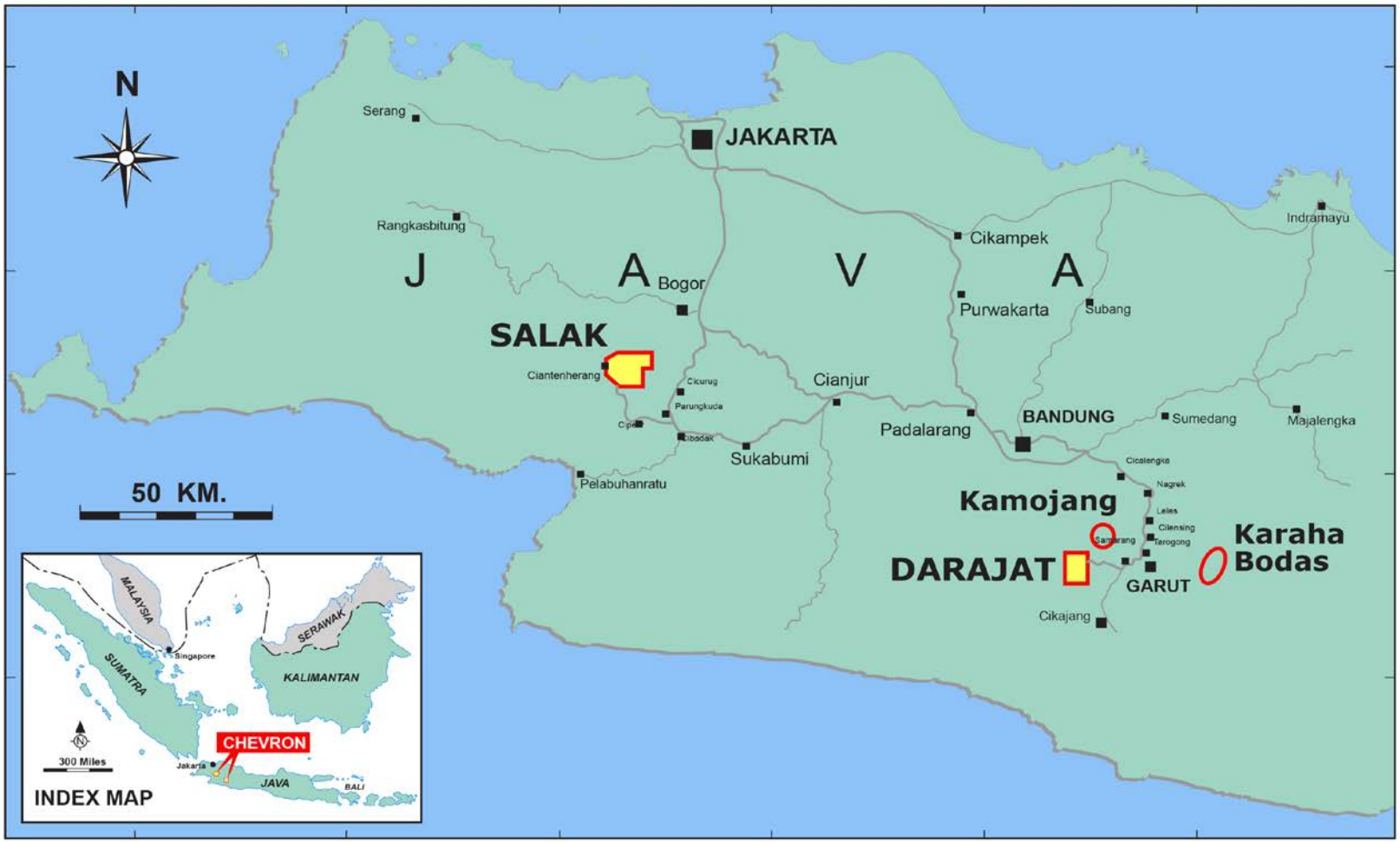


Figure 2.1: Simplified location map of Darajat. Darajat and Salak, highlighted in yellow, are owned and operated by Chevron Geothermal Indonesia. Karaha-Bodas is circled in red. Figure provided by Chevron Geothermal Indonesia, Ltd.

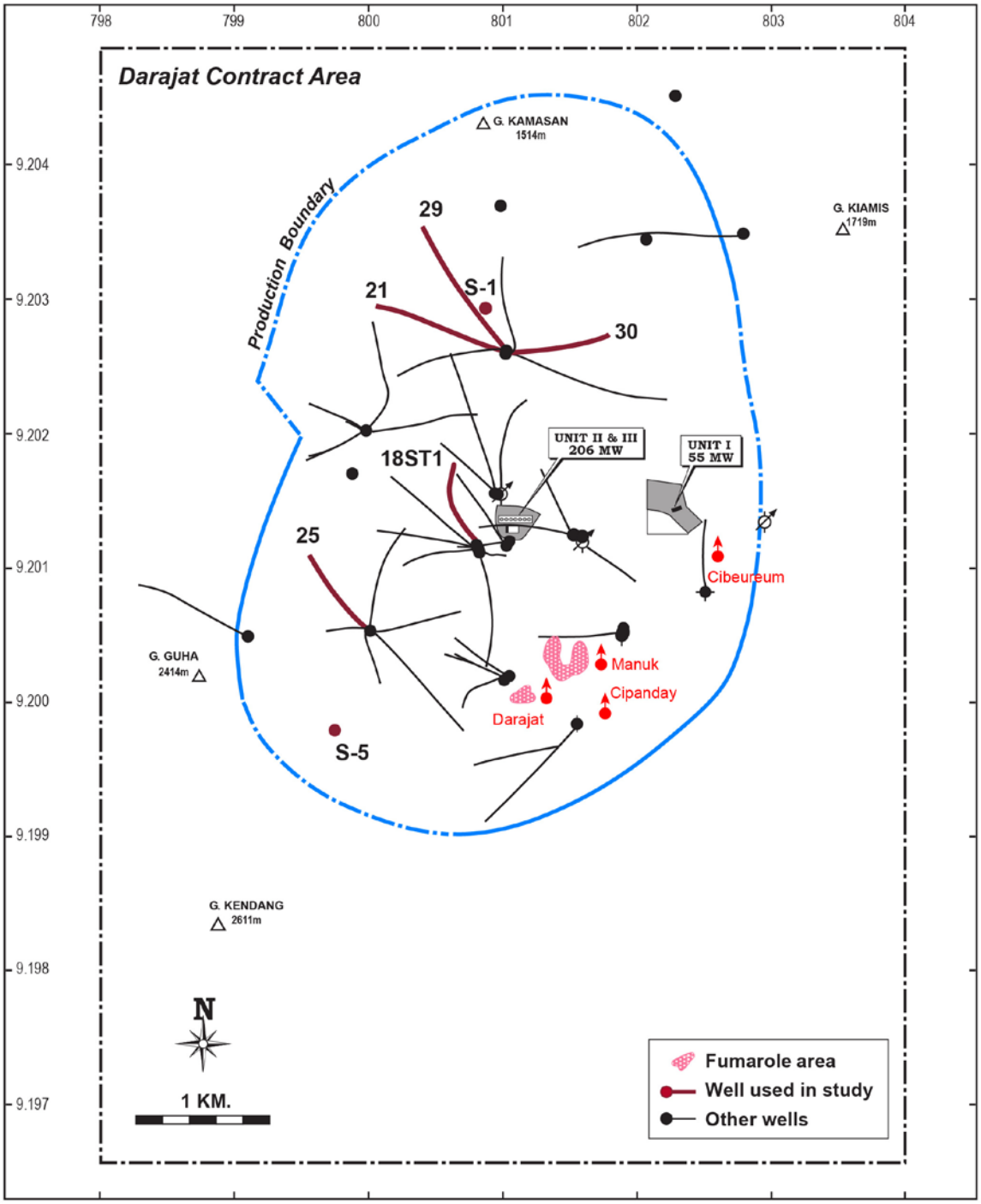


Figure 2.2: Location map of wells from Darajat used in this study. The solid lines are well trace projections from the surface to the bottom of each hole.

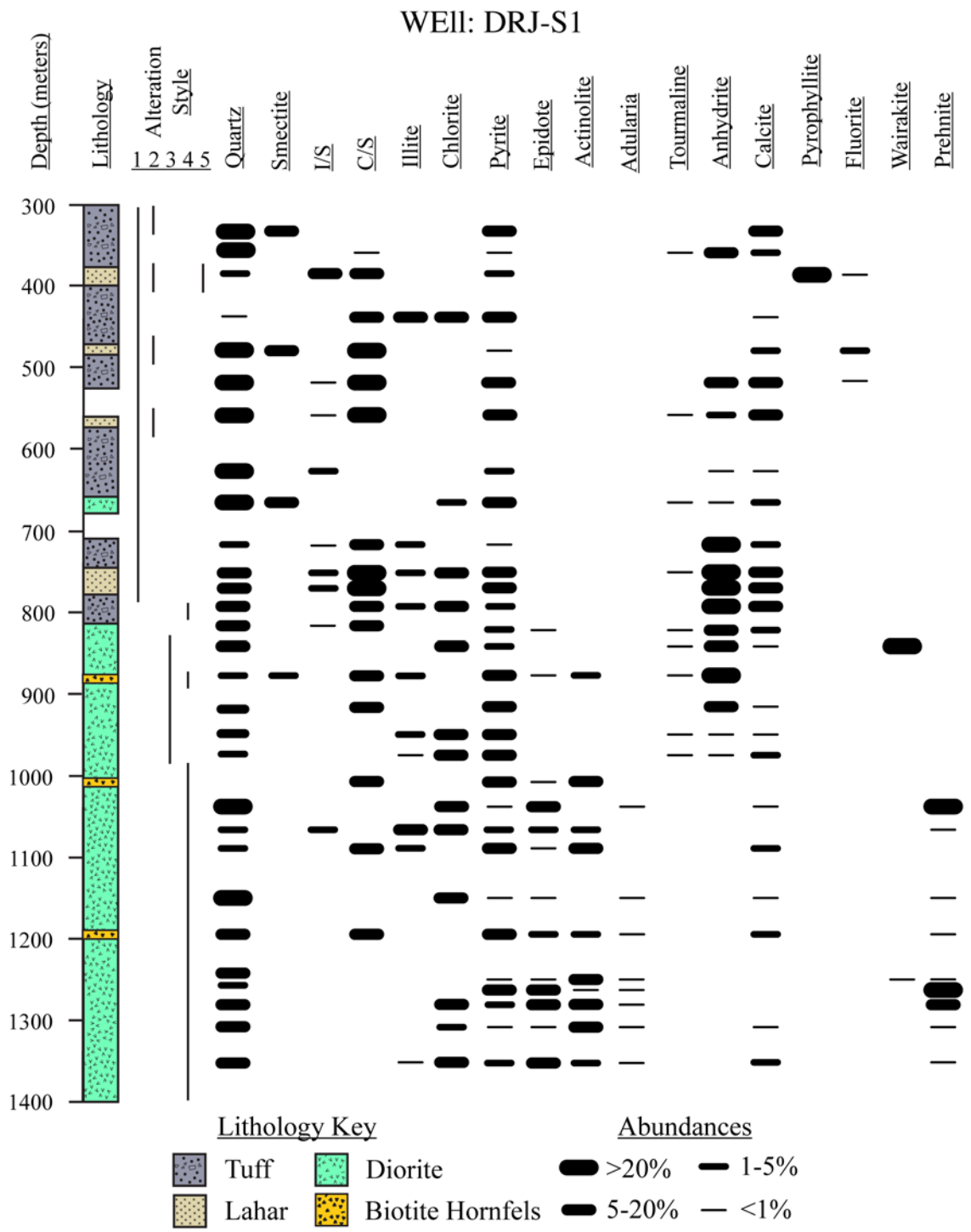


Figure 2.3: Overview of lithology in well DRJ-S1 based on petrographic observations and whole-rock XRD. Alteration styles are as follows: 1 = argillic, 2 = silicic, 3 = phyllic, 4 = propylitic and 5 = advanced argillic. I/S = interlayered illite-smectite, C/S = interlayered chlorite-smectite Horizontal bars indicate the mineral has been observed at that interval; thickness of bar indicates mineral abundance. Depth is in meters from the surface.

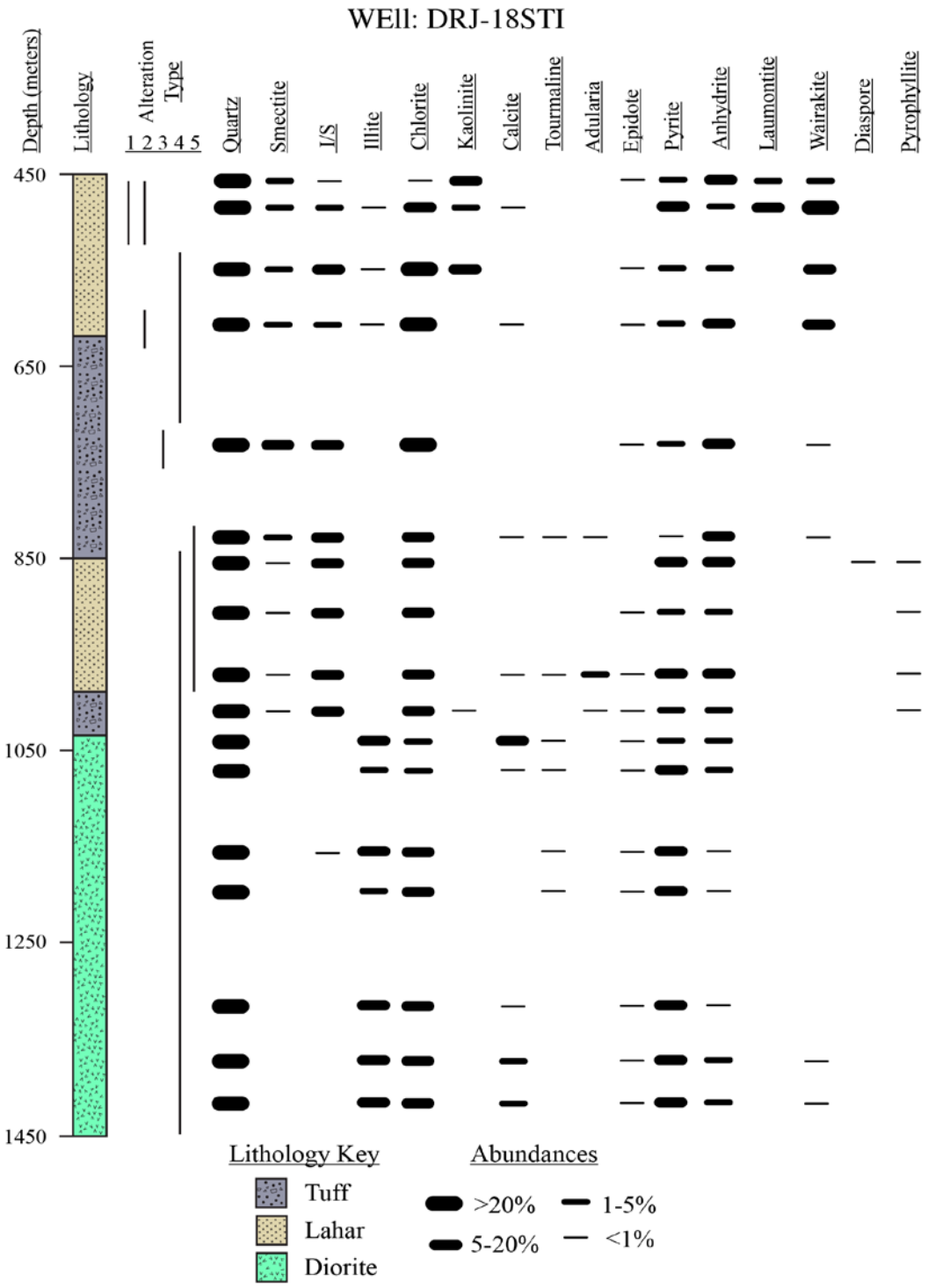


Figure 2.4: Overview of lithology in well DRJ-18ST1 based on petrographic observations and whole-rock XRD. Alteration styles are as follows: 1 = argillic, 2 = silicic, 3 = phyllic, 4 = propylitic and 5 = advanced argillic. I/S = interlayered illite-smectite, C/S = interlayered chlorite-smectite Horizontal bars indicate the mineral has been observed at that interval; thickness of bar indicates mineral abundance. Depth is in meters from the surface.

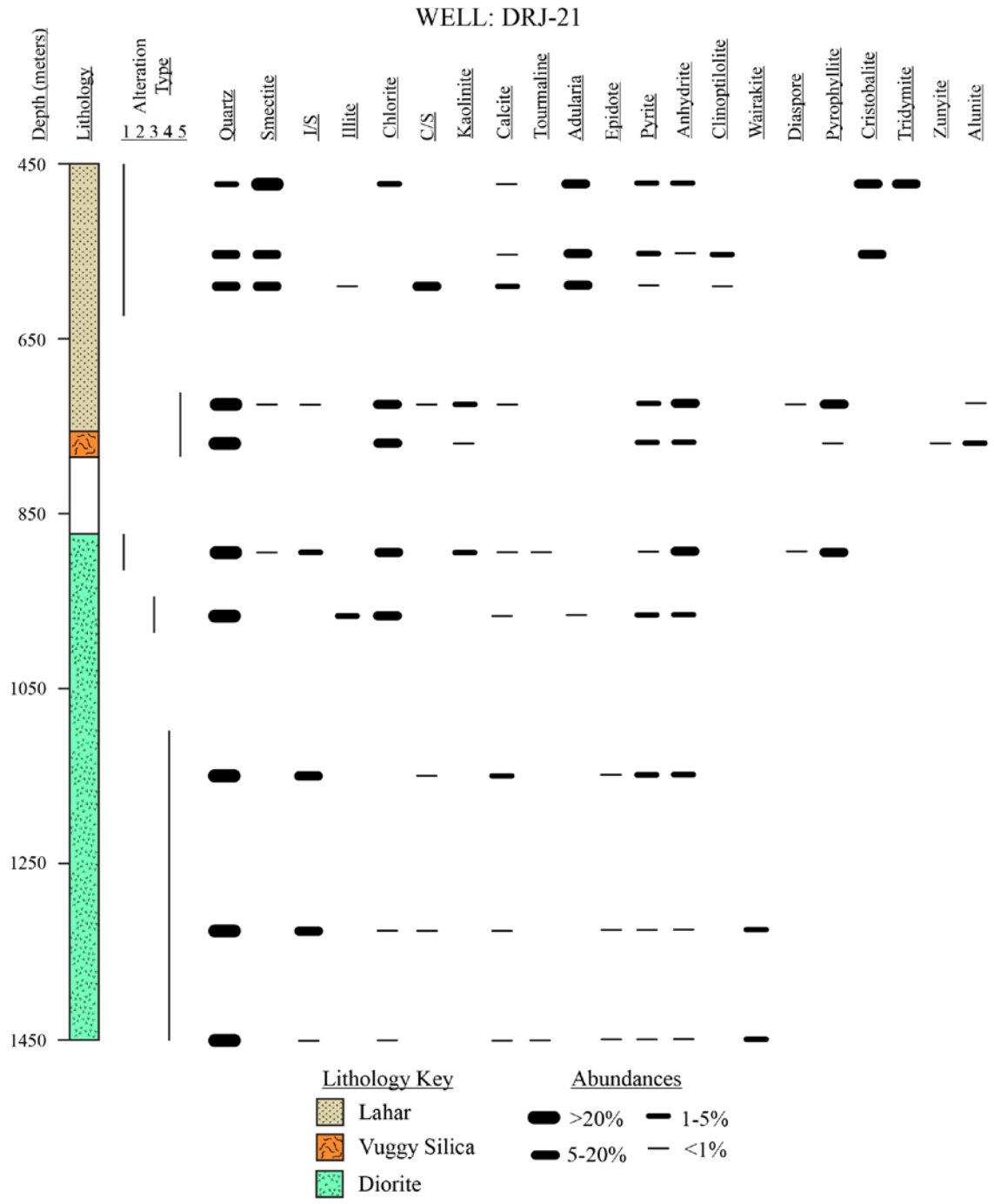


Figure 2.5: Overview of lithology in well DRJ-21 based on petrographic observations and whole-rock XRD. Alteration styles are as follows: 1 = argillic, 2 = silicic, 3 = phyllic, 4 = propylitic and 5 = advanced argillic. I/S = interlayered illite-smectite, C/S = interlayered chlorite-smectite Horizontal bars indicate the mineral has been observed at that interval; thickness of bar indicates mineral abundance. Depth is in meters from the surface.

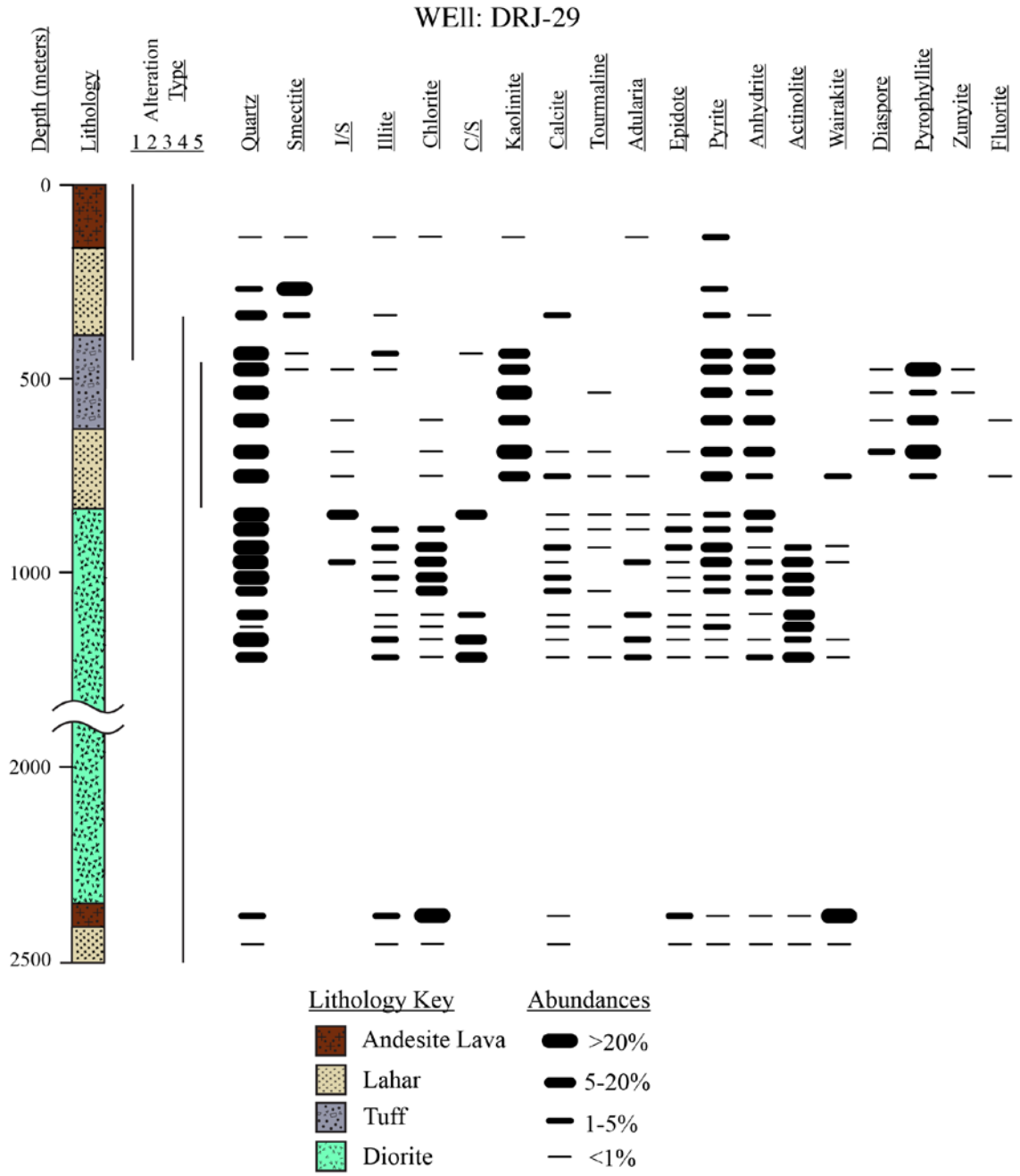


Figure 2.6: Overview of lithology in well DRJ-29 based on petrographic observations and whole-rock XRD. Alteration styles are as follows: 1 = argillic, 2 = silicic, 3 = phyllic, 4 = propylitic and 5 = advanced argillic. I/S = interlayered illite-smectite, C/S = interlayered chlorite-smectite Horizontal bars indicate the mineral has been observed at that interval; thickness of bar indicates mineral abundance. Depth is in meters from the surface.

Table 2.1: Summary of mineral assemblages in the Darajat system. Modified from Moore (unpub., 2007).

| Stage | Process | Alteration Type | Mineralogy |
|---|---|---|---|
| 1 | Upwelling of high temperature NaCl fluids; liquid-dominated | Shallow: argillic-phyllic alteration<br>Deep: propylitic | Shallow: smectite, I/S, illite<br>Deep: epidote, chlorite, actinolite, biotite, tourmaline |
| 2 | Boiling; conversion to vapor-dominated conditions | Silicification | Chalcedony, quartz |
| 3 | Descent and neutralization of steam condensates | Shallow: advanced argillic; sealing of marginal fractures | Shallow: pyrophyllite, diaspore, anhydrite, calcite, tourmaline<br>Deep: Wairakite |
| 4 | Surficial oxidation of $H_2S$ | Advanced argillic alteration | Alunite, kaolinite |

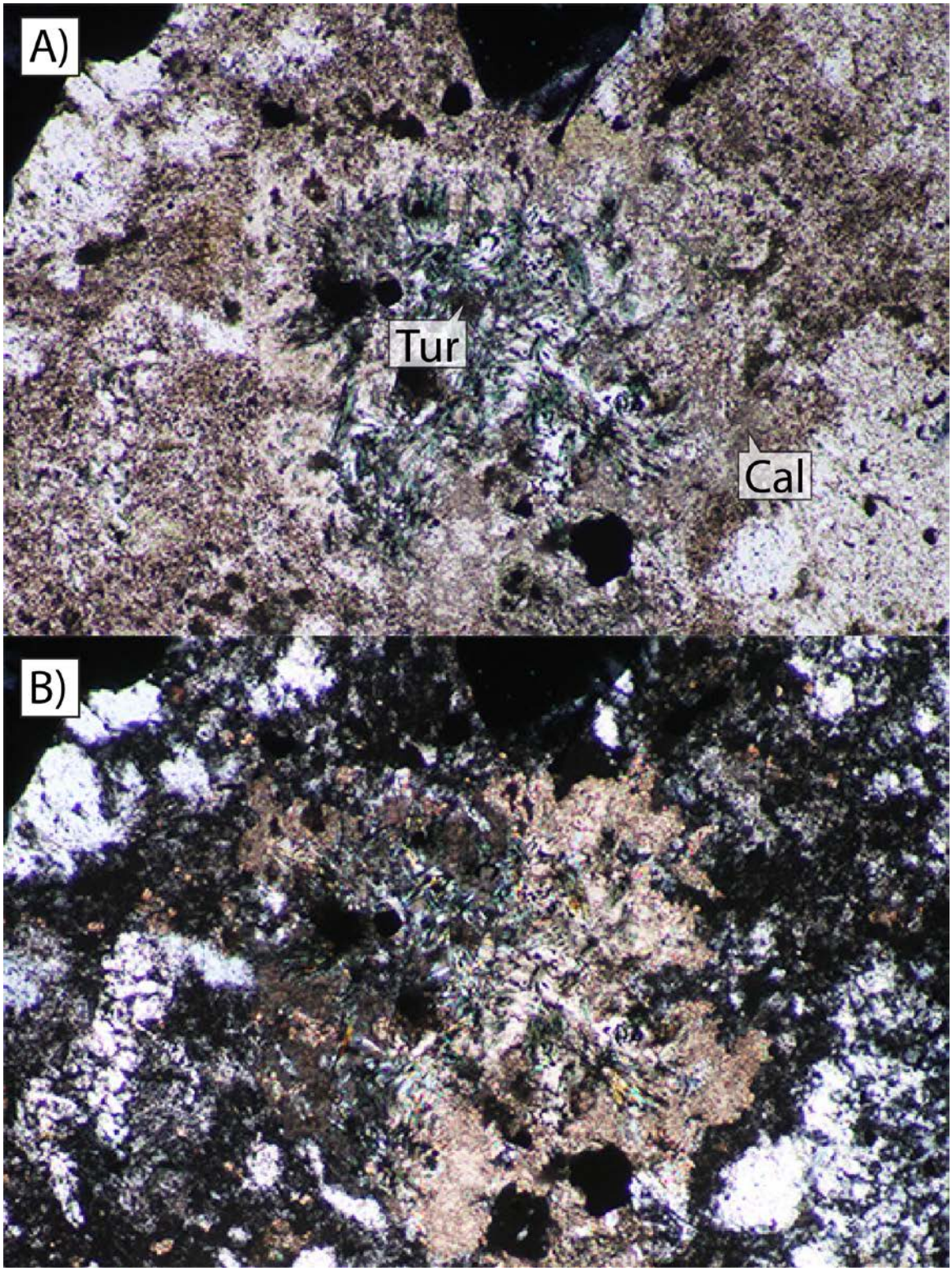


Figure 2.7: Representative photomicrograph of Stage 1 tourmalines (Tur) replacing plagioclase. Calcite (Cal) is also replacing plagioclase. A) Plane polarized light. B) Crossed nicols. The field of view is 2.2 mm.

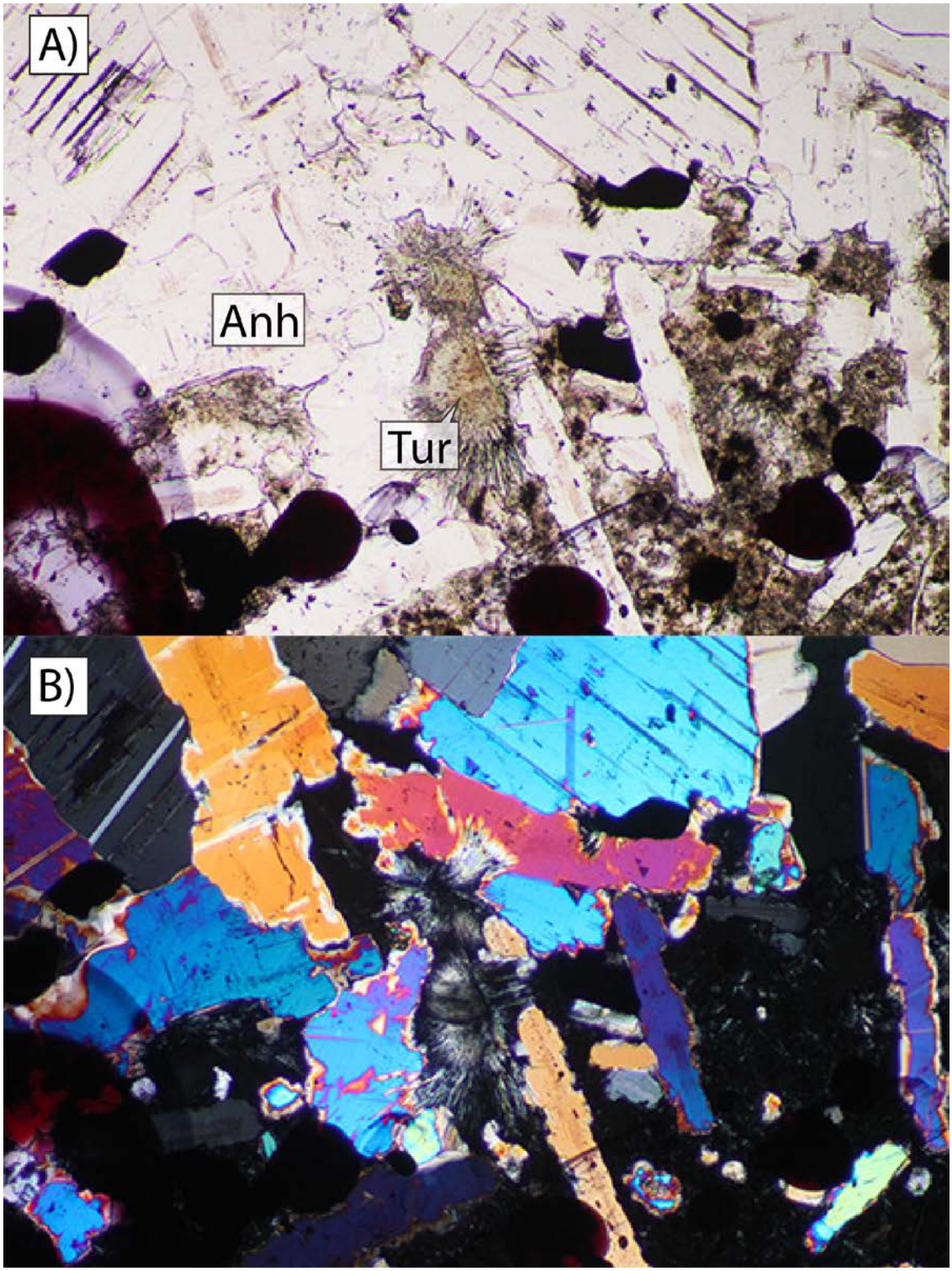


Figure 2.8: Representative photomicrograph of Stage 3 tourmalines (Tur) within an anhydrite (Anh) vein. A) Plane polarized light. B) Crossed nicols. The field of view is 2.2 mm.

Table 2.2: Representative electron microprobe analyses (wt %) of Darajat tourmalines. Sample depths 975.4 m and 807.7 m are Stage 1; 821.4 m and 670.1 m are Stage 3.

| Sample | 670.1 | 670.1 | 670.1 | 670.1 | 670.1 | 670.1 | 670.1 | 670.1 | 670.1 | 670.1 |
|---|---|---|---|---|---|---|---|---|---|---|
| Spot ID | 1_1 | 1_2 | 1_3 | 1_4 | 1_5 | 2_1 | 2_2 | 2_3 | 2_4 | 2_5 |
| *Wt %* | | | | | | | | | | |
| $B_2O_3$ | 10.19 | 10.14 | 10.24 | 10.17 | 10.16 | 10.24 | 10.15 | 10.53 | 10.12 | 9.83 |
| $SiO_2$ | 37.83 | 37.95 | 38.12 | 37.92 | 38.31 | 36.46 | 37.31 | 36.79 | 35.03 | 34.07 |
| $Al_2O_3$ | 32.16 | 31.79 | 31.68 | 31.59 | 31.44 | 33.07 | 32.27 | 30.37 | 28.63 | 27.63 |
| $TiO_2$ | 0.14 | 0.08 | 0.33 | 0.06 | 0.06 | 0.24 | 0.58 | 0.10 | 0.00 | 0.19 |
| FeO | 3.42 | 3.43 | 3.52 | 3.28 | 3.54 | 3.78 | 3.21 | 6.26 | 6.11 | 5.72 |
| MnO | 0.09 | 0.13 | 0.19 | 0.11 | 0.12 | 0.03 | 0.12 | 0.24 | 0.30 | 0.39 |
| MgO | 6.16 | 6.07 | 6.41 | 6.56 | 6.19 | 6.45 | 6.06 | 8.57 | 8.95 | 8.69 |
| CaO | 1.25 | 1.36 | 1.18 | 1.19 | 1.30 | 1.27 | 1.35 | 0.89 | 1.03 | 3.74 |
| $Na_2O$ | 1.14 | 1.18 | 1.10 | 0.98 | 0.97 | 1.21 | 1.20 | 0.96 | 0.72 | 0.72 |
| $K_2O$ | 0.40 | 0.51 | 0.89 | 0.48 | 0.85 | 0.06 | 0.31 | 0.19 | 0.50 | 0.88 |
| F | 0.29 | 0.44 | 0.37 | 0.36 | 0.17 | 0.32 | 0.09 | 0.65 | 0.43 | 0.79 |
| Cl | 0.15 | 0.00 | 0.04 | 0.04 | 0.11 | 0.00 | 0.01 | 0.00 | 0.08 | 0.07 |
| Total | 93.23 | 93.07 | 94.06 | 92.74 | 93.22 | 93.11 | 92.65 | 95.52 | 91.80 | 92.70 |
| O = F,Cl | 0.16 | 0.18 | 0.16 | 0.16 | 0.10 | 0.13 | 0.04 | 0.27 | 0.20 | 0.35 |
| Total | 93.07 | 92.89 | 93.90 | 92.58 | 93.12 | 92.98 | 92.61 | 95.20 | 91.60 | 92.35 |
| *apfu* | | | | | | | | | | |
| B | 3.00 | 3.00 | 3.00 | 3.00 | 3.00 | 3.00 | 3.00 | 3.00 | 3.00 | 3.00 |
| Si | 6.450 | 6.51 | 6.47 | 6.47 | 6.55 | 6.18 | 6.39 | 6.07 | 6.01 | 6.02 |
| $^{T}Al$ | 0.000 | 0.00 | 0.00 | 0.00 | 0.00 | 0.00 | 0.00 | 0.00 | 0.00 | 0.00 |
| $^{Z}Al$ | 6.000 | 6.00 | 6.00 | 6.00 | 6.00 | 6.00 | 6.00 | 5.91 | 5.79 | 5.76 |
| $^{Y}Al$ | 0.464 | 0.42 | 0.34 | 0.36 | 0.34 | 0.61 | 0.52 | 0.00 | 0.00 | 0.00 |
| Ti | 0.018 | 0.01 | 0.04 | 0.01 | 0.01 | 0.03 | 0.07 | 0.01 | 0.00 | 0.03 |
| $Fe^{2+}$ | 0.488 | 0.49 | 0.50 | 0.47 | 0.51 | 0.53 | 0.46 | 0.86 | 0.88 | 0.84 |
| Mn | 0.014 | 0.02 | 0.03 | 0.02 | 0.02 | 0.00 | 0.02 | 0.03 | 0.04 | 0.06 |
| Mg | 1.566 | 1.55 | 1.62 | 1.67 | 1.58 | 1.63 | 1.55 | 2.11 | 2.29 | 2.29 |
| Ca | 0.229 | 0.25 | 0.21 | 0.22 | 0.24 | 0.23 | 0.25 | 0.16 | 0.19 | 0.71 |
| Na | 0.376 | 0.39 | 0.36 | 0.32 | 0.32 | 0.40 | 0.40 | 0.31 | 0.24 | 0.25 |
| K | 0.087 | 0.11 | 0.19 | 0.22 | 0.24 | 0.01 | 0.07 | 0.04 | 0.11 | 0.20 |
| $^{X}\square$ | 0.308 | 0.25 | 0.23 | 0.36 | 0.26 | 0.36 | 0.29 | 0.50 | 0.46 | 0.00 |
| F | 0.158 | 0.24 | 0.20 | 0.19 | 0.09 | 0.17 | 0.05 | 0.34 | 0.23 | 0.44 |
| Cl | 0.044 | 0.00 | 0.01 | 0.01 | 0.03 | 0.00 | 0.00 | 0.00 | 0.02 | 0.02 |
| OH | 3.266 | 3.26 | 3.26 | 3.27 | 3.29 | 3.28 | 3.32 | 3.22 | 3.25 | 3.18 |
| O | 0.532 | 0.51 | 0.53 | 0.53 | 0.58 | 0.55 | 0.63 | 0.45 | 0.50 | 0.36 |

Table 2.2 (continued):

| Sample | 670.1 | 670.1 | 670.1 | 670.1 | 670.1 | 670.1 | 670.1 | 807.7 | 807.7 | 807.7 |
|---|---|---|---|---|---|---|---|---|---|---|
| Spot ID | 3_1 | 3_2 | 3_3 | 4_1 | 4_2 | 4_3 | 4_4 | 1_1 | 1_2 | 1_3 |
| *Wt %* | | | | | | | | | | |
| $B_2O_3$ | 10.21 | 9.38 | 9.99 | 10.40 | 10.47 | 10.27 | 9.77 | 10.49 | 10.43 | 10.83 |
| $SiO_2$ | 35.62 | 33.14 | 36.65 | 38.29 | 46.57 | 37.54 | 31.35 | 36.46 | 36.05 | 40.98 |
| $Al_2O_3$ | 33.16 | 30.23 | 30.22 | 30.58 | 27.18 | 32.10 | 26.63 | 32.84 | 34.13 | 26.55 |
| $TiO_2$ | 0.00 | 0.09 | 0.16 | 0.25 | 0.01 | 0.33 | 8.44 | 0.19 | 0.23 | 0.08 |
| FeO | 4.81 | 3.97 | 4.11 | 4.80 | 4.09 | 4.34 | 5.22 | 7.33 | 6.35 | 9.86 |
| MnO | 0.16 | 0.24 | 0.24 | 0.17 | 0.11 | 0.05 | 0.22 | 0.11 | 0.14 | 0.61 |
| MgO | 6.19 | 5.79 | 6.83 | 7.41 | 5.54 | 6.25 | 7.16 | 6.01 | 5.47 | 8.28 |
| CaO | 1.10 | 6.10 | 2.44 | 0.97 | 0.91 | 1.18 | 1.22 | 0.74 | 1.02 | 0.09 |
| $Na_2O$ | 1.29 | 1.21 | 0.87 | 0.84 | 0.93 | 1.24 | 0.79 | 1.42 | 1.23 | 0.19 |
| $K_2O$ | 0.10 | 0.25 | 0.98 | 0.73 | 0.49 | 0.11 | 0.42 | 0.03 | 0.13 | 3.57 |
| F | 0.40 | 0.08 | 0.31 | 0.32 | 0.15 | 0.38 | 0.25 | 0.00 | 0.00 | 0.03 |
| Cl | 0.14 | 0.06 | 0.01 | 0.06 | -0.01 | 0.03 | 0.10 | 0.11 | 0.15 | 0.33 |
| Total | 93.17 | 90.54 | 92.81 | 94.81 | 96.40 | 93.81 | 91.59 | 95.72 | 95.26 | 101.42 |
| O = F,Cl | 0.19 | 0.05 | 0.13 | 0.15 | 0.06 | 0.17 | 0.13 | 0.02 | 0.01 | 0.08 |
| Total | 92.98 | 90.49 | 92.68 | 94.66 | 96.34 | 93.64 | 91.46 | 95.70 | 95.25 | 101.34 |
| *apfu* | | | | | | | | | | |
| B | 3.00 | 3.00 | 3.00 | 3.00 | 3.00 | 3.00 | 3.00 | 3.00 | 3.00 | 3.00 |
| Si | 6.07 | 6.14 | 6.38 | 6.40 | 7.73 | 6.36 | 5.58 | 6.04 | 6.006 | 6.58 |
| $^{T}Al$ | 0.00 | 0.00 | 0.00 | 0.00 | 0.00 | 0.00 | 0.42 | 0.00 | 0.00 | 0.00 |
| $^{Z}Al$ | 6.00 | 6.00 | 6.00 | 6.00 | 5.32 | 6.00 | 5.58 | 6.00 | 6.00 | 5.02 |
| $^{Y}Al$ | 0.66 | 0.60 | 0.20 | 0.03 | 0.00 | 0.41 | 0.00 | 0.42 | 0.70 | 0.00 |
| Ti | 0.00 | 0.01 | 0.02 | 0.03 | 0.00 | 0.04 | 1.13 | 0.02 | 0.03 | 0.01 |
| $Fe^{2+}$ | 0.69 | 0.62 | 0.60 | 0.67 | 0.57 | 0.61 | 0.78 | 1.02 | 0.88 | 1.32 |
| Mn | 0.02 | 0.04 | 0.04 | 0.02 | 0.02 | 0.01 | 0.03 | 0.02 | 0.02 | 0.08 |
| Mg | 1.57 | 1.60 | 1.77 | 1.85 | 1.37 | 1.58 | 1.90 | 1.49 | 1.36 | 1.98 |
| Ca | 0.20 | 1.21 | 0.46 | 0.17 | 0.16 | 0.21 | 0.23 | 0.13 | 0.18 | 0.02 |
| Na | 0.43 | 0.43 | 0.29 | 0.27 | 0.30 | 0.41 | 0.27 | 0.46 | 0.40 | 0.06 |
| K | 0.02 | 0.06 | 0.22 | 0.17 | 0.11 | 0.02 | 0.10 | 0.01 | 0.03 | 0.73 |
| $^{X}\square$ | 0.35 | 0.00 | 0.03 | 0.40 | 0.43 | 0.36 | 0.40 | 0.41 | 0.39 | 0.19 |
| F | 0.22 | 0.05 | 0.17 | 0.17 | 0.08 | 0.21 | 0.14 | 0.01 | 0.00 | 0.01 |
| Cl | 0.04 | 0.02 | 0.00 | 0.02 | 0.00 | 0.01 | 0.03 | 0.03 | 0.042 | 0.09 |
| OH | 3.25 | 3.31 | 3.28 | 3.27 | 3.31 | 3.26 | 3.28 | 3.32 | 3.330 | 3.30 |
| O | 0.50 | 0.62 | 0.55 | 0.54 | 0.62 | 0.52 | 0.55 | 0.65 | 0.66 | 0.60 |

Table 2.2 (continued):

| Sample | 807.7 | 807.7 | 821.4 | 821.4 | 821.4 | 821.4 | 821.4 | 821.4 | 821.4 | 975.4 |
|---|---|---|---|---|---|---|---|---|---|---|
| Spot ID | 2_1 | 2_2 | 1_5 | 1_6 | 1_10 | 1_16 | 2_1 | 2_2 | 2_4 | 1_7 |
| *Wt%* | | | | | | | | | | |
| $B_2O_3$ | 10.35 | 10.68 | 10.75 | 10.52 | 8.94 | 10.88 | 10.27 | 10.39 | 10.14 | 10.40 |
| $SiO_2$ | 35.99 | 36.42 | 37.46 | 41.71 | 35.11 | 40.97 | 36.12 | 36.29 | 35.57 | 36.11 |
| $Al_2O_3$ | 33.71 | 34.20 | 34.71 | 33.62 | 26.76 | 35.84 | 33.38 | 33.78 | 32.21 | 31.27 |
| $TiO_2$ | 0.00 | 0.19 | 0.50 | 0.20 | 0.20 | 0.33 | 0.18 | 0.03 | 0.16 | 0.28 |
| FeO | 6.30 | 6.25 | 2.79 | 1.38 | 1.82 | 1.80 | 3.36 | 3.78 | 3.84 | 9.97 |
| MnO | 0.08 | 0.09 | 0.01 | 0.05 | 0.01 | 0.04 | 0.11 | 0.05 | 0.06 | 0.13 |
| MgO | 5.71 | 6.70 | 7.82 | 5.47 | 5.97 | 6.01 | 6.98 | 6.94 | 7.11 | 5.46 |
| CaO | 0.89 | 0.95 | 1.16 | 2.70 | 1.02 | 2.58 | 1.88 | 1.81 | 1.31 | 1.02 |
| $Na_2O$ | 1.27 | 1.42 | 1.43 | 1.44 | 1.08 | 1.38 | 1.03 | 1.21 | 1.38 | 1.61 |
| $K_2O$ | 0.04 | 0.02 | 0.01 | 0.01 | 0.02 | 0.01 | 0.03 | 0.01 | 0.02 | 0.02 |
| F | 0.00 | 0.15 | 0.05 | 0.09 | 0.06 | 0.10 | 0.12 | 0.04 | 0.06 | 0.07 |
| Cl | 0.08 | 0.05 | 0.04 | 0.37 | 0.43 | 0.04 | 0.07 | 0.02 | 0.10 | 0.05 |
| Total | 93.90 | 96.82 | 96.71 | 97.57 | 81.30 | 99.97 | 92.94 | 94.27 | 91.95 | 96.26 |
| O = F,Cl | 0.04 | 0.05 | 0.03 | 0.12 | 0.07 | 0.05 | 0.03 | 0.01 | 0.05 | 0.68 |
| Total | 93.94 | 96.87 | 96.68 | 97.45 | 81.23 | 99.92 | 92.97 | 94.28 | 91.90 | 95.58 |
| *apfu* | | | | | | | | | | |
| B | 3.00 | 3.00 | 3.00 | 3.00 | 3.00 | 3.00 | 3.00 | 3.00 | 3.00 | 3.00 |
| Si | 6.05 | 5.93 | 6.06 | 6.89 | 6.82 | 6.54 | 6.11 | 6.07 | 6.10 | 6.03 |
| $^{T}Al$ | 0.00 | 0.07 | 0.00 | 0.00 | 0.00 | 0.00 | 0.00 | 0.00 | 0.00 | 0.00 |
| $^{Z}Al$ | 6.00 | 6.00 | 6.00 | 6.00 | 6.00 | 6.00 | 6.00 | 6.00 | 6.00 | 6.00 |
| $^{Y}Al$ | 0.67 | 0.49 | 0.62 | 0.54 | 0.13 | 0.74 | 0.66 | 0.66 | 0.51 | 0.16 |
| Ti | 0.04 | 0.02 | 0.06 | 0.02 | 0.03 | 0.04 | 0.00 | 0.00 | 0.02 | 0.04 |
| $Fe^{2+}$ | 0.89 | 0.85 | 0.38 | 0.19 | 0.30 | 0.24 | 0.48 | 0.53 | 0.55 | 1.39 |
| Mn | 0.01 | 0.01 | 0.00 | 0.01 | 0.00 | 0.01 | 0.02 | 0.01 | 0.01 | 0.02 |
| Mg | 1.43 | 1.63 | 1.89 | 1.35 | 1.73 | 1.43 | 1.76 | 1.73 | 1.82 | 1.36 |
| Ca | 0.16 | 0.17 | 0.20 | 0.48 | 0.21 | 0.44 | 0.34 | 0.32 | 0.24 | 0.18 |
| Na | 0.41 | 0.45 | 0.45 | 0.46 | 0.41 | 0.43 | 0.34 | 0.39 | 0.46 | 0.52 |
| K | 0.01 | 0.01 | 0.00 | 0.00 | 0.00 | 0.00 | 0.01 | 0.00 | 0.00 | 0.01 |
| $^{X}\square$ | 0.42 | 0.38 | 0.35 | 0.06 | 0.38 | 0.13 | 0.32 | 0.28 | 0.30 | 0.29 |
| F | 0.00 | 0.07 | 0.02 | 0.05 | 0.03 | 0.05 | 0.06 | 0.02 | 0.03 | 0.03 |
| Cl | 0.02 | 0.01 | 0.01 | 0.10 | 0.14 | 0.02 | 0.02 | 0.01 | 0.03 | 0.01 |
| OH | 3.35 | 3.35 | 3.32 | 3.28 | 3.30 | 3.31 | 3.35 | 3.34 | 3.31 | 3.34 |
| O | 0.71 | 0.71 | 0.64 | 0.57 | 0.60 | 0.63 | 0.70 | 0.68 | 0.63 | 0.68 |

Table 2.2 (continued):

| Sample | 975.4 | 975.4 | 975.4 | 975.4 | 975.4 | 975.4 | 975.4 | 975.4 | 975.4 |
|---|---|---|---|---|---|---|---|---|---|
| Spot ID | 1_9 | 1_10 | 5_1 | 5_2 | 5_3 | 5_4 | 5_5 | 7_5 | 7_6 |
| *Wt%* | | | | | | | | | |
| $B_2O_3$ | 10.37 | 9.19 | 10.40 | 10.48 | 10.29 | 10.33 | 9.93 | 11.05 | 10.42 |
| $SiO_2$ | 35.63 | 32.63 | 35.91 | 36.57 | 35.87 | 35.87 | 35.38 | 37.39 | 36.47 |
| $Al_2O_3$ | 30.59 | 22.83 | 31.93 | 31.14 | 31.32 | 31.37 | 29.46 | 34.34 | 30.46 |
| $TiO_2$ | 0.18 | 8.74 | 0.17 | 0.22 | 0.24 | 0.24 | 0.36 | 0.09 | 0.39 |
| FeO | 13.05 | 6.41 | 9.51 | 11.79 | 9.77 | 9.99 | 10.14 | 8.81 | 10.37 |
| MnO | 0.12 | 0.05 | 0.12 | 0.24 | 0.12 | 0.12 | 0.17 | 0.11 | 0.09 |
| MgO | 4.48 | 5.21 | 5.39 | 4.68 | 5.09 | 5.20 | 4.54 | 6.70 | 5.72 |
| CaO | 0.61 | 9.95 | 1.01 | 0.74 | 1.04 | 1.07 | 0.84 | 1.50 | 1.09 |
| $Na_2O$ | 1.83 | 1.22 | 1.49 | 1.63 | 1.46 | 1.38 | 1.51 | 2.15 | 1.80 |
| $K_2O$ | 0.03 | 0.00 | 0.03 | 0.03 | 0.05 | 0.03 | 0.06 | 0.02 | 0.01 |
| F | 0.00 | 0.01 | 0.01 | 0.00 | 0.03 | 0.04 | 0.00 | 0.00 | 0.03 |
| Cl | 0.02 | 0.12 | 0.09 | 0.12 | 0.02 | 0.07 | 0.10 | 0.08 | 0.01 |
| Total | 95.00 | 96.37 | 96.07 | 97.55 | 95.27 | 95.57 | 92.37 | 102.05 | 96.87 |
| O = F,Cl | 0.03 | 0.03 | 0.03 | 0.01 | 0.01 | 0.00 | 0.02 | 0.02 | 0.02 |
| Total | 95.03 | 96.34 | 96.04 | 97.56 | 95.26 | 95.57 | 92.39 | 102.07 | 96.85 |
| *apfu* | | | | | | | | | |
| B | 3.00 | 3.00 | 3.00 | 3.00 | 3.00 | 3.00 | 3.00 | 3.00 | 3.00 |
| Si | 5.97 | 6.17 | 6.00 | 6.06 | 6.06 | 6.03 | 6.19 | 5.88 | 6.08 |
| $^{T}Al$ | 0.03 | 0.00 | 0.00 | 0.00 | 0.00 | 0.00 | 0.00 | 0.11 | 0.00 |
| $^{Z}Al$ | 6.00 | 5.09 | 6.00 | 6.00 | 6.00 | 6.00 | 6.00 | 6.00 | 5.99 |
| $^{Y}Al$ | 0.01 | 0.00 | 0.29 | 0.09 | 0.23 | 0.22 | 0.07 | 0.25 | 0.00 |
| Ti | 0.02 | 1.24 | 0.02 | 0.03 | 0.03 | 0.03 | 0.05 | 0.01 | 0.05 |
| $Fe^{2+}$ | 1.83 | 1.02 | 1.33 | 1.64 | 1.38 | 1.41 | 1.48 | 1.16 | 1.45 |
| Mn | 0.02 | 0.01 | 0.02 | 0.03 | 0.02 | 0.02 | 0.03 | 0.02 | 0.01 |
| Mg | 1.12 | 1.47 | 1.34 | 1.16 | 1.28 | 1.30 | 1.18 | 1.57 | 1.42 |
| Ca | 0.11 | 2.02 | 0.18 | 0.13 | 0.19 | 0.19 | 0.16 | 0.25 | 0.20 |
| Na | 0.59 | 0.45 | 0.48 | 0.52 | 0.48 | 0.45 | 0.51 | 0.66 | 0.58 |
| K | 0.01 | 0.00 | 0.01 | 0.01 | 0.01 | 0.01 | 0.01 | 0.00 | 0.00 |
| $^{X}\square$ | 0.29 | 0.00 | 0.33 | 0.34 | 0.32 | 0.35 | 0.32 | 0.09 | 0.22 |
| F | -0.03 | 0.00 | 0.01 | -0.04 | 0.02 | 0.02 | -0.06 | -0.01 | 0.02 |
| Cl | -0.01 | 0.04 | 0.03 | 0.033 | -0.01 | -0.02 | 0.03 | -0.02 | 0.00 |
| OH | 3.34 | 3.32 | 3.32 | 3.34 | 3.33 | 3.33 | 3.34 | 3.34 | 3.33 |
| O | 0.69 | 0.64 | 0.65 | 0.67 | 0.66 | 0.67 | 0.69 | 0.69 | 0.65 |

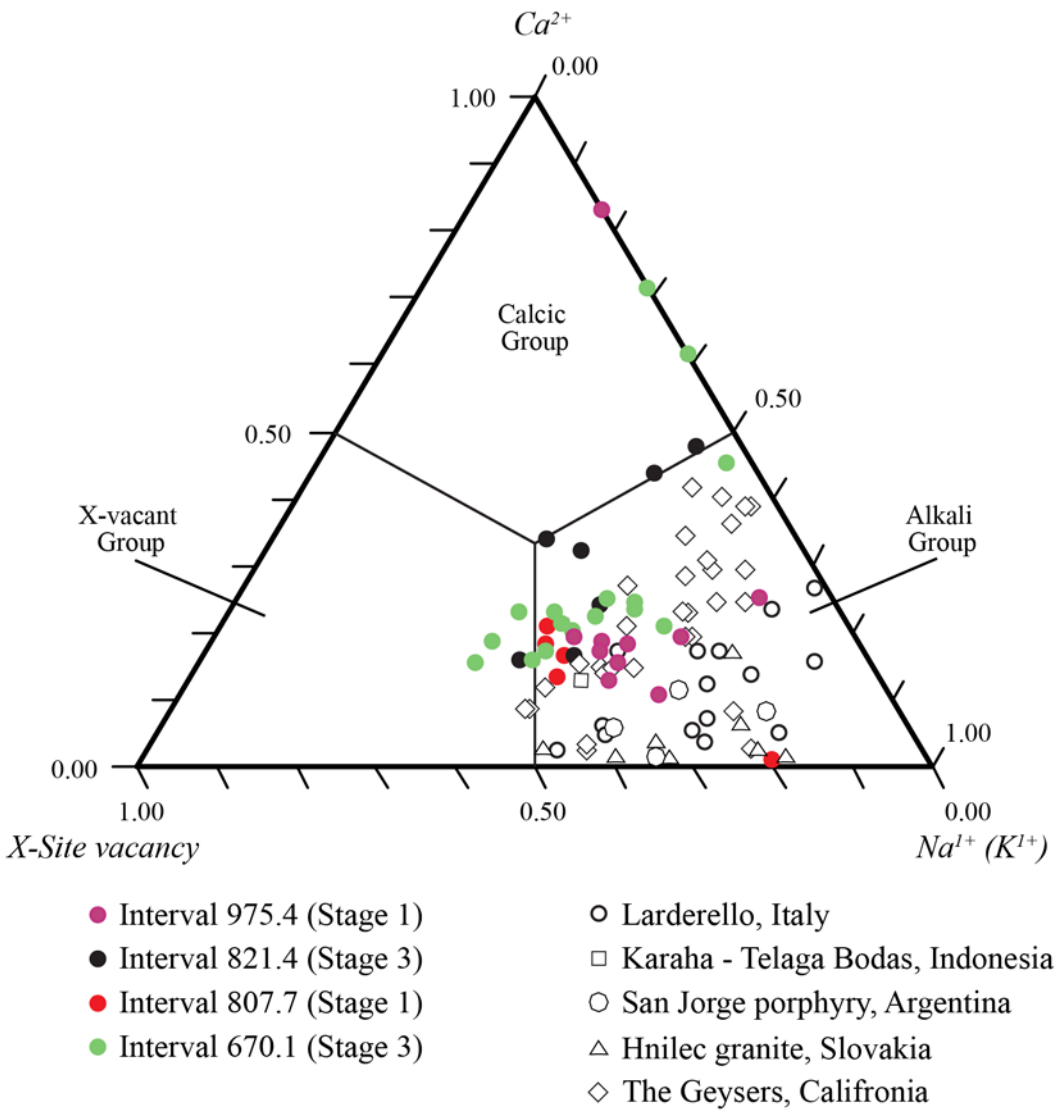


Figure 2.9: General chemical composition diagram based on alkali content (Hawthorne and Henry, 1999) of tourmaline. Circular symbols represent individual analyses of a sample from the Darajat system. The open symbols represent data from other sites.

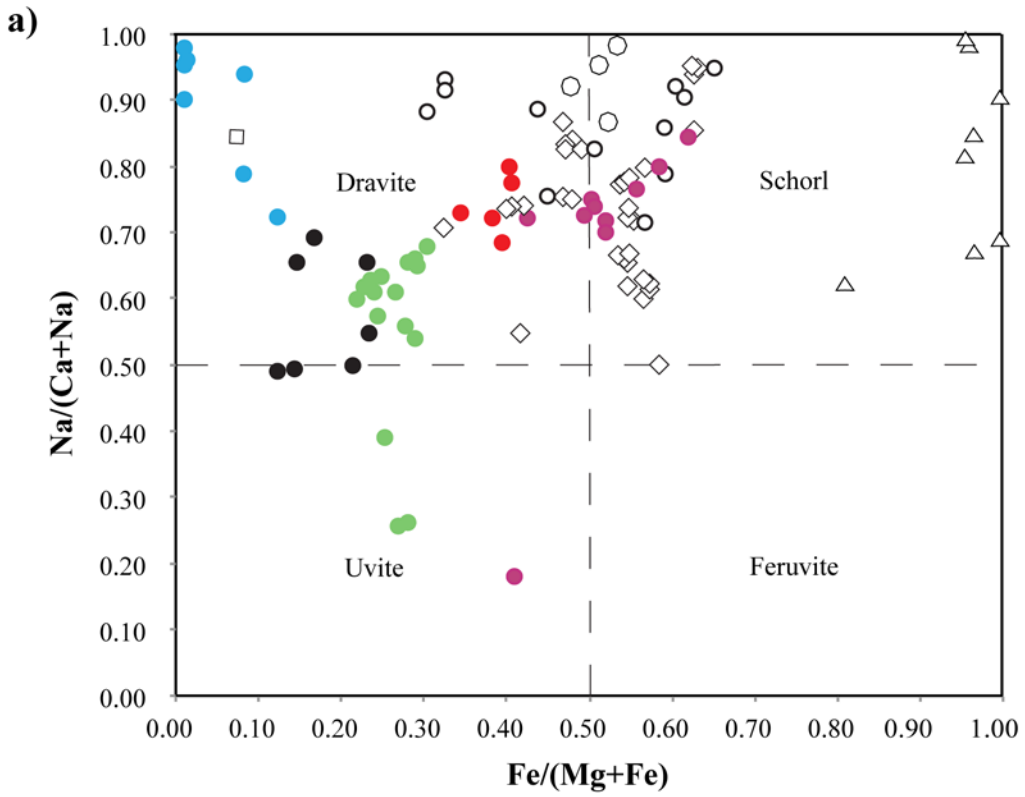


Figure 2.10: Compositional diagrams constructed to further classify tourmalines into accepted categories and depict possible exchange vectors. a) Na/(Ca + Na) ratios plotted as a function of Fe/(Mg + Fe) ratios for each sample. Displays the chemical heterogeneity between the two assemblages. b) Mg vs. Fe plot. The dashed line represents the schorl – dravite solid-solution line. c) Al vs. Na plot. The majority of Darajat samples loosely plot along the $NaAl(CaMg)_{-1}$ exchange vector. All symbols follow the key in Figure 2.9.

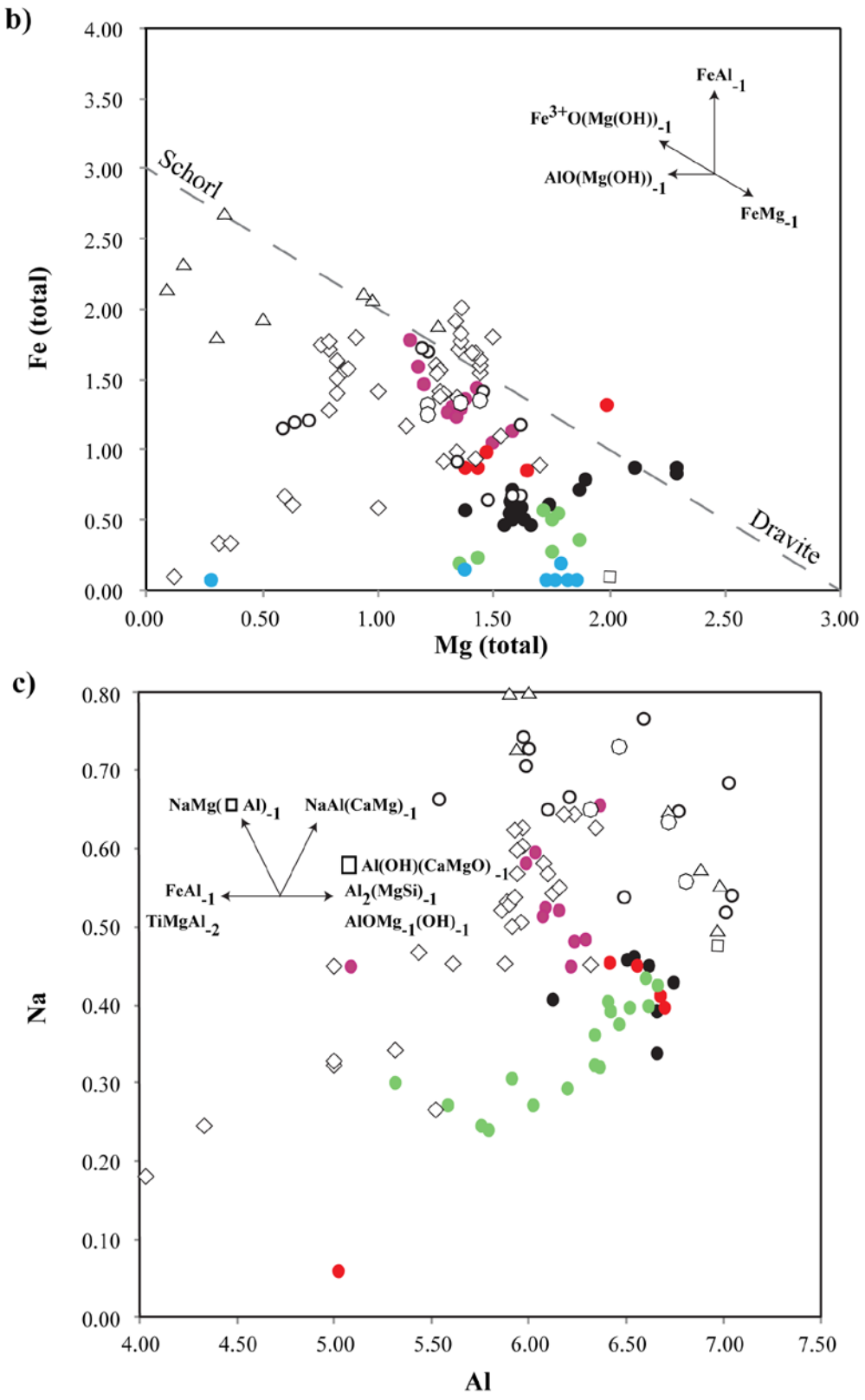


Figure 2.10 (continued):

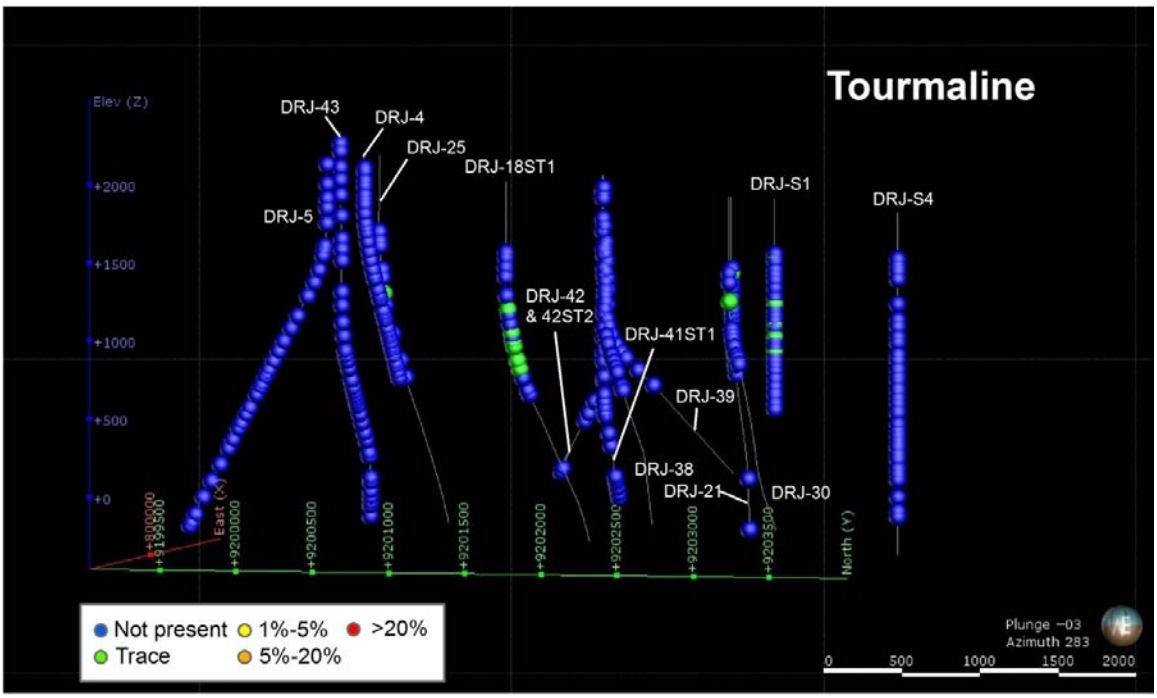


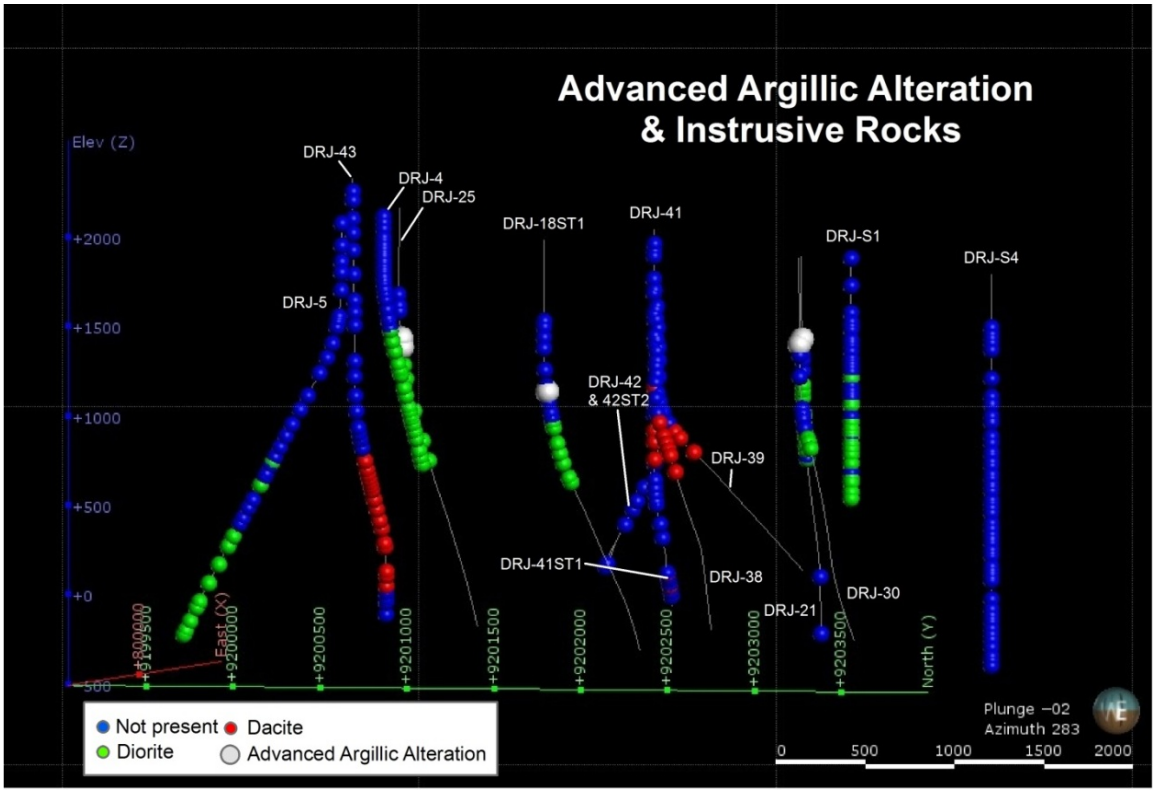


Figure 2.11: Distribution of tourmaline (top) and advanced argillic alteration assemblages (bottom). Also shown are the locations of diorites and dacites. The diorite was eroded prior to emplacement of the overlying rocks and formation of the advanced argillic alteration assemblages.

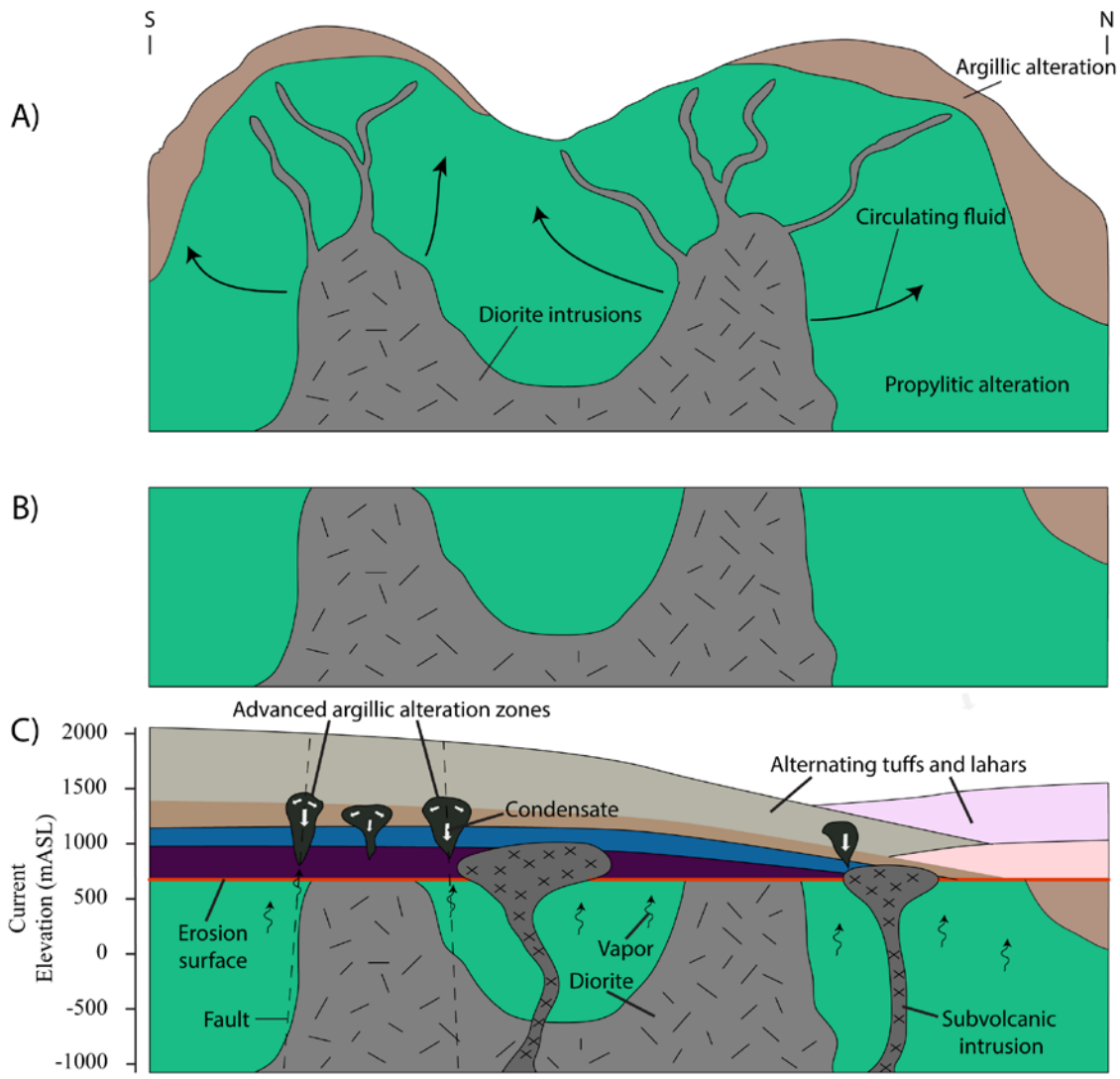


Figure 2.12: Simplified conceptual model of the evolution of the Darajat geothermal system. A) Initial emplacement of the diorite intrusions; this resulted in propylitic and argillic alteration. B) A tectonic erosional event (likely a flank collapse) removed overlying strata, resulting in the precipitation of chalcedony. C) Later subvolcanic intrusions are emplaced and overlying tuffs and lahars are deposited. Ascending vapors condensed, spread laterally and descended downward (white arrows), resulting in Stage 3 advanced argillic alteration and tourmalines. Upon heating, these descending fluids precipitated calcite and anhydrite; this prohibited meteoric recharge, therefore maintaining vapor-dominated conditions that still exist. The current elevation shown in the bottom panel is in meters above sea level.

# APPENDIX A

## X-RAY DIFFRACTION METHODOLOGY AND MINERAL ABUNDANCES

Whole-rock and clay X-ray diffraction (XRD) analyses were performed on each sample in the XRD laboratory at the Energy & Geoscience Institute at the University of Utah, using a Bruker D8 Advance X-ray diffractometer. Phase quantification using the Rietveld method was performed using TOPAS software, developed by Bruker AXS. The Rietveld method fits the peak intensities calculated from a model of the crystalline structure to the observed X-ray powder pattern by a least squares refinement. This is done by varying the parameters of the crystal structures to minimize the difference between the observed and calculated powder patterns. Because the whole powder pattern is taken into consideration, problems of peak overlap are minimized and accurate quantitative analyses can be obtained.

The following operating parameters were used when analyzing the powdered samples: Cu-Kα radiation at 40 kV and 40 mA, 0.02°2θ step size, and 0.4 and 0.6 seconds per step, for clay and bulk samples, respectively. Clay samples were examined from 2 to 45°2θ, and the bulk samples from 4 to 65°2θ. The instrument is equipped with a Lynx Eye detector, which collects data over 2.6 mm, rather than at a point, greatly increasing X-ray counts collected and decreasing acquisition time; a rotating sample stage, which increases the mineral grain orientations encountered by the incident electron beam; and

an automated sample exchanger capable of holding up to 90 samples.

At a minimum, three analyses were conducted on each sample, two or more on the clay-sized fraction and one on the bulk sample. The clay-sized fraction is prepared as follows:

- Samples are first ground in an electric mortar and pestle.
- The resulting powder is mixed with deionized water and further ground in a micronizing mill until fine enough to pass through a 325 mesh screen (particle size < 44 micrometers).
- The less than 5 micrometer size fraction is then separated using Stokes Law by placing the resulting slurry in a beaker (with a small amount of dispersant) and vigorously stirring. After allowing it to settle for 37 minutes, an aliquot (~100 ml) is pipetted out of the top ½ inch.
- The particles are removed from the water column by centrifuging for 15 min at 1500 rpm.
- The bulk of the clean water is decanted, and the sample is thoroughly mixed using an ultrasonic homogenizer.
- The slurry is then applied to a glass slide using a pipette.
- Once the sample has dried, an ‘air dried’ XRD pattern is obtained.
- The sample is then allowed to interact with ethylene glycol vapors for at least 12 hours at 65$^{o}$C to induce swelling of susceptible clays, after which a ‘glycolated’ XRD pattern is obtained.
- Additional heat treatments and scans that involve heating for 1 hour at 375 and/or 550$^{o}$C may be required to confirm the presence of some clay species.

The fraction used for the bulk analysis is prepared as follows:

- Samples are first ground in an electric mortar and pestle.
- The resulting powder is mixed with deionized water and further ground in a micronizing mill until fine enough to pass through a 325 mesh screen (particle size < 44 micrometers).
- The sample is then rolled approximately 50 times to randomly orient the mineral grains.
- The powder is placed in a sample holder which has concentric ridges on the bottom to help decrease the effects of preferred orientation.
- The surface is smoothed with a razor blade to eliminate surface roughness.
- An XRD pattern of the bulk sample is obtained.

The air-dried, glycolated and heated scans of the clay-sized fraction were compared with each other to identify the clay minerals present in the sample, using methods described by Moore and Reynolds (1997). The mineralogy of the clay fraction is then used in the Rietveld refinement of the bulk sample to quantify the abundances of all crystalline phases that are present. The data from Coso wells 68-6, 33A-7 and 73-19 are presented in Tables A.1-A.3.

Table A.1: Summary table of bulk and clay-sized fraction XRD results given by sample for well 68-6. Bulk refinements show abundances in weight percent of the sample, with results round to the nearest tenth. Tr = trace detection.

| Sample depth (m) | Smectite | Illite/Smectite | Illite | Chlorite | Plagioclase | Quartz | K-feldspar | Calcite | Epidote | Biotite | Hornblende | Pyrite | Muscovite | Titanite |
|---|---|---|---|---|---|---|---|---|---|---|---|---|---|---|
| 253.0 | 8.3 | | 5.3 | 4.9 | 35.5 | 22.2 | 8.2 | 8.2 | 1.6 | 0.6 | 4.8 | Tr | | |
| 274.3 | 2.8 | | 4.3 | 2.8 | 53.2 | 24.0 | 4.5 | 2.5 | 1.6 | 0.8 | 3.1 | Tr | | |
| 533.4 | | | 15.8 | 15.8 | 37.4 | 17.5 | 5.1 | 7.0 | | Tr | | Tr | | |
| 609.6 | | | 5.1 | 3.0 | 20.5 | 39.9 | 18.8 | 8.9 | Tr | 1.0 | 1.1 | Tr | Tr | |
| 722.4 | | | 1.0 | 0.9 | 29.9 | 36.1 | 18.5 | 10.2 | Tr | Tr | 1.5 | Tr | | |
| 1188.7 | | | 4.2 | 1.9 | 38.2 | 28.4 | 20.5 | 2.3 | 1.0 | Tr | 1.9 | Tr | 1.0 | |
| 1371.6 | | | 7.0 | 7.5 | 37.9 | 21.7 | 11.4 | 6.1 | 1.9 | 2.2 | 2.7 | 1.5 | | |
| 1484.4 | | | 6.4 | 6.6 | | 20.1 | | 3.5 | 1.5 | 3.0 | 1.7 | | | |
| 2066.5 | | | | 3.2 | 53.6 | 17.8 | 7.6 | Tr | 2.4 | 2.3 | 5.9 | | | |
| 2270.8 | | | | 3.8 | 47.2 | 16.6 | 10.0 | Tr | 3.7 | | | | | Tr |
| 2392.7 | | | 4.6 | 5.1 | 49.0 | 13.1 | 7.9 | 3.1 | 3.4 | 2.8 | 8.2 | Tr | | 1.0 |
| 2465.8 | | | 6.0 | 9.9 | 43.9 | 15.7 | 5.1 | 6.5 | 3.5 | 2.2 | 3.8 | | Tr | 2.5 |
| 2792.0 | | | 5.3 | 1.3 | 38.7 | 31.5 | 15.6 | 1.4 | 1.7 | Tr | 3.8 | | | tr |
| 2849.9 | | | 4.5 | 8.6 | 38.5 | 10.1 | 7.7 | Tr | 7.1 | Tr | 19.6 | Tr | 1.3 | 1.1 |
| 2941.3 | | | 2.3 | 2.9 | 66.3 | 11.6 | 10.6 | 2.0 | 3.4 | 1.3 | 2.5 | Tr | | Tr |
| 2984.0 | | | 3.1 | 8.3 | 42.0 | 6.7 | 4.3 | Tr | 7.9 | 1.2 | 24.6 | | | 1.0 |

Table A.2: Summary table of bulk and clay-sized fraction XRD results given by sample for well 33A-7. Bulk refinements show abundances in weight percent of the sample, with results rounded to the nearest tenth. Tr = trace detection.

| Sample depth (m) | Smectite | Illite/Smectite | Chlorite/Smectite | Illite | Chlorite | Plagioclase | Quartz | K-feldspar | Calcite | Epidote | Biotite | Hornblende | Pyrite | Muscovite | Titanite |
|---|---|---|---|---|---|---|---|---|---|---|---|---|---|---|---|
| 109.7 | 4.5 | Tr | | Tr | 15.4 | 22.5 | 3.6 | 13.4 | | 3.8 | Tr | 34.9 | | 1.2 | 1.2 |
| 262.1 | 8.1 | | | 5.3 | 5.4 | 15.5 | 37.2 | 23.3 | | 2.5 | 2.1 | Tr | | | |
| 414.5 | Tr | | | 8.0 | 2.7 | 31.0 | 37.1 | 25.7 | | 1.5 | Tr | 1.4 | | | |
| 566.9 | Tr | | 2.9 | Tr | | 24.8 | 3.5 | 30.3 | | 3.7 | Tr | 33.9 | | | |
| 646.2 | | 3.9 | | 2.3 | 10.2 | 53.3 | 11.9 | 6.5 | 1.0 | 0.8 | Tr | 10.0 | | | |
| 1024.1 | | Tr | | 6.9 | 8.3 | 35.5 | 30.0 | 10.5 | 3.0 | 2.4 | Tr | 2.1 | Tr | | |
| 1100.3 | | | | 6.4 | 15.1 | 34.3 | 23.5 | 9.4 | 3.7 | 4.4 | Tr | 1.3 | Tr | | |
| 1325.9 | | 5.9 | | 3.8 | 10.3 | 38.7 | 12.3 | 6.4 | 10.3 | 1.9 | Tr | 8.7 | Tr | | |
| 1569.7 | | | | 4.7 | 11.0 | 32.1 | 18.0 | 5.6 | 16.1 | 2.1 | 0.7 | 5.0 | Tr | 1.0 | 1.0 |
| 1649.0 | Tr | Tr | | 8.3 | 15.9 | 39.1 | 8.0 | 5.5 | 4.2 | 5.9 | 0.6 | 11.1 | Tr | | |

Table A.2 (continued):

| Sample depth (m) | Smectite | Illite/Smectite | Chlorite/Smectite | Illite | Chlorite | Plagioclase | Quartz | K-feldspar | Calcite | Epidote | Biotite | Hornblende | Pyrite | Muscovite | Titanite |
|---|---|---|---|---|---|---|---|---|---|---|---|---|---|---|---|
| 1877.6 | Tr | Tr | | 4.5 | 13.0 | 42.6 | 11.3 | 9.3 | 2.7 | 4.1 | Tr | 5.7 | | | |
| 1984.2 | Tr | Tr | | 4.1 | 8.3 | 35.6 | 13.1 | 13.8 | 20.0 | 1.5 | Tr | 2.1 | | | |
| 2136.6 | Tr | | | 4.0 | 8.6 | 46.8 | 14.3 | 10.6 | 2.9 | 4.4 | Tr | 6.7 | | 1.2 | 1.2 |
| 2212.8 | Tr | Tr | | 14.3 | 7.4 | 46.1 | 1.0 | 10.0 | 1.6 | 7.4 | Tr | 11.5 | | | |
| 2322.6 | Tr | Tr | | 4.2 | 14.6 | 42.4 | 3.4 | 3.7 | 1.6 | 4.9 | Tr | 9.2 | | | |
| 2350.0 | Tr | Tr | | 5.0 | 12.3 | 49.1 | 4.3 | 10.1 | 1.5 | 4.2 | Tr | 9.8 | Tr | 2.7 | 2.7 |
| 2380.5 | | | | 4.0 | 4.2 | 42.7 | 23.5 | 18.7 | | 2.7 | Tr | 2.0 | Tr | 1.8 | 1.8 |
| 2502.4 | | | | 3.0 | 8.6 | 41.7 | 17.2 | 15.5 | | 3.1 | Tr | 10.2 | | Tr | Tr |
| 2529.8 | Tr | Tr | | 4.6 | 6.8 | 53.1 | 5.2 | 6.6 | Tr | 6.6 | 0.6 | 15.2 | Tr | | |
| 2532.9 | | Tr | | 1.9 | 5.3 | 52.5 | 17.5 | 8.6 | Tr | 4.8 | 2.4 | 6.5 | Tr | | |

Table A.2 (continued):

| Sample depth (m) | Smectite | Illite/Smectite | Chlorite/Smectite | Illite | Chlorite | Plagioclase | Quartz | K-feldspar | Calcite | Epidote | Biotite | Hornblende | Pyrite | Muscovite | Titanite |
|---|---|---|---|---|---|---|---|---|---|---|---|---|---|---|---|
| 2566.4 | | Tr | | 5.8 | 2.7 | 60.8 | 5.7 | 7.3 | | 3.1 | Tr | 12.8 | 0.3 | | |
| 2624.3 | | Tr | | 4.6 | 6.8 | 53.0 | 5.3 | 6.6 | | 6.6 | Tr | 15.2 | | | |
| 2654.8 | | Tr | | 4.6 | 8.1 | 53.0 | 5.2 | 6.6 | Tr | 6.6 | Tr | 15.2 | | | |
| 2685.3 | | | | 3.4 | 6.3 | 47.4 | 20.2 | 16.9 | Tr | 2.3 | Tr | 2.1 | Tr | | |
| 2746.2 | Tr | Tr | | 4.6 | 8.1 | 52.9 | 5.2 | 6.6 | Tr | 6.6 | Tr | 15.2 | Tr | | |
| 2837.7 | | Tr | | 5.6 | 4.2 | 49.1 | 16.1 | 13.2 | Tr | 2.7 | Tr | 4.7 | Tr | 2.8 | 2.8 |
| 2959.6 | | | | 6.5 | 7.0 | 52.3 | 3.3 | 4.4 | 1.3 | 1.5 | Tr | 22.4 | Tr | | |
| 2990.1 | | | | | 17.0 | 41.4 | 3.5 | 4.4 | 1.2 | Tr | Tr | 21.1 | | | |
| 3051.0 | | | | | 14.1 | 42.9 | 2.5 | 6.2 | 1.0 | 1.6 | Tr | 17.3 | | 10.1 | 10.1 |
| 3081.5 | | | | | 8.1 | 43.7 | 6.3 | 4.9 | Tr | 1.3 | 1.0 | 21.1 | Tr | 9.3 | 9.3 |

Table A.2 (continued):

| Sample depth (m) | Smectite | Illite/Smectite | Chlorite/Smectite | Illite | Chlorite | Plagioclase | Quartz | K-feldspar | Calcite | Epidote | Biotite | Hornblende | Pyrite | Muscovite | Titanite |
|---|---|---|---|---|---|---|---|---|---|---|---|---|---|---|---|
| 3112.0 | | | | | 10.8 | 42.1 | 11.2 | 9.3 | 1.9 | 1.5 | Tr | 16.7 | Tr | 3.7 | 3.7 |
| 3142.5 | | | | | 7.1 | 49.9 | 5.9 | 7.2 | 2.3 | 2.1 | Tr | 21.6 | Tr | | |
| 3173.0 | | | | | 14.2 | 35.9 | 4.4 | 5.7 | 2.8 | 3.8 | Tr | 29.6 | Tr | | |
| 3233.9 | | | | | 11.5 | 36.1 | 13.9 | 11.2 | 2.0 | 4.1 | Tr | 17.0 | Tr | 2.0 | 2.0 |
| 3294.9 | | | | | 12.6 | 32.3 | 13.1 | 10.3 | 1.3 | 5.1 | 2.5 | 10.8 | Tr | | |

Table A.3: Summary table of bulk and clay-sized fraction XRD results given by sample for well 73-19. Bulk refinements show abundances in weight percent of the sample, with results rounded to the nearest tenth. Tr = trace detection.

| Sample depth (m) | Smectite | Illite/Smectite | Illite | Chlorite | Plagioclase | Quartz | K-feldspar | Calcite | Epidote | Biotite | Hornblende | Pyrite | Muscovite | Titanite |
|---|---|---|---|---|---|---|---|---|---|---|---|---|---|---|
| 390.1 | Tr | | 1.3 | 2.0 | 55.4 | 11.6 | 0.9 | 0.4 | 7.8 | 6.6 | 8.4 | Tr | 4.7 | Tr |
| 533.4 | Tr | | 1.1 | 1.1 | 38.0 | 30.6 | 23.0 | 0.5 | 1.4 | Tr | 0.5 | Tr | 1.6 | Tr |
| 545.6 | Tr | | 4.5 | 7.2 | 42.4 | 7.8 | 1.6 | 7.9 | 1.9 | Tr | 0.4 | Tr | 2.1 | 1.4 |
| 777.2 | Tr | | 1.7 | 1.0 | 34.5 | 36.4 | 20.4 | 0.8 | 3.8 | Tr | 1.8 | | 3.3 | |
| 798.6 | Tr | | 2.4 | 1.4 | 54.2 | 16.3 | 1.8 | 2.8 | 6.7 | 9.6 | 3.3 | Tr | | 1.1 |
| 1060.7 | | | 2.6 | 2.0 | 34.7 | 35.7 | 21.0 | 0.7 | 1.5 | Tr | 0.5 | Tr | | Tr |
| 1072.9 | | | 2.2 | 1.4 | 18.3 | 34.6 | 17.5 | 0.7 | 2.3 | Tr | 0.2 | Tr | 2.5 | 1.0 |
| 1225.3 | | Tr | 2.6 | 2.6 | 46.1 | 18.2 | 2.9 | 1.5 | 11.0 | 5.4 | 4.3 | Tr | 3.1 | 1.5 |
| 1316.7 | | | 1.7 | 3.7 | 59.0 | 21.2 | 1.6 | 0.9 | 2.9 | 4.5 | 2.7 | Tr | | Tr |
| 1347.2 | | Tr | 4.9 | 2.7 | 36.7 | 35.2 | 15.0 | 1.0 | 1.4 | Tr | 0.3 | | 2.7 | |
| 1411.2 | | 2.4 | 11.0 | 12.0 | 16.1 | 26.5 | 4.8 | 20.0 | 3.4 | Tr | 2.7 | | | |
| 1581.9 | | | 5.4 | 3.8 | 48.6 | 9.0 | 6.5 | 0.8 | 3.1 | Tr | 10.3 | Tr | 11.2 | |
| 1709.9 | | | 6.5 | 2.8 | 52.1 | 21.0 | 5.3 | 0.8 | 3.6 | 1.2 | 5.8 | Tr | | |
| 1813.6 | | | 7.5 | 3.3 | 27.6 | 46.5 | 10.7 | 1.7 | Tr | Tr | 1.5 | Tr | | |
| 1856.2 | | | 2.4 | 3.8 | 30.1 | 34.4 | 9.7 | 4.4 | 1.0 | Tr | 0.7 | Tr | | |

APPENDIX B

PREEXISTING WHOLE-ROCK OXYGEN ISOTOPE DATA

Here 513 preexisting whole-rock oxygen isotope analyses from 52 wells throughout the Coso system, made available by Terra-Gen, have been compiled into Table B.1. Every measurement was made at Southern Methodist University. These data helped determine the well to study in detail for this project (68-6, 33A-7 and 73-19).

Table B.1: 513 Preexisting whole-rock oxygen isotope analyses from the Coso system. Elevation (in meters) is relative to mean sea level; $\delta^{18}O$ values are in ‰ notation, relative to VSMOW.

| Well | Elevation | $\delta^{18}O$ (‰) | Well | Elevation | $\delta^{18}O$ (‰) |
|---|---|---|---|---|---|
| BLM 84-30 | 1162 | 8.03 | | 1018 | 8.19 |
| | 1089 | 7.21 | | 866 | 7.50 |
| | 940 | 4.23 | | 744 | 7.50 |
| | 662 | 1.22 | | 604 | 7.28 |
| | 498 | 7.54 | | 442 | 8.43 |
| | 402 | 6.07 | | 373 | 6.83 |
| | 254 | 8.47 | | 225 | 7.79 |
| | 117 | 7.38 | | 70 | 8.55 |
| | 102 | 9.32 | | -75 | 7.65 |
| | -62 | 6.74 | | -214 | 6.51 |
| | -167 | 6.82 | | -291 | 8.06 |
| | -321 | 7.15 | | -436 | 5.12 |
| | -406 | 7.52 | | -510 | 7.03 |
| | -521 | 6.04 | | -587 | 5.85 |
| | -559 | 7.88 | | -759 | 7.43 |
| | -650 | 7.70 | | -840 | 7.55 |
| | -751 | 7.66 | | -925 | 5.54 |
| | -868 | 6.92 | | -1062 | 5.79 |
| | -939 | 7.17 | | -1189 | 6.77 |
| | -995 | 7.02 | | -1292 | 5.10 |
| BLM33B-19 | 1079 | 7.98 | | -1353 | 4.48 |

Table B.1 (continued):

| Well | Elevation | $\delta^{18}O$ (‰) |
|---|---|---|
| NVY51A-16 | 985 | 6.91 |
| | 875 | 9.60 |
| | 687 | 6.84 |
| | 482 | 9.60 |
| | 324 | 7.66 |
| | 223 | 6.66 |
| | 90 | 7.44 |
| | -85 | 7.24 |
| | -88 | 5.94 |
| | -250 | 5.00 |
| | -347 | 7.63 |
| | -430 | 5.83 |
| | -546 | 6.60 |
| | -604 | 9.44 |
| | -692 | 6.60 |
| | -765 | 7.23 |
| | -889 | 6.33 |
| | -926 | 5.71 |
| | -1044 | 4.51 |
| | -1167 | 6.65 |
| | -1225 | 4.41 |
| | -1297 | 2.70 |
| NVY34A-9 | 1041 | 9.07 |
| | 946 | 7.60 |
| | 779 | 7.38 |
| | 645 | 6.63 |
| | 526 | 6.08 |
| | 350 | 4.95 |
| | 293 | 6.18 |
| | 123 | 7.81 |
| | 93 | 5.89 |
| | -7 | 5.90 |
| | -63 | 7.81 |
| | -133 | 6.39 |
| | -180 | 8.91 |
| | -238 | 6.97 |
| | -324 | 7.82 |
| | -412 | 6.86 |
| | -494 | 8.82 |
| | -578 | 7.35 |
| | -664 | 4.55 |
| | -806 | 7.41 |
| | -931 | 6.61 |
| | -1002 | 6.11 |
| | -1075 | 5.87 |
| | -1166 | 7.10 |
| | -1308 | 8.60 |
| | -1416 | 7.69 |

| Well | Elevation | $\delta^{18}O$ (‰) |
|---|---|---|
| | -1477 | 5.38 |
| | -1558 | 6.77 |
| | -1587 | 4.77 |
| | -1631 | 5.91 |
| NVY68-6 | 1022 | 4.36 |
| | 855 | 4.03 |
| | 736 | 3.32 |
| | 669 | 6.35 |
| | 556 | 6.60 |
| | 477 | 5.16 |
| | 321 | 4.26 |
| | 204 | 5.33 |
| | 105 | 5.31 |
| | 31 | 4.77 |
| | -61 | 4.45 |
| | -165 | 2.72 |
| | -230 | 3.77 |
| | -365 | 4.39 |
| | -454 | 5.22 |
| | -582 | 5.15 |
| | -707 | 3.82 |
| | -760 | 4.59 |
| | -830 | 3.56 |
| | -903 | 2.99 |
| | -1020 | 1.48 |
| | -1091 | 0.99 |
| | -1188 | 0.57 |
| | -1265 | 0.35 |
| | -1327 | 0.66 |
| | -1407 | 4.02 |
| | -1463 | –0.52 |
| | -1552 | –4.06 |
| | -1593 | 0.52 |
| | -1670 | 0.57 |
| NVY73A-7 | 1091 | 6.20 |
| | 978 | 6.72 |
| | 858 | 6.83 |
| | 768 | 6.23 |
| | 734 | 5.72 |
| | 659 | 5.48 |
| BLM 58A-18 | 1095 | 7.78 |
| | 970 | 7.82 |
| | 848 | 7.41 |
| | 714 | 7.17 |
| | 594 | 7.55 |

Table B.1 (continued):

| Well | Elevation | $\delta^{18}O$ (‰) |
|---|---|---|
| | 492 | 6.78 |
| | 375 | 7.43 |
| | 252 | 7.23 |
| | 88 | 7.11 |
| | -34 | 6.14 |
| | -169 | 7.61 |
| | -279 | 5.88 |
| | -429 | 6.56 |
| | -512 | 5.96 |
| | -620 | 7.02 |
| | -701 | 5.47 |
| | -792 | 6.26 |
| | -883 | 5.06 |
| | -983 | 3.47 |
| | -1080 | 6.15 |
| | -1228 | 7.43 |
| | -1291 | 6.03 |
| BLM 43-7 | 938 | 6.16 |
| | 825 | 6.94 |
| | 752 | 5.9 |
| | 664 | 5.8 |
| | 569 | 4.73 |
| | 499 | 5.06 |
| | 426 | 4.74 |
| NVY 76B-18 | 1076 | 7.34 |
| | 972 | 7.89 |
| | 865 | 7.48 |
| | 680 | 7.08 |
| | 375 | 4.41 |
| | 132 | 4.52 |
| | -103 | 7.42 |
| | -217 | 5.99 |
| | -417 | 7.08 |
| | -529 | 9.8 |
| | -730 | 8.54 |
| | -828 | 1.62 |
| | -897 | 4.48 |
| | -1019 | 4.12 |
| | -1153 | 4.96 |
| | -1189 | 5.02 |
| BLM 66-6 | 893 | 7.08 |
| | 694 | 6.78 |
| | 529 | 4.21 |
| | 398 | 4.38 |
| | 239 | 3.02 |

| Well | Elevation | $\delta^{18}O$ (‰) |
|---|---|---|
| | 97 | 3.62 |
| | -48 | 4.28 |
| | -368 | 0.37 |
| | -459 | 2.83 |
| | -583 | 0.23 |
| BLM 88-1 | 1071 | 7.67 |
| | 913 | 6.79 |
| | 821 | 7.24 |
| | 663 | 7.95 |
| BLM 88-1RD | 553 | 5.41 |
| | 399 | 7.50 |
| | 284 | 5.55 |
| | 121 | 6.67 |
| | -61 | 1.75 |
| BLM 23A-19 | 782 | 7.00 |
| | 621 | 8.35 |
| | 392 | 9.00 |
| | 69 | 6.82 |
| | -163 | 7.60 |
| | -406 | 6.55 |
| | -542 | 4.50 |
| | -827 | 6.09 |
| | -1173 | 5.68 |
| | -1362 | 5.32 |
| NVY 63A-18 | 963 | 6.88 |
| | 734 | 6.18 |
| | 543 | 5.54 |
| | 394 | 4.85 |
| | 201 | 5.17 |
| | 61 | 5.74 |
| | -195 | 6.22 |
| | -343 | 4.39 |
| | -562 | 4.39 |
| | -866 | 4.47 |
| NVY 41B-8 | 1006 | 7.06 |
| | 789 | 6.54 |
| | 596 | 6.58 |
| | 378 | 7.15 |
| | 107 | 6.65 |
| | -94 | 6.65 |
| | -324 | 7.56 |
| | -482 | 9.47 |
| | -697 | 7.66 |
| NVY 66-7 | 1172 | 6.07 |
| | 1041 | 7.88 |

Table B.1 (continued):

| Well | Elevation | $\delta^{18}O$ (‰) |
|---|---|---|
| | 870 | 6.24 |
| | 719 | 6.29 |
| | 584 | 4.78 |
| | 471 | 5.62 |
| | 323 | 5.60 |
| | 182 | 6.05 |
| NVY 63B-18 | 830 | 6.50 |
| | 501 | 5.89 |
| | 230 | 6.06 |
| | 19 | 2.42 |
| | -255 | 5.13 |
| | -586 | 4.83 |
| NVY 63B-18D | -816 | 6.13 |
| | -1024 | 6.97 |
| | -1234 | 4.70 |
| | -1397 | 4.09 |
| NVY 78B-6RD | 976 | 7.66 |
| | 706 | 6.97 |
| | 485 | 5.08 |
| | 243 | 3.40 |
| | 47 | 3.26 |
| NVY 78B-6ST | -170 | 3.25 |
| | -347 | 4.06 |
| | -615 | 3.23 |
| | -806 | 2.18 |
| BLM CGEH1 | 1176 | 6.02 |
| | 1063 | 6.36 |
| | 908 | 7.88 |
| | 756 | 6.26 |
| | 633 | 6.87 |
| | 436 | 7.02 |
| | 285 | 7.45 |
| | 84 | 6.46 |
| | -101 | 5.62 |
| NVY 23A-17 | 1023 | 5.59 |
| | 767 | 6.05 |
| | 648 | 6.30 |
| | 453 | 7.20 |
| | 243 | 5.90 |
| | -70 | 6.82 |
| | -343 | 5.73 |
| | -583 | 6.18 |
| | -814 | 4.63 |
| | -1066 | 4.28 |
| NVY 13A-16 | 927 | 8.45 |

| Well | Elevation | $\delta^{18}O$ (‰) |
|---|---|---|
| | 713 | 7.30 |
| | 595 | 7.29 |
| | 377 | 7.84 |
| | 262 | 7.11 |
| | 121 | 7.28 |
| | -104 | 7.04 |
| | -303 | 7.04 |
| | -538 | 7.37 |
| | -769 | 7.01 |
| NVY 64-16 | 888 | 6.41 |
| | 690 | 7.38 |
| NVY 64-16RD | 258 | 6.24 |
| | -14 | 7.78 |
| | -298 | 8.05 |
| | -536 | 7.63 |
| | -708 | 7.58 |
| | -928 | 5.84 |
| | -1185 | 3.22 |
| | -1298 | 2.05 |
| | -1526 | 5.25 |
| BLM 54-7RD | 697 | 5.42 |
| | 557 | 5.61 |
| | 345 | 4.28 |
| | 220 | 5.79 |
| | 75 | 5.54 |
| | -297 | 4.52 |
| | -421 | 7.32 |
| | -667 | 5.77 |
| | -912 | 3.29 |
| | -1122 | 2.82 |
| NVY 38-9 | 935 | 4.52 |
| | 630 | 7.07 |
| | 338 | 6.92 |
| | 22 | 7.11 |
| | -282 | 7.21 |
| | -585 | 6.83 |
| | -888 | 6.51 |
| | -1155 | 4.65 |
| | -1466 | 5.48 |
| | -1741 | 5.78 |
| NVY 38A-9 | -433 | 6.35 |
| | -732 | 5.28 |
| | -1052 | 4.23 |
| | -1271 | 4.60 |
| | -1492 | 5.81 |

Table B.1 (continued):

| Well | Elevation | $\delta^{18}O$ (‰) |
|---|---|---|
| NVY 47A-8RD | 884 | 5.55 |
| | 776 | 4.44 |
| | 566 | 6.98 |
| | 484 | 6.17 |
| | 352 | 6.98 |
| | 189 | 7.39 |
| | -2 | 2.75 |
| NVY 78-7 | 998 | 7.40 |
| | 668 | 5.29 |
| | 552 | 6.14 |
| | 396 | 4.84 |
| | 177 | 5.00 |
| | 55 | 4.65 |
| | -95 | 6.31 |
| | -223 | 5.85 |
| | -362 | 5.75 |
| BLM 46A-19RD | 379 | 6.98 |
| | 94 | 6.77 |
| | -242 | 7.90 |
| | -462 | 7.12 |
| | -724 | 5.17 |
| | -942 | 7.14 |
| | -1232 | 6.51 |
| | -1536 | 6.71 |
| | -1828 | 7.56 |
| | -2052 | 0.45 |
| | -2113 | 0.41 |
| | -2265 | 5.22 |
| | -2373 | 7.02 |
| | -2579 | 5.20 |
| Navy I 87A-7 | 1128 | 8.92 |
| | 1031 | 9.15 |
| | 886 | 5.81 |
| | 696 | 5.94 |
| | 580 | 5.23 |
| | 425 | 6.24 |
| | 258 | 5.46 |
| Navy I 24A-8 | 1120 | 6.05 |
| | 931 | 6.59 |
| | 693 | 6.28 |
| | 462 | 6.15 |
| | 288 | 4.41 |
| | 155 | 6.12 |
| | 24 | 4.08 |
| | -150 | 1.52 |

| Well | Elevation | $\delta^{18}O$ (‰) |
|---|---|---|
| | -272 | 2.90 |
| | -417 | 1.42 |
| Navy I 41A-8 | 1003 | 6.34 |
| | 815 | 6.80 |
| | 601 | 6.81 |
| | 425 | 5.65 |
| | 239 | 7.76 |
| | 83 | 6.94 |
| | -107 | 5.72 |
| | -305 | 6.81 |
| | -534 | 7.32 |
| | -733 | 6.60 |
| Navy II 81A-18 | 1090 | 6.94 |
| | 959 | 7.67 |
| Navy II 81A-18RD | 832 | 6.33 |
| | 696 | 6.13 |
| | 489 | 4.90 |
| | 392 | 5.33 |
| | 280 | 4.28 |
| | 180 | 5.71 |
| Navy II 67C-17 | 924 | 7.84 |
| | 726 | 7.95 |
| | 538 | 7.35 |
| | 321 | 7.79 |
| | 86 | 7.30 |
| | -181 | 7.50 |
| | -520 | 7.63 |
| | -701 | 7.00 |
| | 0 | 6.06 |
| | -927 | 5.60 |
| | 0 | 6.60 |
| | -1118 | 7.50 |
| Navy II 86-17 | 823 | 7.89 |
| | 452 | 7.19 |
| | 171 | 7.19 |
| | -84 | 8.21 |
| | -370 | 8.93 |
| | -694 | 6.65 |
| | -1007 | 6.73 |
| | -1333 | 6.69 |
| | -1497 | 5.66 |
| | -1733 | 5.67 |
| Navy II 83-16 | 900 | 7.37 |
| | 593 | 8.00 |
| | 270 | 6.56 |

Table B.1 (continued):

| Well | Elevation | $\delta^{18}O$ (‰) |
|---|---|---|
| | -36 | 7.77 |
| | -353 | 6.77 |
| | -658 | 6.65 |
| | -898 | 7.32 |
| | -1196 | 6.99 |
| | -1492 | 6.45 |
| | -1824 | 7.08 |
| Navy II 83B-16 | 845 | 7.37 |
| | 501 | 6.88 |
| | 211 | 7.79 |
| | -109 | 7.09 |
| | -363 | 6.14 |
| | -706 | 5.13 |
| | -965 | 5.47 |
| | -1224 | 5.72 |
| | -1501 | 7.25 |
| | -1916 | 6.97 |
| Navy II 64A-16 | 793 | 8.16 |
| | 507 | 7.11 |
| | 203 | 7.76 |
| | -100 | 6.98 |
| | -347 | 6.94 |
| | -650 | 6.78 |
| | -905 | 6.04 |
| | -1241 | 3.95 |
| | -1471 | 7.75 |
| | -1709 | 6.82 |
| Navy II 67-17 | 799 | 7.59 |
| | 537 | 8.33 |
| | 252 | 7.16 |
| | 47 | 7.04 |
| | -125 | 7.37 |
| | -325 | 7.11 |
| | -508 | 6.58 |
| | -693 | 7.23 |
| | -1009 | 7.19 |
| | -1381 | 6.90 |
| Navy II 37B-17 | 1000 | 8.32 |
| | 726 | 6.43 |
| | 522 | 5.41 |
| | 273 | 5.76 |
| | 38 | 6.33 |
| | -152 | 6.64 |
| | -362 | 6.22 |
| | -576 | 6.68 |

| Well | Elevation | $\delta^{18}O$ (‰) |
|---|---|---|
| BLM 52-20 | 890 | 7.68 |
| | 654 | 8.07 |
| | 401 | 7.21 |
| | 201 | 7.34 |
| | -6 | 6.26 |
| | -207 | 6.68 |
| | -434 | 7.20 |
| | -616 | 6.98 |
| | -838 | 7.53 |
| | -1082 | 5.70 |
| BLM 47B-20 | 976 | 6.46 |
| | 790 | 6.02 |
| | 540 | 5.18 |
| | 337 | 6.99 |
| | 89 | 7.17 |
| | -31 | 7.59 |
| | -258 | 6.74 |
| | -504 | 6.31 |
| | -663 | 6.71 |
| BLM 16A-20 | 1056 | 7.97 |
| | 788 | 7.33 |
| | 599 | 8.14 |
| | 280 | 6.84 |
| | 41 | 4.27 |
| | -200 | 6.31 |
| | -367 | 6.36 |
| | -588 | 7.12 |
| | -908 | 7.09 |
| BLM 24-20 | 975 | 7.76 |
| | 656 | 7.40 |
| | 352 | 7.17 |
| BLM 24-20RD | 63 | 6.83 |
| | -122 | 6.28 |
| | -439 | 5.23 |
| | -570 | 4.20 |
| | -735 | 4.99 |
| BLM 88-20 | 972 | 6.41 |
| | 682 | 8.18 |
| | 454 | 6.15 |
| | 183 | 6.15 |
| | -40 | 6.02 |
| | -237 | 7.59 |
| | -471 | 7.81 |
| | -680 | 7.53 |
| | -892 | 7.33 |

Table B.1 (continued):

| Well | Elevation | $\delta^{18}O$ (‰) |
|---|---|---|
| | -1108 | 6.71 |
| BLM 81A-19 | 962 | 7.51 |
| | 752 | 7.88 |
| BLM 81A-19RD | 472 | 7.31 |
| | 296 | 7.41 |
| | 72 | 5.87 |
| | -53 | 7.06 |
| | -222 | 6.94 |
| | -366 | 6.25 |
| NVY 38B-9 | -748 | 5.52 |
| | -936 | 5.56 |
| | -1074 | 4.35 |
| | -1133 | 6.62 |
| | -1260 | 5.80 |
| | -1319 | 5.58 |
| | -1441 | 5.75 |
| | -1513 | 6.06 |

## B.2 New Oxygen Isotope Data

Here 140 new oxygen isotope measurements made on whole-rock, feldspar, chlorite, biotite and hornblende samples from wells 68-6, 33A-7 and 73-19 have been compiled. A complete dataset for each well is compiled into Tables B.2 (68-6), B.3 (33A-7) and B.4 (73-19).

Table B.2: Measured $\delta^{18}O$ values for whole-rock and mineral samples from well 68-6, Coso geothermal system, California. Values are reported in per mil (‰) notation, relative to SMOW.

| Well: 68-6 | | | | | |
|---|---|---|---|---|---|
| Depth (m) | Whole-Rock (‰) | Feldspar (‰) | Chlorite (‰) | Biotite (‰) | Hornblende (‰) |
| 271.3 | 3.88 | | | | |
| 335.3 | 4.47 | 6.04 | | | |
| 423.7 | 2.55 | | | | |
| 487.7 | 3.49 | 6.59 | 2.12 | | |
| 563.9 | 5.08 | | | | |
| 685.8 | 5.78 | | | | |
| 722.4 | 6.02 | 6.29 | | | |
| 883.9 | 3.57 | | | | |
| 984.5 | 4.07 | | | | |
| 1069.8 | 4.30 | | | | |
| 1271.0 | 4.43 | | | | |
| 1371.6 | 2.44 | 5.24 | | | |
| 1432.6 | 2.87 | | | | |
| 1484.4 | 1.50 | 4.96 | | | |
| 1554.5 | 2.60 | | | | |
| 1700.8 | 3.78 | 5.64 | 0.16 | | |
| 1798.3 | 4.67 | 6.76 | | | |
| 1935.5 | 4.46 | | | | |
| 2066.5 | 2.94 | | | | |
| 2270.8 | 2.70 | | | | |
| 2392.7 | 0.75 | | | | |
| 2465.8 | 0.75 | 3.09 | | | |
| 2566.4 | 0.61 | | | | |
| 2709.7 | 0.75 | 3.08 | | -3.18* | |
| 2792.0 | 2.83 | 3.59 | | | |
| 2849.9 | 0.54 | | | | |
| 2895.6 | 0.26 | | | | |
| 2941.3 | -4.60 | -3.88 | -1.53 | | |
| | | -5.06[#] | | | |
| | | -4.12[€] | | | |
| 2984.0 | -1.05 | 1.76 | 1.01 | | 3.58 |
| 3173.0 | 0.64 | | | | |

[#]Hand picked cloudy (more altered) feldspar
[€]Feldspar separated from finer-grained (150-200 mesh) whole rock aliquot
*Chloritized biotite

Table B.3: Measured $\delta^{18}O$ values for whole-rock and mineral samples from well 33A-7, Coso geothermal system, California. Values are reported in per mil (‰) notation, relative to SMOW.

| Well: 33A-7 | | | | | |
|---|---|---|---|---|---|
| Depth (m) | Whole-Rock (‰) | Feldspar (‰) | Chlorite (‰) | Biotite (‰) | Hornblende (‰) |
| 33.5 | 7.62 | 7.50 | | | |
| 109.7 | 3.7 | | | | |
| 262.1 | 5.39 | | | | |
| 414.5 | 7.45 | | | | |
| 566.9 | 4.84 | | | | |
| 646.2 | 5.34 | | | | |
| 871.7 | 0.2 | | | | |
| 1024.1 | 3.59 | | | | |
| 1100.3 | 3.00 | 5.49 | 1.98 | | |
| 1325.9 | 4.18 | | | | |
| 1569.7 | 3.89 | | | | |
| 1649.0 | 2.71 | | | | |
| 1877.6 | 1.03 | | | | |
| 1984.2 | 3.93 | | | | |
| 2136.6 | 1.60 | | | | |
| 2212.8 | -0.44 | | | | |
| 2322.6 | -0.02 | | | | |
| 2322.6 | -1.02 | | | | |
| 2350.0 | -0.98 | | | | |
| 2380.5 | 0.14 | | | | |
| 2471.9 | 0.51 | -2.37 | | | 4.35 |
| 2502.4 | -2.35 | | | | |
| 2529.8 | -3.08 | -0.03 | 0.32 | -3.83* | 4.31 |
| | | +0.63€ | | | |
| 2566.4 | 0.94 | 4.16 | | | |
| 2593.8 | 2.15 | 4.20 | | | 3.32 |
| 2624.3 | 1.55 | | | | |
| 2654.8 | 2.92 | | | | |
| 2685.3 | 2.10 | 4.60 | | | |
| 2746.2 | 3.91 | | | | |
| 2837.7 | 4.48 | 5.49 | | | |
| 2959.6 | 4.60 | | | | |
| 2990.1 | 4.25 | | | | |
| 3020.6 | 4.05 | | | | |
| 3051.0 | 1.78 | | | | |
| 3081.5 | 4.21 | | | | |
| 3112.0 | 4.03 | | | | |
| 3142.5 | 4.61 | | | | |
| 3173.0 | 4.10 | | | | |
| 3233.9 | 4.49 | | | | |
| 3294.9 | 3.88 | 5.90 | 4.12 | | |

€Feldspar separated from finer-grained (150-200 mesh) whole rock aliquot
*Chloritized biotite

Table B.4: Measured $\delta^{18}O$ values for whole-rock and mineral samples from well 73-19, Coso geothermal system, California. Values are reported in per mil (‰) notation, relative to SMOW.

| **Well: 73-19** | | | | | |
|---|---|---|---|---|---|
| Depth (m) | Whole-Rock (‰) | Feldspar (‰) | Chlorite (‰) | Biotite (‰) | Hornblende (‰) |
| 271.3 | 6.98 | 7.79 | | 3.84 | 4.62 |
| 381.0 | 6.61 | | | | |
| 390.1 | 6.37 | | | | |
| 445.0 | 7.48 | 8.12 | | | |
| 545.6 | 5.52 | | | | |
| 777.2 | 7.57 | | | | |
| 798.6 | 6.36 | | | | |
| 1060.7 | 7.16 | | | | |
| 1072.9 | 7.41 | | | | |
| 1225.3 | 6.07 | | | | |
| 1316.7 | 6.63 | | | | |
| 1347.2 | 5.91 | | | | |
| 1386.8 | 4.61 | 6.14 | -0.45 | 1.97 | |
| 1411.2 | 2.38 | | | | |
| 1481.3 | 6.30 | 7.26 | | 3.78 | 4.21 |
| 1581.9 | 5.94 | | | | |
| 1664.2 | 6.85 | | | | |
| 1709.9 | 5.13 | | | | |
| 1813.6 | 5.14 | 6.20 | | | |
| 1834.9 | 3.30 | 6.34 | | | |
| 1856.2 | 3.30 | | | | |

# APPENDIX C

## CALCULATION OF $\delta^{18}O$ VALUES OF RESERVOIR FLUIDS

The $\delta^{18}O$ values for the reservoir fluids in wells 33A-7, 68-6 and 73-19 have been determined using available measured $\delta^{18}O$ values of liquids and vapors collected at each well-head (Table C.1) and by following the approach described by Truesdell (1984). In order to compute the $\delta^{18}O$ value of the unboiled reservoir fluid from these two measured $\delta^{18}O$ values, the following information is also needed: 1) the temperature at which steam-liquid separation occurred; 2) the current reservoir temperature at each production zone; and 3) corresponding enthalpies (found by referring to steam tables) for vapor at separation temperature, liquid at separation temperature and liquid at the reservoir temperature. A steam fraction, y, is then calculated using these enthalpies, from the following equation (Truesdell, 1984):

$$y = \frac{H_{T,D} - H_{L,T}}{H_S - H_{L,T}}$$

where $H_{T,D}$ is the enthalpy of liquid water at the reservoir temperature, $H_{L,T}$ is the enthalpy of the liquid at the temperature of separation and $H_S$ is the enthalpy of the vapor at the temperature of separation. Using this y value, it possible to then calculate the

$\delta^{18}O_w^f$ value of the recombined (unboiled) reservoir with the following equation:

$$\delta^{18}O_w^f = y * \delta^{18}O_{v,T} + (1 - y) * \delta^{18}O_{l,T}$$

where $\delta^{18}O_{v,T}$ is the value of steam at separation, $\delta^{18}O_{l,T}$ is the value of the fluid at separation and $\delta^{18}O_w^f$ is the value of the unboiled reservoir fluid within each well (Truesdell, 1984).

Two assumptions are made when performing this calculation: first it is assumed that the steam and fluid remain together during ascent and only separate at the surface (single-stage separation process); second, it has been assumed that no isotopic exchange occurred between the rapidly ascending fluids and the host rock during ascent from the production zones to the well head.

The results of these recombination calculations of $\delta^{18}O_w^f$ values are compiled in Table C.1. Multiple calculations were possible for wells 68-6 and 73-19 because more than one well head test has been conducted for these wells. The average calculated $\delta^{18}O_w^f$ values of unboiled reservoir fluids are -7.49 ‰ (well 33A-7), -8.67 ‰ (well 68-6) and -5.56 ‰ (73-19); these values are used in Chapter 1.

Table C.1: Necessary information for calculation of unboiled reservoir fluid ($\delta^{18}O_w^f$) for wells 33A-7, 68-6 and 73-19. $\delta^{18}O_v$ is the measured value of vapor collected at each well head; $\delta^{18}O_F$ is the measured value of liquid water collected at each well head; $H_{T,D}$ is the enthalpy value for liquid water at the measured reservoir temperature; $H_S$ is the enthalpy value of the vapor at the separation temperature; $H_{L,T}$ is the enthalpy of the liquid water at the temperature of separation; y is the calculated steam (vapor) fraction; and $\delta^{18}O_w^f$ is the $\delta^{18}O$ value of the unboiled reservoir fluid.

| Well | $\delta^{18}O_v$ | $\delta^{18}O_F$ | Separation Temp. (°C) | Reservoir Temp. (°C) | $H_{T,D}$ | $H_S$ | $H_{L,T}$ | Y | $\delta^{18}O_w^f$ |
|---|---|---|---|---|---|---|---|---|---|
| 73-19 | -6.78 | -5.10 | 171 | 370 | 1873 | 2770 | 723.6 | 0.56 | -6.04 |
| 73-19 | -7.22 | -4.86 | 171 | 345 | 1624 | 2770 | 723.6 | 0.44 | -5.90 |
| 73-19 | -5.49 | -3.21 | 172 | 376 | 2099 | 2771 | 728.0 | 0.67 | -4.74 |
| 68-6 | -10.62 | -7.76 | 163 | 273 | 1195 | 2778 | 684.3 | 0.25 | -8.46 |
| 68-6 | -11.18 | -8.34 | 177 | 261 | 1134 | 2755 | 745.6 | 0.19 | -8.88 |
| 33A-7 | -10.48 | -5.85 | 109 | 282 | 1246 | 2688 | 452.8 | 0.35 | -7.49 |

# APPENDIX D

## TOURMALINE MINERAL CHEMISTRY DATA

The chemical compositions of tourmalines present within the Darajat geothermal system reservoir rocks have been determined by electron microprobe analysis. Table D.1 contains the initial oxide percent data returned; in total, 38 analyses were made.

Table D.1: Initial oxide percentage values for tourmalines found within the Darajat geothermal system. Values were determined using an electron microprobe analyzer.

| Sample | $Na_2O$ | $Al_2O_3$ | MgO | $SiO_2$ | $K_2O$ | CaO | $TiO_2$ | MnO | FeO | F | Cl | Oxide Totals |
|---|---|---|---|---|---|---|---|---|---|---|---|---|
| 670.1-2_1 | 1.21 | 33.07 | 6.45 | 36.46 | 0.06 | 1.27 | 0.24 | 0.03 | 3.78 | 0.32 | 0.02 | 82.90 |
| 670.1-2_2 | 1.20 | 32.27 | 6.06 | 37.31 | 0.31 | 1.35 | 0.58 | 0.12 | 3.21 | 0.09 | 0.01 | 82.50 |
| 670.1-2_3 | 0.96 | 30.37 | 8.57 | 36.79 | 0.19 | 0.89 | 0.10 | 0.24 | 6.26 | 0.65 | 0.02 | 85.03 |
| 670.1-2_4 | 0.72 | 28.63 | 8.95 | 35.03 | 0.50 | 1.03 | -0.11 | 0.30 | 6.11 | 0.43 | 0.08 | 81.67 |
| 670.1-2_5 | 0.72 | 27.63 | 8.69 | 34.07 | 0.88 | 3.74 | 0.19 | 0.39 | 5.72 | 0.79 | 0.07 | 82.87 |
| 670.1-1_1 | 1.14 | 32.16 | 6.16 | 37.83 | 0.40 | 1.25 | 0.14 | 0.09 | 3.42 | 0.29 | 0.15 | 83.04 |
| 670.1-1_2 | 1.18 | 31.79 | 6.07 | 37.95 | 0.51 | 1.36 | 0.08 | 0.13 | 3.43 | 0.44 | 0.03 | 82.98 |
| 670.1-1_3 | 1.10 | 31.68 | 6.41 | 38.12 | 0.89 | 1.18 | 0.33 | 0.19 | 3.52 | 0.37 | 0.04 | 83.82 |
| 670.1-1_4 | 0.98 | 31.59 | 6.56 | 37.92 | 0.48 | 1.19 | 0.06 | 0.11 | 3.28 | 0.36 | 0.04 | 82.56 |
| 670.1-1_5 | 0.97 | 31.44 | 6.19 | 38.31 | 0.85 | 1.30 | 0.06 | 0.12 | 3.54 | 0.17 | 0.11 | 83.06 |
| 670.1-4_1 | 0.84 | 30.58 | 7.41 | 38.29 | 0.73 | 0.97 | 0.25 | 0.17 | 4.80 | 0.32 | 0.06 | 84.41 |
| 670.1-4_2 | 0.93 | 27.18 | 5.54 | 46.57 | 0.49 | 0.91 | -0.03 | 0.11 | 4.09 | 0.15 | 0.01 | 85.95 |
| 670.1-4_3 | 1.24 | 32.10 | 6.25 | 37.54 | 0.11 | 1.18 | 0.33 | 0.05 | 4.34 | 0.38 | 0.03 | 83.54 |
| 670.1-4_4 | 0.79 | 26.63 | 7.16 | 31.35 | 0.42 | 1.22 | 8.44 | 0.22 | 5.22 | 0.25 | 0.10 | 81.81 |
| 670.1-3_1 | 1.29 | 33.16 | 6.19 | 35.62 | 0.10 | 1.10 | -0.01 | 0.16 | 4.81 | 0.40 | 0.14 | 82.96 |
| 670.1-3_2 | 1.21 | 30.23 | 5.79 | 33.14 | 0.25 | 6.10 | 0.09 | 0.24 | 3.97 | 0.08 | 0.06 | 81.16 |
| 670.1-3_3 | 0.87 | 30.22 | 6.83 | 36.65 | 0.98 | 2.44 | 0.16 | 0.24 | 4.11 | 0.31 | 0.01 | 82.83 |
| 807.7-1_1 | 1.42 | 32.84 | 6.01 | 36.46 | 0.03 | 0.74 | 0.19 | 0.11 | 7.33 | 0.00 | 0.11 | 85.24 |
| 807.7-1_2 | 1.23 | 34.13 | 5.47 | 36.05 | 0.13 | 1.02 | 0.23 | 0.14 | 6.35 | 0.01 | 0.15 | 84.90 |
| 807.7-1_3 | 0.19 | 26.55 | 8.28 | 40.98 | 3.57 | 0.09 | 0.08 | 0.61 | 9.86 | 0.03 | 0.33 | 90.59 |
| 807.7-2_1 | 1.27 | 33.71 | 5.71 | 35.99 | 0.04 | 0.89 | -0.36 | 0.08 | 6.30 | 0.01 | 0.08 | 83.72 |
| 807.7-2_2 | 1.42 | 34.20 | 6.70 | 36.42 | 0.02 | 0.95 | 0.19 | 0.09 | 6.25 | 0.01 | 0.05 | 86.30 |
| 821.4-1_5 | 1.43 | 34.71 | 7.82 | 37.46 | 0.01 | 1.16 | 0.50 | 0.01 | 2.79 | 0.05 | 0.04 | 85.98 |
| 821.4-1_6 | 1.44 | 33.62 | 5.47 | 41.71 | 0.01 | 2.70 | 0.20 | 0.05 | 1.38 | 0.09 | 0.37 | 87.04 |
| 821.4-1_10 | 1.08 | 26.76 | 5.97 | 35.11 | 0.02 | 1.02 | 0.20 | 0.01 | 1.82 | 0.00 | 0.43 | 72.42 |
| 821.4-2_1 | 1.03 | 33.38 | 6.98 | 36.12 | 0.03 | 1.88 | -0.18 | 0.11 | 3.36 | 0.01 | 0.07 | 82.79 |

Table D.1 continued:

| Sample | $Na_2O$ | $Al_2O_3$ | MgO | $SiO_2$ | $K_2O$ | CaO | $TiO_2$ | MnO | FeO | F | Cl | Oxide Totals |
|---|---|---|---|---|---|---|---|---|---|---|---|---|
| 821.4-2_2 | 1.21 | 33.78 | 6.94 | 36.29 | 0.01 | 1.81 | 0.03 | 0.05 | 3.78 | 0.01 | 0.03 | 83.94 |
| 821.4-2_3 | 1.22 | 26.29 | 3.15 | 46.66 | 0.01 | 7.55 | 0.18 | 0.06 | 1.16 | 0.08 | 0.00 | 86.35 |
| 821.4-2_4 | 1.38 | 32.21 | 7.11 | 35.57 | 0.02 | 1.31 | 0.16 | 0.06 | 3.84 | 0.06 | 0.10 | 81.81 |
| 975.1-1_7 | 1.61 | 31.27 | 5.46 | 36.11 | 0.02 | 1.02 | 0.28 | 0.13 | 9.97 | 0.00 | 0.05 | 85.92 |
| 975.1-1_9 | 1.83 | 30.59 | 4.48 | 35.64 | 0.03 | 0.61 | 0.18 | 0.12 | 13.05 | 0.00 | 0.00 | 86.53 |
| 975.1-1_10 | 1.22 | 22.83 | 5.21 | 32.63 | 0.00 | 9.95 | 8.74 | 0.05 | 6.42 | 0.01 | 0.12 | 87.18 |
| 975.1-5_1 | 1.49 | 31.93 | 5.39 | 35.91 | 0.03 | 1.01 | 0.17 | 0.12 | 9.51 | 0.01 | 0.09 | 85.66 |
| 975.1-5_3 | 1.63 | 31.14 | 4.68 | 36.57 | 0.03 | 0.74 | 0.22 | 0.24 | 11.79 | -0.09 | 0.12 | 87.07 |
| 975.1-5_4 | 1.46 | 31.32 | 5.09 | 35.87 | 0.05 | 1.04 | 0.24 | 0.12 | 9.77 | 0.03 | 0.01 | 85.00 |
| 975.1-5_5 | 1.38 | 31.37 | 5.20 | 35.87 | 0.03 | 1.07 | 0.24 | 0.12 | 9.99 | 0.04 | 0.00 | 85.31 |
| 975.1-7_5 | 2.15 | 34.34 | 6.70 | 37.39 | 0.02 | 1.50 | 0.09 | 0.11 | 8.81 | 0.01 | 0.03 | 91.15 |
| 975.1-7_6 | 1.80 | 30.46 | 5.72 | 36.47 | 0.01 | 1.09 | 0.39 | 0.09 | 10.37 | 0.03 | 0.01 | 86.44 |